Sources and gain in photonic random media

Sources and gain in photonic random media

ACADEMISCH PROEFSCHRIFT

ter verkrijging van de graad van doctor
aan de Universiteit van Amsterdam
op gezag van de Rector Magnificus
prof. dr. D. C. van den Boom
ten overstaan van een door het college voor promoties
ingestelde commissie,
in het openbaar te verdedigen in de Agnietenkapel
op woensdag 20 juni 2012, te 12.00 uur

door

Ramy Gerrit Samir El-Dardiry

geboren te Utrecht

Promotiecommissie

Promotor prof. dr. A. Lagendijk

Overige leden prof. dr. W. L. Barnes
prof. dr. H. Cao
prof. dr. ir. H. B. van Linden van den Heuvell
prof. dr. A. Polman
prof. dr. W. L. Vos

Faculteit der Natuurwetenschappen, Wiskunde en Informatica

Contents

CHAPTER 1

Introduction

The central topic of this thesis concerns the interaction between sources of electromagnetic radiation and complex multiple scattering media. Both of these two elements span a vast field in the natural sciences themselves. Our treatment of the matter in this introductory chapter is aimed at putting forward only the essential physics and background required to understand the experiments and theory described in this thesis. First, the various mechanisms for generation of electromagnetic radiation are described in Sec. 1.1. Second, the physics behind both single and multiple scattering of waves is briefly reviewed in Sec. 1.2. In Sec. 1.3, random lasers and infinite range correlations are introduced as two central research subjects that combine sources and multiple scattering. The contents of this thesis and our contribution are then outlined in Sec. 1.4.

1.1 Sources of electromagnetic radiation

Due to its importance in the everyday human perception of the world, light has inevitably been studied and put to use since ancient times. The wave nature of light was put forward by several natural philosophers of whom Christiaan Huygens (1629-1695) is generally accredited the most. His *Traité de la lumière* provides a fascinating look onto the status of optics during the early stages of the modern era [1]. By drawing an analogy with sound waves, Huygens concludes that light must be a wave that propagates via the mediation of tiny masses. In the original formulation of the famous principle named after him these tiny masses, the ether, indeed feature prominently:

> *De sorte qu'il faut qu'autour de chaque particule il se fasse une onde dont cette particule soit le centre [1]* (So it arises that around each particle there is made a wave of which that particle is the centre [2]).

This formulation has often been rephrased in terms of secondary sources instead of particles, although it would technically be more correct to view the "particles" as scatterers

since no new light is generated. In fact, Huygens postulated that the generation of light was the consequence of matter in rapid motion which, as we shall see shortly, is not far from our modern day understanding of light sources. The intuitive concept of an ether remained prevalent among scientists, but had finally to be refuted due to experimental results obtained by Michelson and Morley at the end of the nineteenth century. Their experiments indicated that the speed of light is constant thereby contradicting predicted anisotropies from ether based theories.

However, the wave concept of light has remained as one of the foundations of modern science and technology. The work of Faraday and Maxwell led to the discovery that light is an electromagnetic wave whose characteristics are well described by solving the Maxwell equations. These four equations describe how the electric field $\mathbf{E}$ and the magnetic field $\mathbf{H}$ depend on the volume density of electric charge ρ_c, the polarization of a medium $\mathbf{P}$, the magnetization of a medium $\mathbf{M}$, and the current density $\mathbf{J}$ [3]:

$$\nabla \cdot \mathbf{E} = -\frac{1}{\epsilon_0} \nabla \cdot \mathbf{P} + \frac{\rho_c}{\epsilon_0}, \tag{1.1}$$

$$\nabla \cdot \mathbf{H} = -\nabla \cdot \mathbf{M}, \tag{1.2}$$

$$\nabla \times \mathbf{E} = -\mu_0 \frac{\partial \mathbf{H}}{\partial t} - \mu_0 \frac{\partial \mathbf{M}}{\partial t}, \tag{1.3}$$

$$\nabla \times \mathbf{H} = \mathbf{J} + \epsilon_0 \frac{\partial \mathbf{E}}{\partial t} + \frac{\partial \mathbf{P}}{\partial t}. \tag{1.4}$$

Here ϵ_0 and μ_0 are the permittivity and permeability of the vacuum. In this thesis only nonmagnetic electrically neutral media are considered, therefore $\mathbf{M} = 0$, $\rho_c = 0$, and $\mathbf{B} = \mu_0 \mathbf{H}$. By taking the curl of Eq. (1.3) and then inserting Eq. (1.4) on the right hand side, the equation for electromagnetic waves is found

$$\nabla \times (\nabla \times \mathbf{E}) + \frac{1}{c^2} \frac{\partial^2 \mathbf{E}}{\partial t^2} = -\mu_0 \frac{\partial^2 \mathbf{P}}{\partial t^2} - \mu_0 \frac{\partial \mathbf{J}}{\partial t}, \tag{1.5}$$

$$-\nabla^2 \mathbf{E} + \frac{1}{c^2} \frac{\partial^2 \mathbf{E}}{\partial t^2} = -\mu_0 \frac{\partial^2 \mathbf{P}}{\partial t^2} - \mu_0 \frac{\partial \mathbf{J}}{\partial t}. \tag{1.6}$$

Where in the last step the vector identity $\nabla \times (\nabla \times \mathbf{V}) \equiv \nabla (\nabla \cdot \mathbf{V}) - \nabla \cdot (\nabla \mathbf{V})$ was used together with $\nabla \cdot \mathbf{E} = 0$, and $c = 1/\sqrt{\epsilon_0 \mu_0}$ is the speed of light in vacuum. Wave Eq. (1.6) lies at the heart of photonics research. It is used, *e.g.*, in the design of antennas on the nanometer scale [4–6], the development of higher resolution microscopes [7], the discovery and fabrication of optical metamaterials [8–10], and the understanding of the propagation of waves in complex photonic media [11]. With increasing complexity of photonic structures, solving the equation numerically can be a tremendous computational exercise and we shall often find the need to simplify matters considerably.

The right hand side term in Eq. (1.6) shows that electromagnetic waves are scattered, generated or absorbed by the acceleration of charges. The acceleration of charges can either take place by a changing current, $\mu_0 \frac{\partial \mathbf{J}}{\partial t}$, as is the case in metals, or a change in the polarization of the medium, $\mu_0 \frac{\partial^2 \mathbf{P}}{\partial t^2}$, as is the case in insulators, or by a combination of both as is the case in semiconductors. The frequency of the wave determines the type of electromagnetic radiation that is generated. Light forms just a small portion of the entire electromagnetic spectrum. Although light has the obvious advantage of being visible, it requires photonic structures to be in the nanometer range making the construction of these structures a serious technological challenge. Waves with a smaller frequency than light
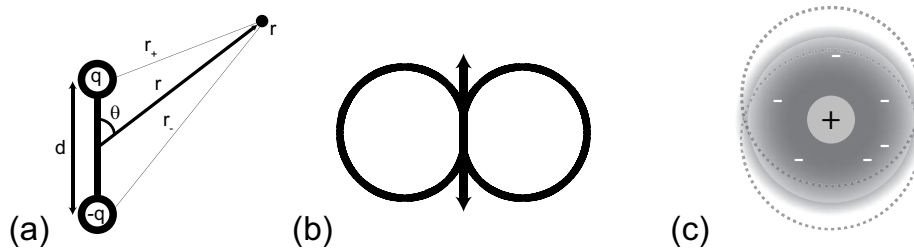
Figure 1.1: (a) An electromagnetic dipole consisting of two opposite charges q separated by distance d radiates to point $\mathbf{r}$. The distances from the two charges to the observation point are r_+ and r_- respectively. (b) The radiation pattern for a vertically aligned dipole, an iso-intensity contour is plotted in the $r\theta$-plane. (c) oscillating dipole sources for light can be formed by atoms in which a negatively charged electron cloud oscillates around the positively charged nucleus.

enable us to study similar phenomena on larger length scales while the underlying physics remains the same. In this thesis we describe experiments performed with visible light (400-790 THz) and microwaves (10 GHz).

To first order, electromagnetic sources are described by oscillating dipoles. An isotropically radiating point source is well approximated in the far field by an oscillating dipole. A classical dipole is therefore one of the most frequently used sources in photonics. In Sec. 1.1.1, the expressions of the fields for a point dipole are derived following a standard reference [12]. Oscillating dipoles can be induced in a variety of ways depending on the desired frequency. Dipole sources can be created by inducing oscillating currents in an antenna in the case of microwaves or by thermal and spontaneous emission in the case of light. The latter will be discussed in Sec. 1.1.2 and Sec. 1.1.3, and will be followed by a discussion on stimulated emission and absorption in Sec. 1.1.4.

1.1.1 Radiating point dipole

The wave equation deduced from the Maxwell equations showed that sources of radiation stem from either accelerating charges or changing currents. The oscillating dipole is the easiest example of such a source and it is frequently used to describe experimental configurations with atomic and molecular light sources. In this section the expressions for the fields of a radiating point dipole are derived [12] at a distant point $\mathbf{r}$ away from the dipole.

Consider two metal spheres connected by a thin wire of length d aligned along the z-axis with its center located at the origin as illustrated in Fig. 1.1(a); one sphere contains a charge $q(t)$, while the other sphere contains an opposite charge $-q(t)$. The charge on the spheres oscillates with angular frequency ω. The two spheres then form a dipole with oscillating dipole moment $\mathbf{p}(t) = p_0 \cos{(\omega t)}\,\hat{\mathbf{z}}$ where the amplitude is given by $p_0 \equiv q_0 d$. For an ideal point dipole it is assumed $d \ll \lambda \ll r$. In electrodynamics, the electric and magnetic fields at point $\mathbf{r}$ can be expressed in terms of the potential V and the vector potential $\mathbf{A}$

$$\mathbf{E} = -\nabla V - \frac{\partial \mathbf{A}}{\partial t}, \tag{1.7}$$

$$\mathbf{B} = \nabla \times \mathbf{A}. \tag{1.8}$$

11

The retarded potential of the dipole is given by

$$V(\mathbf{r}, t) = \frac{1}{4\pi\epsilon_0} \left\{ \frac{q_0 \cos\left[\omega\left(t - r_+/c\right)\right]}{r_+} - \frac{q_0 \cos\left[\omega\left(t - r_-/c\right)\right]}{r_-} \right\}, \tag{1.9}$$

$$V(r, \theta, t) \cong -\frac{p_0\omega}{4\pi\epsilon_0 c} \left(\frac{\cos\theta}{r}\right) \sin[\omega(t - r/c)]. \tag{1.10}$$

The second equation is the result of applying geometrical and Taylor approximations to Eq. (1.9) that follow from the criterion $d \ll \lambda \ll r$. The vector potential is given by the integral of the current density over the volume of the wire.

$$\mathbf{A}(\mathbf{r}, t) = \frac{\mu_0}{4\pi} \int \frac{\mathbf{J}(\mathbf{r}')}{|\mathbf{r} - \mathbf{r}'|} d\tau', \tag{1.11}$$

$$\mathbf{A}(r, \theta, t) \cong -\frac{\mu_0 p_0 \omega}{4\pi r} \sin\left[\omega(t - r/c)\right] \hat{\mathbf{z}}, \tag{1.12}$$

$$= -\frac{\mu_0 p_0 \omega}{4\pi r} \sin\left[\omega(t - r/c)\right] (\cos\theta \hat{\mathbf{r}} - \sin\theta \hat{\boldsymbol{\theta}}). \tag{1.13}$$

In the second step we used $|\mathbf{r} - \mathbf{r}'| \approx r$ when $d \ll r$. Putting the expressions for V and $\mathbf{A}$ into Eqs. (1.7) and (1.8) and discarding all higher order terms in $1/r$, returns the radiated electric and magnetic field by an ideal dipole.

$$\mathbf{E}(r, t) = -\frac{\mu_0 p_0 \omega^2}{4\pi} \left(\frac{\sin\theta}{r}\right) \cos[\omega(t - r/c)]\hat{\boldsymbol{\theta}}, \tag{1.14}$$

$$\mathbf{B}(r, t) = -\frac{\mu_0 p_0 \omega^2}{4\pi c} \left(\frac{\sin\theta}{r}\right) \cos[\omega(t - r/c)]\hat{\boldsymbol{\phi}}. \tag{1.15}$$

From these two equations, the radiated intensity is found by calculating the cycle-averaged Poynting vector $\mu_0 \mathbf{S} = (\mathbf{E} \times \mathbf{B})$

$$\langle \mathbf{S}(r, \theta) \rangle = \left(\frac{\mu_0 p_0^2 \omega^4}{32\pi^2 c}\right) \frac{\sin^2\theta}{r^2}\hat{\mathbf{r}}. \tag{1.16}$$

From this equation one understands that the intensity profile is shaped like a donut and the intensity falls off with r^2. In order for the dipole to act as a true source of radiation $\oint \langle \mathbf{S} \rangle d\mathbf{a} > 0$ where the integration runs over a closed surface containing the dipole, in words this condition implies radiation is created by the source. The divergence theorem, $\oint \langle \mathbf{S} \rangle d\mathbf{a} = \int \nabla \cdot \langle \mathbf{S} \rangle d\tau$, allows us to analyze the divergence of the Poynting vector instead. Since $\nabla \cdot r^{-2}\hat{\mathbf{r}} = 4\pi\delta(\mathbf{r})$ with $\delta(\mathbf{r})$ the Dirac delta function, the divergence of a classical dipole reads

$$\nabla \cdot \langle \mathbf{S} \rangle = \frac{\mu_0 p_0^2 \omega^4}{12\pi c}\delta(\mathbf{r}), \tag{1.17}$$

from which we conclude a classical point dipole indeed acts as a source for electromagnetic radiation. However, reciprocity implies that a classical dipole can also be excited by radiation. An excited dipole will of course also radiate. Conservation of energy dictates that for an excited dipole without dissipation $\int \nabla \cdot \langle \mathbf{S} \rangle d\tau = 0$. Hence, the oscillating dipole, although described by the same equations, has turned from a source into a scatterer. Scattering objects that are much smaller than the wavelength are well described by dipole scattering and are referred to as Rayleigh scatterers [13]. The physics of these relatively small scatterers is all around us and can be witnessed every day. The frequency dependence of the scattered power in Eq. (1.16) leads to the blue color of the sky, while the angle dependence causes scattered light from the sky to be partially polarized. We will come back to the physics of scattering particles in Sec. 1.2.1.

1.1.2 Spontaneous emission and vacuum fluctuations

Since the frequency of dipole radiation is simply given by the frequency of the oscillating charges, low frequency waves can easily be generated electronically at arbitrary frequencies with the right circuit design. The engineering and fabrication of antennas has become a major industry that covers the low end of the electromagnetic spectrum consisting of radiowaves and microwaves. The difficulty of fabricating higher frequency sources by this method is one of the main reasons for the fact that the THz part of the electromagnetic spectrum was relatively hard to study in the past [14]. For infrared and visible light, high frequency oscillating dipoles can be formed by oscillating electron clouds in molecules and atoms as illustrated in Fig. 1.1(c) [15]. In nature, the main source for accelerating charges that emit light is due to thermal excitation. Every object with a nonzero absolute temperature radiates electromagnetic waves in thermal equilibrium, the sun and incandescent light bulbs are two everyday examples of these so-called black body radiators. Spontaneous emission of radiation can occur when excited atoms and molecules fall back to a lower energy state.

Until now we have described the physics of electromagnetism classically. However, spontaneous emission requires a quantum mechanical treatment of both the field and the atom in order to be in correspondence with experiment [16, 17]. A semiclassical description of spontaneous emission, in which the fields are treated classically and the atom quantum mechanically, essentially fails because according to such a model an atom in the excited state $|\psi_2\rangle$ is in an unstable equilibrium and would therefore never fall back to the ground state $|\psi_1\rangle$ [16]. In quantum electrodynamics even vacuum modes contain fluctuating electromagnetic fields that perturb an excited atom. These perturbations will sooner or later force the atom to leave its unstable equilibrium and to undergo a transition to the ground state while simultaneously sending out radiation in the form of a photon[1]. The precise moment an atom decays by spontaneous emission is unpredictable, yet the average rate at which an atom decays is well described by quantum electrodynamics. Obviously the higher the number of modes that interact with the atom, the shorter it takes on average for an atom to decay. When the electromagnetic modes form a continuum, the average radiative decay of an excited atom at position $\mathbf{r}$ and transition dipole moment d is described by an exponential of which the decay rate γ_r is given by Fermi's Golden Rule

$$\gamma_r(\mathbf{r}, \omega, \hat{\mathbf{d}}) = \frac{\pi d^2 \omega}{h \epsilon_0} \rho(\mathbf{r}, \omega, \hat{\mathbf{d}}). \tag{1.18}$$

In this expression, ρ is the local density of electromagnetic radiative states (LDOS). The LDOS gives the number of states per unit volume to which an atomic oscillating dipole positioned at $\mathbf{r}$, oriented along $\hat{\mathbf{d}}$, and with frequency ω can couple.

Fermi's Golden Rule yields another cornerstone of the field of photonics. The first part of Eq. (1.18) $\frac{\pi d^2 \omega}{h \epsilon_0}$ is an atomic factor, which in practice can hardly be altered without operating at the Ångstrom scale. However, by engineering the LDOS photonically one can gain control over the emission characteristics of an emitter with structures on the order of a wavelength [18]. The LDOS might appear an exotic quantity at first glance, yet a plain mirror can already change the LDOS significantly. The decay rate of an atom in proximity

---

[1]Since spontaneous emission is a fully quantum mechanical process, the term photon in this context is justified. Occasionally and mainly to increase the readability of the text, we shall use the term photon when in principle a semiclassical description suffices and there is in principle no need for speaking about photons instead of energy density.
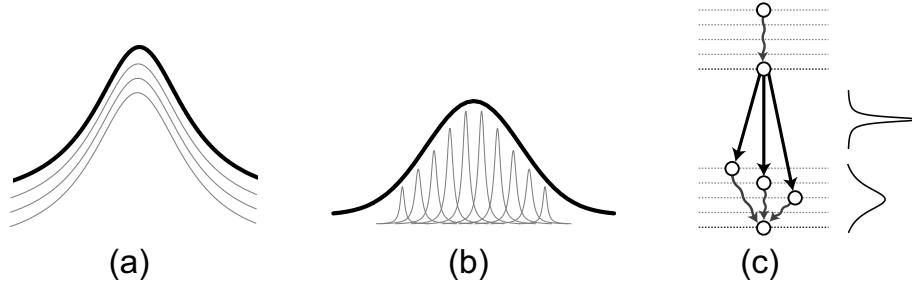
Figure 1.2: The emission spectrum from a collection of molecules or atoms can be broadened by (a) homogeneous broadening processes or (b) inhomogeneous broadening processes, or a combination of both. In the case of homogeneous broadening the linewidth is broadened for each individual emitter (gray lines) in a similar fashion. The output spectrum for a collection of emitters (black line) is therefore identical to the output spectrum of an individual emitter. Inhomogeneous broadening is caused by emitters having different center frequencies (gray lines). (c) In a four-level system the emitter quickly relaxes to the lower level of the excited state (wiggly arrow) from which it can undergo a radiative transition (straight arrows) to several vibrational sublevels of the ground state. From these vibrational sublevels the molecule relaxes back to the lowest level of the ground state. The spread in sublevels of the ground state is responsible for a significant homogenous broadening of the emission spectrum.

($\sim \lambda$) of a mirror oscillates as a function of its separation distance [19, 20]. In 3D photonic crystals with a high enough photonic contrast the LDOS vanishes completely leading to a photonic band gap in which atoms theoretically cease to decay at all. Recently it was shown experimentally that a photonic band gap can reduce the average decay rate by more than a factor 10 [21].

1.1.3 Non-radiative decay: quantum efficiency and spectral broadening

Besides undergoing a radiative transition from a higher energy state to a lower energy state via the process of spontaneous emission, atoms and molecules can, in general, also relax to a lower energy state by non-radiative transitions. Examples of processes that cause non-radiative transitions include lattice vibrations and molecular collisions [15, 16]. The quantum efficiency ϕ is a quantitative measure for how much energy flows into the radiative decay channel in comparison to non-radiative decay channels and is defined by

$$\phi \equiv \frac{\gamma_r}{\gamma_r + \gamma_{\mathrm{nr}}}, \tag{1.19}$$

where γ_{nr} is the non-radiative decay rate. From an experimental point of view high quantum efficiency sources are often the emitters of choice in photonics. Not only because they simply return more light, but also because they are more convenient probes for measuring changes in the LDOS by performing lifetime measurements. A change in the LDOS results in a different value for the radiative decay rate and thereby changes the ratio between radiative and non-radiative decay. However, when the non-radiative decay channels are strongly dominating over the radiative channel, any change in the radiative decay rate will be hard to detect since lifetime measurements probe the total decay rate $\gamma_{\mathrm{tot}} = \gamma_r + \gamma_{\mathrm{nr}}$, which is then hardly affected.

Non-radiative transitions within an emitter also have a significant impact on its emission spectrum. The spectrum of an ideal two-photon emitter with amplitude decay rate $\gamma_{\mathrm{tot}}/2$ is given by the Fourier transform of an exponential which has a complex Lorentzian line shape

with a characteristic Full-Width at Half-Maximum (FWHM) linewidth of γ_{tot} [15, 22]. In practice and especially at room temperature, the width of an emission spectrum is broader than this value. The spectrum collected from an ensemble of emitters can broaden due to the spectral broadening of each individual emitter, or because the individual emitters emit at different center frequencies as illustrated in Fig. 1.2(a) and (b). The first case is referred to as homogeneous broadening, the second case is called inhomogeneous broadening.

The light sources used in this thesis are dye molecules which form a four-level system. Figure 1.2(c) provides a schematic illustration of the decay processes in such a four-level system. An excited four-level emitter relaxes to the lowest level of the excited state by non-radiative transitions from which it decays (partly) radiatively to a vibrational sublevel of the ground state. The presence of these vibrational sublevels of the ground state are the main broadening mechanism for these type of emitters [23, 24]. Although the lifetime of the lowest excited state is relatively long (order of nanoseconds) and would give rise to a narrow spectrum ($\Delta\lambda \sim 1$ nm), the vibrational sublevels enable each molecule to undergo radiative transitions with widely varying energies leading to a broader spectrum. Typical four-level emitters therefore exhibit a long lifetime and a homogeneously broadened frequency spectrum ($\Delta\lambda \sim 50$ nm).

1.1.4 Stimulated emission, absorption, and elastic scattering

Just as vacuum fluctuations of the electromagnetic field modes are able to induce radiation from an atomic or molecular dipole, so are higher energy eigenstates of the electromagnetic modes with the same frequency. We then speak of stimulated transitions and in contrast to spontaneous emission, these transitions are not intrinsically quantum mechanical, they are as accurately described in a semiclassical framework. In the semiclassical picture, the incident field creates an oscillating dipole in the atom, which originates from the superposition of two atomic eigenstates $|\psi_1\rangle$ and $|\psi_2\rangle$ with different energies, $E_2 > E_1$. As a consequence the oscillating dipole starts radiating itself and this radiation can either be in-phase or out-phase with the incident radiation. A collection of in-phase oscillating dipoles interferes constructively with the incident field leading to an enhancement of the field, whereas a collection of out-phase dipoles interferes destructively and leads to an attenuation of the incident field [15]. These coherent processes are referred to as stimulated emission for the in-phase case and stimulated absorption for the out-phase case, yet they stem from the same dipole excitation and therefore have equivalent transition probabilities. Stimulated absorption lets the atomic system end up in the energetically excited state $|\psi_2\rangle$, while stimulated emission let the atomic system end up in the energetically lower state $|\psi_1\rangle$. When a population of atoms is considered with N_1 atoms in the ground state and N_2 atoms in the excited state stimulated emission and absorption occur simultaneously. If N_1 initially exceeds N_2 incident radiation is attenuated, if however the situation is reversed radiation is amplified. In the latter case of amplification, the population is said to be inverted.

When either of these two processes occur the original phase of the field is preserved by the oscillating dipoles of the atoms or molecules. The oscillating dipoles can easily loose their phase information however by non-radiative transitions, collisions, and spontaneous emission. This process is called dephasing and for the experiments described in this thesis, dephasing happens on order of magnitude shorter time scales than the stimulated radiative processes. Due to dephasing, the emission from a collection of in-phase excited molecules will be due to incoherent spontaneous emission.
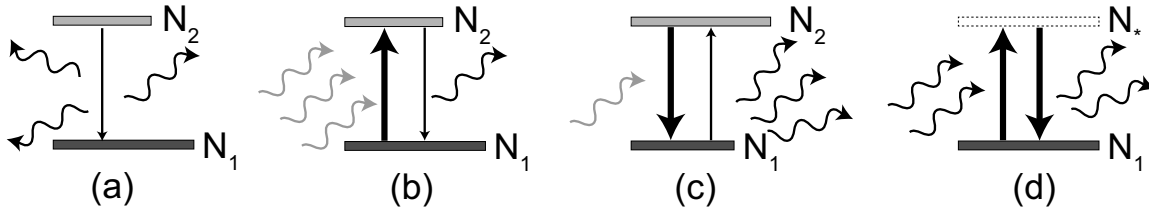
Figure 1.3: Illustration of the different interactions of light and a collection of atoms for (a) spontaneous emission, (b) and (c) stimulated transitions and (d) elastic scattering. (a) Atoms populating the higher energy state can fall back to the ground state while radiating light due to perturbations caused by vacuum fluctuations. (b) When the population of atoms in the lower energy state is higher than the population of atoms in the higher energy state, incident radiation is attenuated because stimulated absorption dominates over stimulated emission. (c) Population inversion leads to amplification of the incident radiation where the radiated waves are in-phase with the incident waves. (d) When atoms scatter light, the population of the lower energy level does not change. Excitation of virtual energy levels is followed by immediate reradiation.

The change in energy level of the atom clearly distinguishes stimulated transitions from elastic scattering processes. Elastic scattering is also due to oscillating dipoles that are induced by an electromagnetic field. However, in the case of elastic scattering the energy of the particle does not change. In order to describe scattering in terms of energy states, the particle is said to be excited by the incident light to a *virtual* energy state from which the particle immediately falls back to its real state while reradiating. Since the atom never populates a higher energy state in reality, dephasing does not occur and the reradiated light is in phase with the incident light. The difference between scattering, stimulated emission, stimulated absorption, and spontaneous emission is summarized in Fig. 1.3. For closely isotropically packed scattering atoms in a dielectric (separation distance $\ll \lambda$) incident light is therefore hardly affected apart from obtaining a different speed, which can be derived from Maxwell's equations by considering a homogeneous polarizability [3]. When scatterers are randomly positioned in a medium with separation distances on the order of a wavelength or longer, the propagation of waves is drastically altered. The propagation of waves through such an inhomogeneous, scattering medium is the subject of Sec. 1.2, but we will first discuss how stimulated emission is utilized in a laser, one of the most important contemporary artificial sources of radiation.

1.1.5   Lasers

The term laser is an acronym for "Light Amplification by Stimulated Emission of Radiation". The idea of amplifying radiation by stimulated emission was originally conceived and put to practice in the microwave part of the electromagnetic spectrum [25]. Theodore Maiman built the first operating laser for visible light in 1960 [26] using a flash lamp and a ruby crystal as an amplifying medium.

Although lasers vary widely in design and operation, they all consist of three essential ingredients: a gain medium that leads to amplification of radiation, a spectrally selective feedback mechanism that enhances the interaction between light of a certain frequency and the gain medium, and a pump that provides the energy for the excitation of the gain medium.

In practice, most conventional lasers have a gain medium that consists of a collection of atoms or molecules that is population inverted [27] and a cavity consisting of high-quality
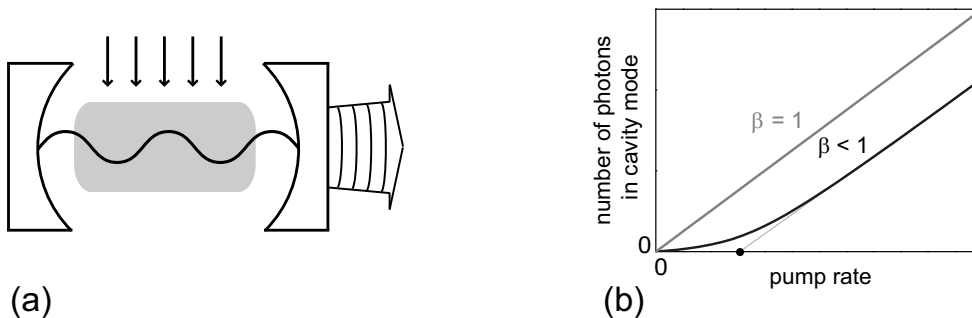
Figure 1.4: (a) Illustration of a conventional laser. A pump mechanism (small black arrows) is used to create a population inversion in the gain medium (gray block). Two mirrors form a cavity which provides feedback for its modes. Light is amplified by stimulated emission in the gain medium. A small part of the amplified radiation is transmitted through one of the mirrors. (b) The output power of a laser for two different values of the spontaneous emission factor β. For $\beta = 1$ (gray line) there is no threshold in the output power. For $\beta < 1$ (black line) a threshold can be defined by the crossing of the extrapolated above threshold output power (dotted line) and the x-axis as indicated by the black dot.

mirrors that provides the feedback for the resonant cavity mode as shown in Fig. 1.4(a). The dynamics of the number of molecules in the upper laser level and the energy in the cavity mode are related. For a single-mode laser with a unit quantum efficiency four-level gain medium, the number of photons q in the cavity mode and the number of molecules in the upper laser level N are given by [15]

$$\frac{dq}{dt} = -\gamma_c q + \beta N \gamma_r q + \beta N \gamma_r, \tag{1.20}$$

$$\frac{dN}{dt} = R - \beta N \gamma_r q - N \gamma_r, \tag{1.21}$$

with steady-state solution

$$q = -\frac{1}{2\beta} + \frac{R}{2\gamma_c} + \frac{1}{2}\sqrt{\left(\frac{1}{\beta} - \frac{R}{\gamma_c}\right)^2 + 4\frac{R}{\gamma_c}}. \tag{1.22}$$

Here γ_c is the cavity decay rate, R is the pump rate, and β is the spontaneous emission factor, which describes what the probability is that a spontaneously emitted photon ends up in the cavity mode. For a conventional laser this β-factor lies between 10^{-7} and 10^{-10} [15]. Spontaneous emission is essential in most lasers, since it provides the seed for amplification.

A plot of the steady-state solution to rate Eqs. (1.20)-(1.21) in Fig. 1.4(b) reveals that the number of photons is strongly dependent on the pump rate when $\beta < 1$. A pump threshold can be defined, $R_{\text{th}} = (1/\beta - 1)\gamma_c$, above which the number of photons starts to increase rapidly as a function of pump power. At threshold the gain in the system compensates for the losses in the cavity mode. Above threshold, stimulated emission has become the most important source of radiation and the laser mode thereby prevents that excited molecules "loose" there energy to unwanted spontaneous emission outside the cavity mode. Since radiation induced by stimulated emission is in phase with the incident radiation, the laser light can become highly coherent in both time and space. For the peculiar case of $\beta = 1$, the situation is different. Every emitted photon ends up in the cavity mode by definition and therefore the threshold in the output power disappears.

1.2 Random photonic media

The strive for perfectly ordered and clean structures has been deeply entrenched in optics. Scattering due to structural inhomogeneities or particles is indeed detrimental to many optical devices, such as glass lenses, metallic mirrors, and conventional lasers, and therefore preferably avoided. In our encounter with nature, however, scattering of electromagnetic radiation is all around us and simply cannot be neglected. Not surprisingly, the research on multiple light scattering has long been dominated by astrophysicists for whom knowledge of electromagnetic wave scattering is needed to uncover essential information about stellar systems [11, 28].

Despite the ongoing experimental efforts to fabricate nearly perfectly ordered photonic structures, it is inevitable that any man-made structure contains disorder to some extent. This unavoidable presence of disorder limits the performance of, *e.g.*, photonic crystals whose design is based intrinsically on order [29, 30]. The exciting promises of the field of metamaterials such as cloaking and negative index materials are also based on the assumption of perfect order, and it remains to be seen whether these promises are feasible when some disorder is taken into account [31, 32].

Instead of taking order as a starting point of science and technology, one might as well accept the presence of disorder from the beginning and try to use it to one's advantage. This idea of perceiving disorder as a strength rather than a weakness, has become more widespread in recent years. Introducing disorder by design has enabled a strong interaction between single photons and single quantum emitters via Anderson localized modes [33] and has led to the observation of transverse Anderson localization [34]. In the microwave regime, the time-reversal of scattered waves originating from a point source was shown to lead to focussing beyond the diffraction limit [35]. In optics, where time-reversal of waves is far from trivial, it was shown that manipulating the amplitude and phase of a wavefront by spatial light modulators and appropriate feedback algorithms can lead to sharp focussing outside [36, 37] and inside [38] a scattering medium. This wavefront shaping technique has been further developed and in combination with high refractive index scattering media it allows for sub-100 nm microscopy [39]. Using the technique of wavefront shaping the transmission matrix describing the transmission of light through random media was determined, allowing for the imaging of objects through opaque media [40].

Besides the development of these revolutionary disorder based technologies, the physics of wave transport through disordered systems is exciting and worth studying in itself. A better understanding of the propagation of waves in multiple scattering media explains the appearance of many objects surrounding us and the transition from metals to insulators. Rather than solving Maxwell's equations by brute force as for example done by Finite-Difference Time-Domain calculations (FDTD) [41], which in principle would lead to precise predictions of light transport in random media, we prefer to seek accurate analytical descriptions by reducing the complexity of the system from the start. In this section we first study how single particles scatter light in Subsec. 1.2.1. The transport mean free path is introduced as the essential quantity for describing multiple scattering of light in Subsec. 1.2.2. We then discuss how both a particle and wave like description of electromagnetic radiation passing through a collection of single scatterers lead to diffusion in Subsec. 1.2.3 and Subsec. 1.2.4, and finally how the incorporation of interference leads to Anderson localization in Subsec. 1.2.5.
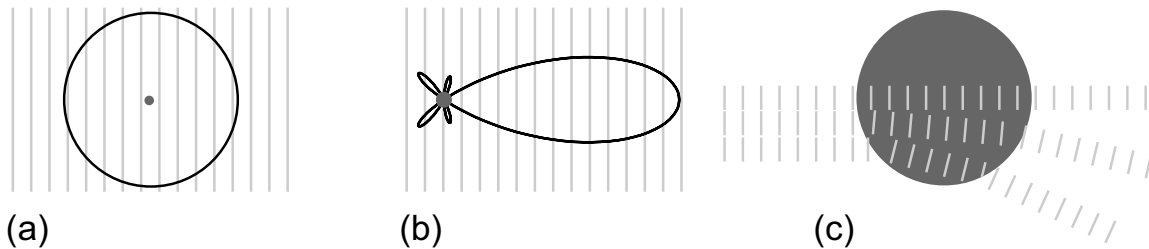
Figure 1.5: The size of a scatterer determines its scattering function. (a) For particles much smaller than the wavelength the scattering is governed by Rayleigh scattering. The scattering is isotropic in the plane perpendicular to the polarization. (b) Particles with a size on the order of the wavelength are in the Mie-regime. The scattering function is very dependent on angle. (c) When the size of the particle is much larger than the wavelength ray optics can be used to describe the scattering process.

1.2.1 Single scattering

The way scattering from a particle is described depends on its size with respect to the wavelength and the refractive index contrast between the particle and the surrounding medium. We define the size parameter $x \equiv ka$ with a the characteristic length of the particle and $k \equiv \omega/c$ the wave number of the wave. For spherical particles a is given by the radius. The three regimes of single particle scattering are illustrated in Fig. 1.5 and explained below. When a scattering particle is much smaller than the wavelength ($x < 1$), the particle is said to be in the Rayleigh regime and can be treated as a dipole for which we have already calculated in Sec. 1.1.1 that the radiation pattern is isotropic in the plane perpendicular to the orientation of the dipole. The polarizability α of the particle[2] determines the strength of the induced dipole moment by

$$\mathbf{p} = \alpha \mathbf{E}. \tag{1.23}$$

The cross section of a scatterer is a quantitative measure for the strength of a scatterer. The scattering cross section σ_ℓ is defined as the ratio between the power taken out of an incident wave by scattering and the intensity I_0 of the incident wave [28]. By the same token we can define an absorption cross section σ_a by considering the power taken out of an incident wave by absorption. By using Eq. (1.23), Eq. (1.17), and $I_0 \equiv \frac{1}{2}c\epsilon_0 E_0^2$, we find the scattering cross section of a Rayleigh scatterer

$$\sigma_s \equiv \frac{P}{I_0} = \frac{|\alpha|^2 k^4}{6\pi\epsilon_0^2}. \tag{1.24}$$

This relation emphasizes again that in the Rayleigh regime the scattering of particles becomes stronger for shorter wavelengths.

When particle sizes become on the order of a wavelength, the dipole approximation used for Rayleigh scatterers breaks down. One can still view the particle as a collection of dipoles and determining its scattering properties essentially comes down to adding up the contribution from every individual dipole while taking into account interactions between the dipoles themselves [13]. The scattered radiation will show strong fluctuations with angle due to constructive and destructive interference, and will therefore be very anisotropic.

---

[2]In general the polarizability of a particle is a tensor. Here we only consider particles that have isotropic polarizability, in which case the tensor can be treated as a scalar.
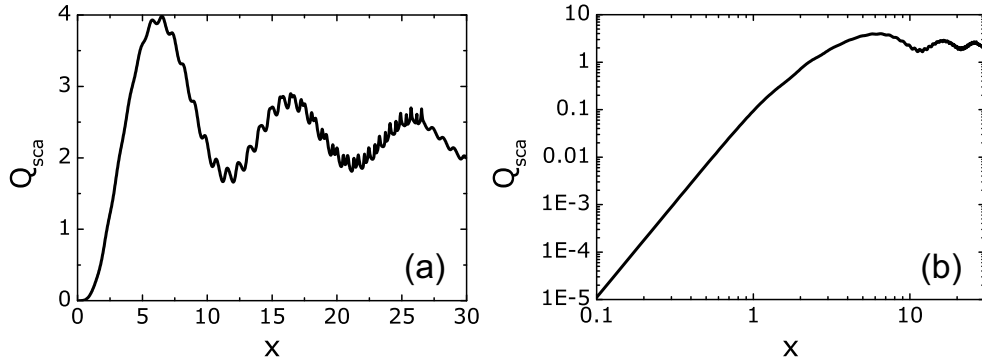
Figure 1.6: The scattering cross section of a sphere normalized to its geometrical cross section versus size parameter on (a) a linear plot and (b) a log-log plot. The linear plot shows how resonances appear when $x > 1$. The logarithmic plot illustrates the λ^{-4} dependence of the cross section when $x < 1$. When $x \gg 1$ the scattering cross section becomes twice the geometrical cross section. The plots are calculated using Mie-theory with $n = 1.33$ for the sphere and $n = 1$ for the environment.

The exact radiation pattern and the scattering cross section of such a scatterer can only be calculated analytically for spheres and cylinders by using Mie-theory [13, 28, 42]. The strong dependence on wavelength for these type of scatterers results in spectral resonances of the scattering cross section as shown in Fig. 1.6 where we have plotted the calculated scattering cross section as a function of size parameter. In these plots the Mie-regime can be clearly identified by the numerous valleys and peaks. The logarithmic plot of the cross-section highlights the λ^{-4} dependence of the cross-section in the Rayleigh regime.

Scatterers much larger than the wavelength fall within the geometrical optics regime and can be analyzed by ray optics. For example, the scattering from rain droplets is described by this regime and enables us to explain the intricate structure of rainbows. A main somewhat paradoxical feature of large scatterers is the fact that their scattering cross section is twice their geometrical cross section [28] due to the diffraction of waves at the edges of its geometrical shadow. The calculations shown in Fig. 1.6 indeed indicate that the scattering cross section becomes twice the geometrical cross section for $x \gg 1$.

1.2.2 Multiple scattering and random walks

When a system with characteristic length scale L contains more than one scatterer, waves have the possibility of scattering more than once. This probability increases when the density n of scatterers is increased or when the scattering cross section of the individual scatterers becomes larger, because the average path length between two scattering events then decreases. This length is called the scattering mean free path ℓ_s and is given by

$$\ell_s = \frac{1}{n\sigma_s}. \tag{1.25}$$

A sample is in the multiple scattering regime when $\ell_s < L$. In the previous section we have seen that particles do not necessarily scatter isotropically. Mie-spheres for example scatter preferentially in the forward direction. It therefore can take more than just one scattering event to completely randomize the wave's direction. The traversed length that is required to loose all information about the input wave's initial direction, is called the transport mean free path ℓ. This important quantity can be found by normalizing the scattering mean free
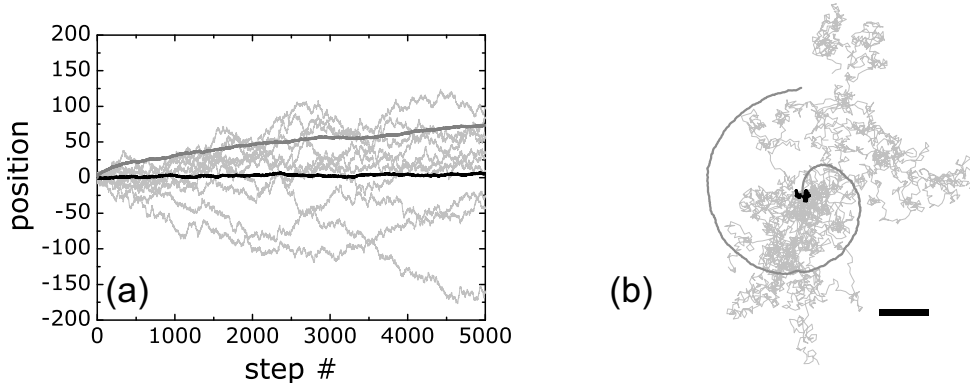
Figure 1.7: Random walks in (a) 1D and (b) 2D with unit step size. The light gray curves are examples of 10 random walks in 1D and 8 in 2D with 5000 and 500 steps respectively. The black curves are the ensemble averages over 100 samples. The dark gray curves indicate the root mean square of the displacement, which has been parameterized in the 2D case. The black bar equals 10 unit steps.

path with the average cosine of the scattering angle:

$$\ell = \frac{\ell_s}{1 - \langle \cos \theta \rangle}. \tag{1.26}$$

A medium remains (partly) transparent as long as $\ell > L$. For opaque media on the other hand the transport of waves is dominated by multiple scattering. Describing the exact wave propagation through such a complex medium obviously becomes a hopeless endeavor, which only the naivety of a computer might resolve. We shall need to introduce approximations and secondly mainly study the properties of ensemble averages, in order to not leave the physical understanding out of sight.

A simple description of wave transport in random media can be obtained by ignoring the wave character of electromagnetic radiation altogether. In this picture, the radiation is treated as a particle and the scatterers simply change the direction of these particles from one k-vector to another as if the multiple scattering medium is playing a pinball game with the wave. The radiation "particle" undergoes a random walk [43, 44] through the medium with an average step size ℓ. At every step i the wavevector changes direction which we indicate by a unit vector with random orientation $\hat{\mathbf{k}}_\mathbf{i}$. Figure 1.7 shows examples of random walks in 1D and 2D. By averaging over a large number N of these stochastic processes, one is able to obtain accurate approximations for the energy density in a random medium in many situations. For example, one can deduce that for isotropic random walks the mean position $\langle \mathbf{r} \rangle$ after n steps is the starting point by realizing $\langle \mathbf{r}(n) \rangle = \frac{1}{N} \sum_{i=1}^{N} \left[\mathbf{r_i}(n-1) + \ell \hat{\mathbf{k}}_\mathbf{i} \right] = \langle \mathbf{r}(n-1) \rangle = \langle \mathbf{r}(0) \rangle$, because $\hat{\mathbf{k}}_\mathbf{i}$ averages out to zero. A similar argument for the mean-square of the position yields $\langle |\mathbf{r}(n)|^2 \rangle = \frac{1}{N} \sum_{i=1}^{N} \left[|\mathbf{r}_i(n-1)|^2 + 2\ell \hat{\mathbf{k}}_\mathbf{i} + \ell^2 \right] = \langle |\mathbf{r}(n-1)|^2 \rangle + \ell^2 = n\ell^2$, which shows that the average distance to the starting point scales with the square root of steps [44]. These two properties of isotropic random walks can also clearly be seen in the ensemble averaged curves in Fig. 1.7.

1.2.3 Particle diffusion

If the concentration $C(\mathbf{r}, t)$ of particles that undergo a random walk is not spatially uniform, the flow per unit area $\mathbf{J}$ of particles is towards creating spatial homogeneity. This general

property of a collection of randomly walking particles is known as Fick's first law and is mathematically formulated as

$$\mathbf{J} = -D\nabla C, \tag{1.27}$$

where D is the diffusion constant which is proportional to both the step size of the random walks and the speed of the particles. In a medium where no particles are created or annihilated any change of concentration at a certain point must be due to a net flow of particles through the infinitesimal surface surrounding the point:

$$\frac{\partial C}{\partial t} = -\nabla \cdot \mathbf{J}, \tag{1.28}$$

$$\frac{\partial C}{\partial t} = D\nabla^2 C. \tag{1.29}$$

Here we have used Eq. (1.27) to obtain Fick's second law in Eq. (1.29), better known as the classical diffusion equation. This versatile equation is omnipresent in all exact sciences, its applications vary from describing heat conduction [45] and molecular transport in cells [43] to price fluctuations in stock markets [46]. A source term S can be incorporated by adding it up to the right hand side of Eq. (1.29). If a time-independent unit source is placed at the origin $\delta(\mathbf{r} - \mathbf{r}')$ of an infinite medium, Eq. (1.29) reduces to the Poisson equation whose solution is given by $C(\mathbf{r}) = \frac{1}{4\pi D|\mathbf{r}|}$.

1.2.4 Wave diffusion

Diffusion is an unavoidable phenomenon in the case of a collection of particles performing an isotropic random walk. Any random-walk-like description of radiation will therefore inevitably end up with some form of the diffusion equation after averaging over disorder. However electromagnetic radiation is a wave in the first place and we have not yet justified that Eq. (1.29) applies to wave propagation in random media. Coherent waves propagating through random media give rise to a very irregular intensity pattern known as speckle, that is caused by constructive and destructive interference at random positions. In order to understand why waves diffuse, the wave nature needs to be taken into account from the start and speckles need to be averaged out. Rather than using the vector wave Eq. (1.6) found in Sec. 1.1, we treat the waves as a scalar[3] by considering the Helmholtz equation for monochromatic wave amplitude $\Psi(\mathbf{r}, t) = \psi(\mathbf{r})e^{i\omega t} + \text{c.c.}$

$$\nabla^2 \Psi - \frac{\epsilon(\mathbf{r})}{c^2}\frac{\partial^2 \Psi}{\partial t^2} = 0, \tag{1.30}$$

$$-\nabla^2 \psi - \frac{\omega^2}{c^2}\epsilon(\mathbf{r})\psi = 0, \tag{1.31}$$

with $\epsilon(\mathbf{r})$ the dielectric constant and ω the frequency of the wave. The solution to Eq. (1.31) depends on the variation of dielectric constant over space and our goal is to find it in a multiple scattering medium in which the dielectric constant fluctuates strongly and where a unit source is placed at the origin. In the wave equation above, it is implicitly assumed that the scatterers and the surrounding medium have a constant, but different, dielectric constant. This assumption allows us to neglect a term containing the gradient of the dielectric constant [47]. A more extensive treatment of the theory in this section can

---

[3]By writing the electromagnetic waves as a scalar, the polarization of the waves is ignored.

be found in the review by Van Rossum and Nieuwenhuizen [48] and the article by Van der Mark *et al.* [49]. We adopt the same sign convention as Ref. [50]. For simplicity reasons, point scatterers embedded in an environment with $\epsilon = 1$ are assumed in what follows. Thus for a scatterer at position $\mathbf{R_j}$ we have $\epsilon(\mathbf{r}) = 1 + \mu\delta(\mathbf{r} - \mathbf{R_j})$ where μ is a constant with dimension volume.

Amplitude propagation

Before considering the propagation of waves from a unit source in a multiple scattering medium, let us first study the propagation from a unit source in free space. The free space propagator is also known as the bare Green function and due to its importance this function receives its own symbol $g(\mathbf{r})$

$$-\nabla^2 g - \frac{\omega^2}{c^2}g = \delta(\mathbf{r}), \tag{1.32}$$

$$g(\mathbf{r}) = \frac{e^{i\frac{\omega}{c}|\mathbf{r}|}}{4\pi|\mathbf{r}|}, \tag{1.33}$$

where the solution has been obtained after solving the first equation in Fourier space and transforming back. The solution for the wave amplitude when a collection of sources $S(\mathbf{r})$ is present is then simply given by the superposition principle

$$\psi(\mathbf{r}) = \int g(\mathbf{r}, \mathbf{r}')S(\mathbf{r}')d\mathbf{r}'. \tag{1.34}$$

If a single point scatterer with $V(\mathbf{r}) \equiv V\delta(\mathbf{r} - \mathbf{R_j}) = \mu\frac{\omega^2}{c^2}\delta(\mathbf{r} - \mathbf{R_j})$ is introduced into the system at point $\mathbf{R_j}$, one can rewrite Eq. (1.31) as $-\nabla^2\psi - \frac{\omega^2}{c^2}\psi = V(\mathbf{r})\psi$. By using $V(\mathbf{r})\psi$ as the source term in Eq. (1.34), we find an iterative equation for the wave amplitude at point $\mathbf{r}$

$$\psi(\mathbf{r}) = \psi_0(\mathbf{r}) + \int g(\mathbf{r}, \mathbf{R_j})V\delta(\mathbf{r}' - \mathbf{R_j})\psi(\mathbf{r}')d\mathbf{r}', \tag{1.35}$$

$$= \psi_0(\mathbf{r}) + g(\mathbf{r}, \mathbf{R_j})V\psi(\mathbf{R_j}), \tag{1.36}$$

$$= \psi_0(\mathbf{r}) + g(\mathbf{r}, \mathbf{R_j})t\psi_0(\mathbf{R_j}). \tag{1.37}$$

Here ψ_0 is the solution of the wave equation without the scatterer present, and t has been introduced as part of the single particle scattering matrix t_j given by[4]

$$t_j(\mathbf{r_1}, \mathbf{r_2}) = \delta(\mathbf{r_1} - \mathbf{R_j})\delta(\mathbf{R_j} - \mathbf{r_2})t, \tag{1.38}$$

$$t = V + Vg(\mathbf{R_j}, \mathbf{R_j})V + Vg(\mathbf{R_j}, \mathbf{R_j})Vg(\mathbf{R_j}, \mathbf{R_j})V + \dots \tag{1.39}$$

The scattering matrix contains the properties of a single scatterer as described in Sec. 1.2.1. For a point scatterer this t as given by Eq. (1.39) is ill-defined, because the real part of $g(\mathbf{R_j}, \mathbf{R_j})$ blows up. The t-matrix is therefore often approximated by considering only the first two terms and by replacing the infinite real part of the second term by a finite term. In the remainder of this section, we will simply describe a single scatterer by its t-matrix without making its form explicit.

---

[4]The polarizability of a real scatterer depends strongly on frequency as discussed in Sec. 1.2.1. The t-matrix is therefore also frequency dependent. To keep the notation concise we do not show this frequency dependence explicitly in the text.

With the description of single scattering at our disposal, let us now seek expressions for the wave amplitude inside a medium containing N scatterers with a unit source at $\mathbf{r}'$. The amplitude full Green function $G(\mathbf{r}, \mathbf{r}')$ is the solution to

$$-\nabla^2 G(\mathbf{r}, \mathbf{r}') - \left[\frac{\omega^2}{c^2} + \sum_{j=1}^{N} V_j(\mathbf{r}) \right] G(\mathbf{r}, \mathbf{r}') = \delta(\mathbf{r} - \mathbf{r}'). \tag{1.40}$$

Again, this equation can be rewritten as an iterative equation

$$G(\mathbf{r}, \mathbf{r}') = g(\mathbf{r}, \mathbf{r}') + \int g(\mathbf{r}, \mathbf{r_1}) \sum_{j=1}^{N} V_j(\mathbf{r_1}) G(\mathbf{r_1}, \mathbf{r}') d\mathbf{r_1}. \tag{1.41}$$

This equation considers all possible combinations of scattering from particle to particle. Some of these combinations have already been encountered in building up the t-matrix of a single scatterer, namely the repetitive scattering of waves from one scatterer. To simplify matters considerably, we neglect all recurrent scattering terms in Eq. (1.41): a wave does not return to the same scatterer once it has encountered another scatterer. An insightful way of visualizing this so-called Independent Scattering Approximation (ISA) is by using Feynman diagrams

$$G_{\text{ISA}}(\mathbf{r}, \mathbf{r}') = \quad - \quad + \quad -\times- \quad + \quad -\times-\times-$$
$$+ \quad -\times-\times-\times- \quad + \ldots \tag{1.42}$$

The lines indicate the bare Green function and the crosses are the t-matrices of the individual scatterers. Implementing the ISA in Eq. (1.41), we find

$$G_{\text{ISA}}(\mathbf{r}, \mathbf{r}') = g(\mathbf{r}, \mathbf{r}') + \iint g(\mathbf{r}, \mathbf{r_1}) \sum_{j=1}^{N} t_j(\mathbf{r_1}, \mathbf{r_2}) G_j(\mathbf{r_2}, \mathbf{r}') d\mathbf{r_1} d\mathbf{r_2}, \tag{1.43}$$

$$= g(\mathbf{r}, \mathbf{r}') + \sum_{j=1}^{N} g(\mathbf{r}, \mathbf{R_j}) t G_j(\mathbf{R_j}, \mathbf{r}'), \tag{1.44}$$

where G_j denotes the ISA Green function of the same system excluding scatterer j, the replacement of G with G_j is a consequence of the fact that we restrict ourselves to the ISA. Repetitive scattering from one scatterer is included in the t-matrix.

Since the aim of this section is to find diffusion of waves, the average over disorder realizations needs to be considered which we denote by angular brackets $\langle \cdot \rangle$. The averaged Green function has to be translationally invariant $\langle G(\mathbf{r}, \mathbf{r}') \rangle \equiv G(\mathbf{r} - \mathbf{r}')$. Moreover for a scattering medium in the thermodynamic limit $G_j(\mathbf{r} - \mathbf{r}') = G(\mathbf{r} - \mathbf{r}')$, which follows from assuming that taking away a single scatterer does not alter the averaged system's behavior significantly. The average of any function is found by integrating the function over space and dividing by the volume V_{tot}, thus for the N scatterer functions the averaging procedure is given by $\int \prod_{j=1}^{N} \frac{d\mathbf{R_j}}{V_{\text{tot}}}$. If this averaging over disorder procedure is applied to element x of the sum in Eq. (1.44) one finds

$$\int g(\mathbf{r}, \mathbf{R_x}) t G_x(\mathbf{R_x}, \mathbf{r}') \prod_{j=1}^{N} \frac{d\mathbf{R_j}}{V_{\text{tot}}} = t \int g(\mathbf{r} - \mathbf{R_x}) \left[\int G_x(\mathbf{R_x}, \mathbf{r}') \prod_{j=1, j \neq x}^{N} \frac{d\mathbf{R_j}}{V_{\text{tot}}} \right] \frac{d\mathbf{R_x}}{V_{\text{tot}}} \tag{1.45}$$

$$= \frac{t}{V_{\text{tot}}} \int g(\mathbf{r} - \mathbf{R_x}) G(\mathbf{R_x} - \mathbf{r}') d\mathbf{R_x}, \tag{1.46}$$

which applied to the whole sum in Eq. (1.44) results in

$$G_{\text{ISA}}(\mathbf{r} - \mathbf{r}') = g(\mathbf{r} - \mathbf{r}') + \sum_{j=1}^{N} \frac{t}{V_{\text{tot}}} \int g(\mathbf{r} - \mathbf{R_j})G(\mathbf{R_j} - \mathbf{r}')d\mathbf{R_j}, \tag{1.47}$$

$$= g(\mathbf{r} - \mathbf{r}') + nt \int g(\mathbf{r} - \mathbf{R_j})G(\mathbf{R_j} - \mathbf{r}')d\mathbf{R_j}, \tag{1.48}$$

where $n = n/V_{\text{tot}}$ is the density of scatterers and all scatterers have identical t-matrices. The remaining integral is a convolution, which suggests this equation is again easier to solve in Fourier space. In real space the solution is approximated by

$$G(\mathbf{r}) = \frac{e^{iK|\mathbf{r}|}}{4\pi|\mathbf{r}|}, \tag{1.49}$$

where the effective complex wave number is given by $K = \sqrt{\omega^2/c^2 + nt} \equiv k_{\text{eff}} + i/(2\ell_s)$ with $k_{\text{eff}} = n_{\text{eff}}\omega/c$ and n_{eff} the effective refractive index.

Equation (1.49) describes how the average wave amplitude propagates through a random medium: it decays exponentially with the scattering mean free path. Yet, the exponential decay does not resemble the result obtained for the concentration in the classical diffusion equation. If we would simply study the intensity by $\langle G \rangle \langle G^* \rangle$ only the intensity which is left in the incident radiation is described. In fact, we have derived Lambert-Beer's law that describes how a coherent beam decays due to scattering.

Intensity propagation

In order to describe diffusion of waves, the averaging needs to be done at the intensity level: after the multiplication of the amplitude with its complex conjugate. To do so, let us return to the iterative Eq. (1.44) obtained in the independent scattering approximation, but instead study $G(\mathbf{r_1}, \mathbf{r_2})G^*(\mathbf{r_3}, \mathbf{r_4})$

$$G(\mathbf{r_1}, \mathbf{r_2})G^*(\mathbf{r_3}, \mathbf{r_4}) = \left[g(\mathbf{r_1}, \mathbf{r_2}) + \sum_{j=1}^{N} g(\mathbf{r_1}, \mathbf{r_j})t_j G_j(\mathbf{r_j}, \mathbf{r_1}) \right] \times$$

$$\left[g^*(\mathbf{r_3}, \mathbf{r_4}) + \sum_{j=1}^{N} g^*(\mathbf{r_3}, \mathbf{r_j})t_j G_j^*(\mathbf{r_j}, \mathbf{r4}) \right]. \tag{1.50}$$

Obviously this equation becomes very complicated due to the multiplication of two sums and the iteration terms. The Feynman diagram visualizes the above equation in a more insightful manner,

$$G(\mathbf{r_1}, \mathbf{r_2})G^*(\mathbf{r_3}, \mathbf{r_4}) = [\; \text{—} \; + \; \text{—×—} \; + \; \text{—×—×—} \; + \ldots] \times$$
$$[\; \text{—} \; + \; \text{—×—} \; + \; \text{—×—×—} \; + \ldots]^*$$

$$\tag{1.51}$$

Here multiplication of an amplitude with a complex conjugate amplitude is symbolized by writing them underneath each other with arrows pointing in opposite directions and

scattering from the same scatterer is indicated by the dotted lines. Note that recurrent scattering has again been ignored. The trick in analyzing the ensemble averaged form of this equation, lies in knowing which diagrams to consider and which ones to neglect. For example, ensemble averaging over all diagrams in which the amplitude and complex amplitude do not share any scatterer results in the coherent propagation of waves as already found in the amplitude section. The second simplest diagrams to analyze are those that have one or more scatterers in common in a sequential manner, the so-called ladder terms. If we let a triple line denote the ensemble averaged dressed Green function we obtain[5]

$$\langle L(\mathbf{r_1}, \mathbf{r_2}) L^*(\mathbf{r_3}, \mathbf{r_4}) \rangle = \quad \cdots \quad + \quad \cdots \quad + \quad \cdots \quad + \ldots \tag{1.52}$$

$$= \quad \boxed{\mathcal{L}} \quad , \tag{1.53}$$

with

$$\boxed{\mathcal{L}} \equiv \quad \vdots \quad + \quad \cdots \quad + \quad \cdots \quad + \ldots \tag{1.54}$$

$$= \quad \vdots \quad + \quad \boxed{\mathcal{L}} \quad . \tag{1.55}$$

In real space the Bethe-Salpeter like expression for this ladder vertex reads

$$\mathcal{L}(\mathbf{r}) = ntt^* \delta(\mathbf{r}) + ntt^* \int \frac{e^{-\mathbf{r}'/\ell_s}}{(4\pi |\mathbf{r}'|)^2} \mathcal{L}(\mathbf{r} - \mathbf{r}') d\mathbf{r}'. \tag{1.56}$$

Here for the dressed Green function Eq. (1.49) was used. Conservation of energy allows us to find a relation between the scattering cross section and the t-matrix of an individual scatterer: $ntt^* = 4\pi/\ell_s$. With help from this relation and by transforming to Fourier space, one finally obtains

$$\mathcal{L}(\mathbf{r}) = \frac{4\pi}{\ell_s} \delta(\mathbf{r}) + \frac{3}{\ell_s^3 |\mathbf{r}|}. \tag{1.57}$$

The second term in this equation describes how the intensity drops off in a multiple scattering environment. If we want to know the intensity $\langle I \rangle$ measured at point $\mathbf{r}$ originating from a unit source at $\mathbf{r_s}$, the ladder diagram needs to get connected by dressed Green functions to the source and the observation point [51]

$$\langle I(\mathbf{r}) \rangle = \quad \boxed{\mathcal{L}} \quad . \tag{1.58}$$

---

[5]Technically the ensemble averaged Green functions given by the triple lines do not contain all scatterers, because any ensemble average would then lead to a completely connected diagram. For a large number of scatterers however we can ignore this technicality and treat all dressed Green functions equally and independently.

26

(a) (b)
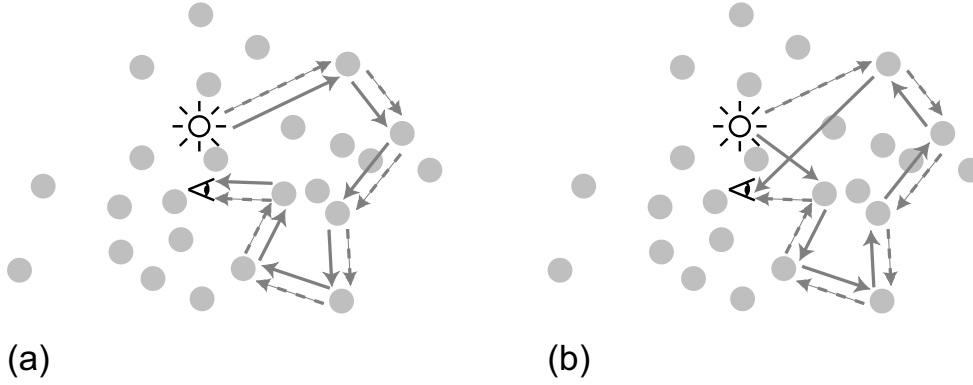
Figure 1.8: Two-dimensional representation of (a) a ladder term and (b) a most crossed term connected to both a source and an observation point. Straight arrows: dressed Green functions. Dashed arrows: complex conjugate Green functions. Ensemble averaged ladder terms give rise to diffusion. Ensemble averaged cross-terms are responsible for interference effects. Intuitively this interference can be understood by realizing that when the source and the observation point overlap the path length difference between the regular path and the complex conjugate path becomes zero. Therefore, the two paths interfere constructively at the source position.

Where we have introduced $\lhd$ to denote the observation point and $\circledast$ to denote the source. Defining $r = |\mathbf{r_1} - \mathbf{r_s}|$, the two short-range vertices connecting the ladder diagram to the source and the observation point are given by

$$\int G(\mathbf{r_1} - \mathbf{r_s})G^*(\mathbf{r_1} - \mathbf{r_s})d\mathbf{r_1} = \frac{4\pi}{16\pi^2}\int e^{-r/\ell_s}dr = \frac{\ell_s}{4\pi}. \tag{1.59}$$

By treating these short-range vertices as points and thereby letting the ladder term run from the source to the observation point, diagram (1.58) simplifies from an integral to a straightforward multiplication

$$\langle I(\mathbf{r}) \rangle = \left(\frac{\ell_s}{4\pi}\right)^2 \mathcal{L}(\mathbf{r} - \mathbf{r_s}) = \frac{3}{16\pi^2\ell_s|\mathbf{r} - \mathbf{r_s}|}. \tag{1.60}$$

Thus the ensemble averaged intensity's $\mathbf{r}$ dependence is analogous to the stationary solution of the classical diffusion equation. We conclude that the ladder vertex is responsible for the diffusion of waves. In hindsight this should not come as too big of a surprise: ladder terms represent random walks of intensity through a random medium as illustrated in Fig. 1.8(a). By ensemble averaging these random walks one describes diffusion, just as in the particle case. Solution of the time-dependent Bethe-Salpeter like Eq. (1.56) enables us to find an expression for the diffusion constant in a random medium: $D = \frac{1}{3}v_e\ell$ with v_e the energy velocity [52].

1.2.5 Anderson localization

In the previous section, we have deliberately limited our discussion to those diagrams that give rise to diffusion of light, namely the ladder terms. Other diagrams are of course also present in reality and they give rise to other phenomena. Among the most studied diagrams are the so-called "most-crossed" diagrams. In these diagrams, the shared scatterers between the amplitude and complex conjugate amplitude are encountered in a time-reversed manner as shown in Fig. 1.8(b). The intensity at the observation point now becomes strongly

dependent on its relative position to the source. If the source and the observation point overlap, the amplitude and the complex amplitude following the most crossed paths always interfere constructively and thereby lead to an enhanced intensity at this particular position. By a similar reasoning the most crossed diagrams lead to an enhanced intensity in the exact backscattering direction when illuminating a finite multiple scattering sample. This interference effect is known as enhanced backscattering (EBS) or weak localization, and has been observed for a wide variety of waves [53–56]. Over the years EBS has grown from an intriguing interference effect into a technique that enables the characterization of multiple scattering samples [57–60]. In particular because the width of the EBS cone is inversely proportional to the transport mean free path.

In lower dimensions ($d = 1, 2$), random walks have unit probability of returning to the point of origin. Therefore, interference cannot be ignored when describing the transport of waves in one-or two-dimensional media. Rather than showing a diffuse behavior, the waves are exponentially localized around the source position. The absence of diffusion due to interference is known as Anderson localization, named after the man who theoretically discovered it for electron waves in 1958 [61]. In three dimensions, the situation is more complex [62]. For weakly scattering media diffusion remains a valid approximation: the probability of a wave returning to its initial position is negligible. With an increase in scattering strength, however, interference effects become more important. When the scattering mean free path is of similar magnitude as the wavelength of radiation ($k\ell_s \sim 1$ [63]), the waves scatter so strongly near the source position that interference cannot be ignored[6]. The diffusion of waves is brought to a complete standstill and the diffusion constant becomes zero.

Observing Anderson localization in three dimensions with classical waves is extremely challenging [64]. Partly because the potential in Helmholtz Eq. (1.31) depends quadratically on frequency, in contrast to the potential for de Broglie waves that is frequency independent [11, 65]. Increasing the wavelength in a system thus does not automatically lead to a smaller value for $k\ell_s$ and a significant effort needs to be put in designing strongly scattering samples for a particular frequency range [65]. Experiments with light have additionally been hindered by the presence of absorption, which makes it difficult to make unambiguous claims on the absence of diffusion [66–68]. Recent experiments with ultrasound and metallic beads have led to convincing results that do show signatures of Anderson localization in three dimensions [69]. Together with an experiment that visualized the localized electronic states with a scanning tunneling microscope, this experiment made it possible to study the fascinating spatial structure of localized wave functions [70, 71].

1.3 Interaction between sources and random media

Multiple scattering of radiation and the science of light generation have traditionally been studied on their own. The effect of scattering on the propagation of waves generated from a far away source, is what primarily interested the astrophysicists who initiated the field of multiple scattering of light [13, 28]. For that purpose, it suffices to assume that the incident radiation is a plane wave which also conveniently simplifies the underlying mathematics. Parallel to the efforts of understanding multiple scattering, a very successful combination of science, engineering, and business has led to an incredible development in man-made

---

[6]Fulfilling the criterion $k\ell_s \sim 1$ is by no means a guarantee for having localization effects in a sample. It should rather be seen as a quantity that indicates when localization effects are *expected* to become important.

Figure 1.9: Illustration of a random laser. Radiation (light gray arrows) originating from a spontaneous emission event (white disks) is amplified through stimulated emission by the excited gain medium (gray area). Scatterers (dark gray disks) provide feedback to the light by lengthening the path length traveled through the gain medium. The light generated by a random laser is omnidirectional, but spectrally narrow compared to the spontaneous emission spectrum.

sources of light over the past two centuries [72, 73]. First, by the introduction of electric light sources at the end of the nineteenth century, and second by the continuous innovations in the field of laser physics starting from the second half of the twentieth century. In this section, we discuss how sources *embedded* in multiple scattering media can give rise to exciting new phenomena. We introduce the concept of a random laser in Subsec. 1.3.1 and show how a source can give rise to infinite range correlations in Sec. 1.3.2.

1.3.1 Random lasers

Whereas in a conventional laser mirrors are used as a feedback mechanism, a random laser uses multiple scattering of light as a feedback mechanism. A cartoon of a random laser is shown in Fig. 1.9. In a random laser, a spontaneously emitted photon gets amplified by stimulated emission while at the same time its path length in the gain medium is lengthened due to the feedback provided by multiple scattering. As a consequence the emission spectrum narrows for increasing pump powers and the output power for the peak of the spectrum shows typical threshold behavior. In contrast to a conventional laser the emitted light from a random laser is omnidirectional.

The idea of generating light inside a scattering medium by stimulated emission was already thought of in 1968 by the Soviet scientist Letokhov [74]. After some initial experiments on ground laser crystals [75, 76], the field really started in the mid 1990's due to a dispute on a paper by Lawandy *et al.* describing laser action from supposedly strongly scattering samples [77, 78]. The dispute centered around the question whether the samples were truly in the diffusive multiple scattering regime or whether the samples were just redirecting some amplified light by single scattering. The *Nature* editor dealing with the scientific correspondence, coined the term "random laser" which has been in use ever since. A random laser can either be conceived as a multiple scattering medium with gain or as a laser system with a complex cavity configuration. In fact, both well-known laser physics effects are observed with random lasers, *e.g.*, relaxation oscillations [79], intensity fluctuations [80], and mode coupling [81], as well as prominent multiple scattering phenomena, *e.g.*, enhanced backscattering [82] and speckle [83].

In pioneering experimental studies by Cao *et al.* [84, 85], narrow features were detected

in the output spectrum of ZnO random lasers. The interpretation of these narrow spectral features has turned out to be far from straightforward and the community has not yet converged to a particular explanation. Impressive theoretical efforts [86, 87] have mainly focussed on two-dimensional random laser systems. Yet, it remains to be seen how these theoretical concepts translate to three dimensional systems and how these theories can be connected directly to experimentally relevant parameters. Anderson localization [85], Fabry-Pérot resonances [88, 89], absorption induced confinement [90], and photons traveling exceptionally long light paths through the gain medium [91], are all examples of explanations put forward that illustrate the plethora of interpretations to be found in the literature. Terminology such as "coherent random lasing" and "non-resonant feedback" has become widespread [92], but often conceals the underlying physics [93]. We therefore prefer to refrain from using this kind of terminology in this thesis.

1.3.2 C_0-correlation

Irregular intensity patterns that appear when coherent radiation is scrambled by a static random medium, display all kinds of intensity correlations [48]. The fact that these correlations arise indicate that the speckle patterns caused by constructive and destructive interference are not as random as we might initially think. The best-studied and easiest to observe correlation, the C_1 also known as the "memory-effect", describes how speckle patterns are correlated under rotation of the sample when both illumination and detection are limited to a single k-vector (this configuration is typically referred to as "one channel in, one channel out"). This correlation is short-ranged, meaning that it decays exponentially with rotation angle. The two other well-known correlations, the C_2 and C_3 [94, 95], describe long-range and infinite range correlations respectively. The C_2 shows that the total transmitted intensity is also correlated to the k-vector of the incident radiation ("one channel in, all channels out") or vice versa. The C_3 is the optical analog of universal conductance fluctuations and describes how much the total transmitted intensity fluctuates when radiation is incident under all possible angles ("all channels in, all channels out").

Since the study of intensity correlations was largely initiated by scientists working in the field of condensed matter physics, it is not surprising that all these three correlation refer to samples analyzed in a transmission configuration. In contrast to electromagnetic radiation, electrons cannot be created out of nothing inside a sample. In 1999, B. Shapiro [51] calculated a new type of correlation by considering intensity generated from *within* random media. He considered two diffusive intensities originating from the same unit source at $\mathbf{R_s}$ propagating to $\mathbf{r}$ and $\mathbf{r} + \Delta\mathbf{r}$ that share one scatterer in close proximity to the source. Diagrammatically the correlated intensity product is given by

$$\langle I_c(\mathbf{r})I_c(\mathbf{r} + \Delta\mathbf{r})\rangle = \qquad\qquad\qquad\qquad\qquad\qquad (1.61)$$

This diagram is evaluated by first isolating and calculating the short-range vertex U, so that afterwards the diffusion ladders can be treated as if emerging from the source position.

The vertex U reads

$$U = \qquad\qquad\qquad\qquad\qquad\qquad\qquad\qquad (1.62)$$

If we let $\mathbf{R_x}$ denote the position of the shared scatterer and $\mathbf{r_1}$ and $\mathbf{r_2}$ denote the connection points to the ladder, the number U is given by

$$U = \frac{4\pi}{\ell} \iiint G(\mathbf{r_1} - \mathbf{R_s})G^*(\mathbf{r_1} - \mathbf{R_x})G^*(\mathbf{R_x} - \mathbf{R_s})$$
$$\times G(\mathbf{r_2} - \mathbf{R_x})G(\mathbf{R_x} - \mathbf{R_s})G^*(\mathbf{r_2} - \mathbf{R_s})d\mathbf{R_x}d\mathbf{r_1}d\mathbf{r_2}, \qquad (1.63)$$

where the factor $4\pi/\ell$ originates from the shared scatterer at $\mathbf{R_x}$. The integrations over $\mathbf{r_1}$ and $\mathbf{r_2}$ are similar and most easily handled in Fourier-space. These two integrations return $\frac{\ell}{4\pi}\frac{\sin k_0 r}{k_0 r}\exp\left(-\frac{r}{2\ell}\right)$, with $r = |\mathbf{R_s} - \mathbf{R_x}|$. Inserting these expressions in integral Eq. (1.63) gives

$$U = \frac{4\pi}{\ell}\frac{\ell^2}{16\pi^2}\int G^*(\mathbf{R_x} - \mathbf{R_s})G(\mathbf{R_x} - \mathbf{R_s})e^{-r/\ell}\left(\frac{\sin k_0 r}{k_0 r}\right)^2 d\mathbf{R_x} \qquad (1.64)$$

$$= \frac{\ell}{4\pi}\int \frac{e^{-r/\ell}}{(4\pi r)^2}e^{-r/\ell}\left(\frac{\sin k_0 r}{k_0 r}\right)^2 d\mathbf{R_x} \qquad (1.65)$$

$$= \frac{\ell}{32\pi}. \qquad (1.66)$$

In the last step we have approximated $\exp(-r/\ell)$ by 1, since the integrand is dominated by the region $r \ll \ell$. Using this number for the vertex U, expression (1.59) for the short-range objects connecting the ladders to the observation points, and the fact that an equivalent C_0 diagram can also be obtained by placing the shared scatterer in the outer Green functions of the diagram, the contribution of diagram (1.61) to the intensity correlation becomes

$$C_0(\Delta r) = \frac{\langle I_c(\mathbf{r})I_c(\mathbf{r} + \Delta\mathbf{r})\rangle}{\langle I(\mathbf{r})\rangle\langle I(\mathbf{r} + \Delta\mathbf{r})\rangle} \qquad (1.67)$$

$$= 2\frac{\ell}{32\pi k_0}\mathcal{L}(\mathbf{r} - \mathbf{R_s})\mathcal{L}(\mathbf{r} + \Delta\mathbf{r} - \mathbf{R_s})\left(\frac{\ell}{4\pi}\right)^2 \Bigg/ \mathcal{L}(\mathbf{r} - \mathbf{R_s})\mathcal{L}(\mathbf{r} + \Delta\mathbf{r} - \mathbf{R_s})\left(\frac{\ell}{4\pi}\right)^4$$
$$\qquad (1.68)$$

$$= \frac{\pi}{k_0\ell}. \qquad (1.69)$$

From which we conclude that scattering close to the source induces a correlation with infinite range. Such a type of correlation means that for some realizations of disorder the speckle pattern *as a whole* has a higher or lower intensity than the average intensity as illustrated in Fig. 1.10. This result might come as a surprise since for all configurations of disorder the intensity originates from the same source. Apparently, random media change the output power of the source.
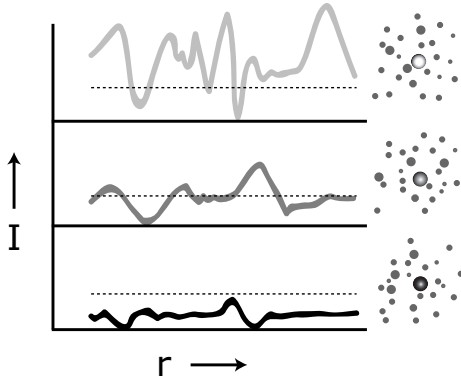
Figure 1.10: The C_0-correlation is an infinite range intensity correlation caused by a scatterer placed in close proximity to a unit source. In this figure the effect of C_0 on three speckle patterns is illustrated. Rather than fluctuating around the ensemble average (dashed lines), the averages of the individual speckle patterns for different realizations of disorder show an offset (black, gray, and light gray lines).

1.4 Outline of this thesis

In *chapter 2*, we argue how different types of molecular light sources can lead to surprisingly different outcomes of experiments in photonics. Random lasers are shown to be great model systems for studying the consequences of using different types of sources experimentally. A new classification scheme for sources is introduced in close analogy to the source classification in electronics. The implications of this classification for the C_0-correlation are discussed and illustrated with a transfer matrix calculation of a source inside a one-dimensional random stack of layers with alternating refractive indices.

By extruding such a one-dimensional system along one direction, the dynamics of Anderson localization can be studied. In *chapter 3*, we explain how this so-called transverse localization scheme maps a spatial coordinate onto time. Using a microwave setup, we are able to measure when the ensemble averaged wave functions localize. An eigenmode analysis of the system's Hamiltonian is performed, in order to explain the results.

In *chapter 4*, diffusion inside an amplifying random medium is studied. By making use of a side-imaging technique, the random lasing threshold becomes visual in space. The system is analyzed numerically by coupling the time-dependent diffusion equation to the time-dependent equation for the population inversion. Both experimentally and numerically, we observe that gain leads to an expansion of the diffusive volume.

This expansion in volume can cause remarkable spectral effects in a random laser as illustrated by experimental studies in *chapter 5*. By carefully controlling the absorption of light emitted by a random laser, we are able to shift the output spectrum of a random laser by several line widths. This tunability is analyzed by describing the random laser emission spectrum with one effective cavity decay rate.

The narrow spectral features that have dominated the field of random laser are studied in *chapter 6*. We introduce new ways of studying these features systematically. First, the spatial structure belonging to a certain spectral feature is measured using a spectrally and spatially selective detection apparatus. Second, a wide range of random laser samples is studied to find out how the transport mean free path and the gain length influence the appearance of spikes. A conceptual model is introduced based on two laser modes that explains the results qualitatively.

Finally, in *chapter 7* we conclude and put forward several subjects and applications naturally following from our research.

Classification of light sources and their interaction with active and passive environments

The central theme of this chapter is the dependence of a light source on its optical surroundings. Four-level light sources are classified in two types and this classification is used to describe their responses to both changes in the LDOS and stimulated emission. Random lasers are shown to be particulary illustrative in showing how different sources can lead to different experimental outcomes in photonics. By analyzing the random lasers with an extended set of rate equations, properties of the used sources are retrieved. Our results require a revision of studies on sources in complex media and put the C_0-correlation in a different perspective. An example of such a revision is given by a numerical calculation of a source in a 1D stack of layers with alternating refractive indices.

2.1   Light sources in the natural sciences

Atomic and molecular light sources are essential tools in the natural sciences. Physicists use these light sources in a great variety of situations, for example to study light-matter interactions in the context of cavity quantum electrodynamics [33, 96], to probe vacuum fluctuations inside and around photonic and plasmonic nanostructures [97, 98], or as building blocks for lasers [86]. In the life sciences, fluorescent proteins have quickly become one of the most important workhorses soon after their discovery [99]. Major engineering efforts are nowadays devoted to inventing light-source based microscopy techniques, in order to obtain improved resolution and sensitivity [100, 101].

The prominence of light sources in scientific experiments solicits for a well-defined classification of different types of sources. We propose such a classification analogous to the field of electronics where every circuit design incorporates a well defined source. In electronics, ideal sources are classified as Constant Current Sources (CCS) or Constant Voltage Sources (CVS) depending on their response to a certain load [102].
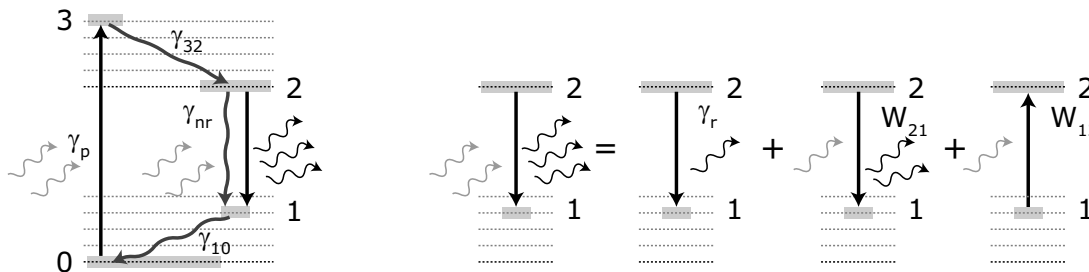
Figure 2.1: (left) Radiative and non-radiative transitions in a four level system. Straight black arrows: radiative transitions. Dark gray wiggly arrows: non-radiative transitions. Light gray wiggly arrows: incident radiation. Black wiggly arrows: output radiation. Gray bars: population level. (right) The photon production rate from level 2 to level 1 is determined by the cumulative processes of spontaneous emission, stimulated emission, and stimulated absorption.

Mathematically, a point source (sink) is incorporated by a positive (negative) divergence ($S = \nabla \cdot \mathbf{J}$) of a certain vector quantity in space. In order to be classified as a source for light, light should either be created by conversion from a different type of energy, *e.g.*, by electroluminescence, or by a photochemical process in which the absorbed excitation photon differs in frequency from the emitted photon, *e.g.*, in three- and four-level systems. In contrast, ideal two-level systems cannot be considered as light sources, they are scatterers instead. In this chapter, we limit ourselves to a discussion of four-level systems. Our approach is general however and can also be applied to other light generation mechanisms.

In a four-level system there are two decay channels from the lowest vibrational sublevel of the excited state to a vibrational sublevel of the ground state: a radiative and a nonradiative channel. These two relaxation mechanisms are competing for the number of molecules in the excited state, in a similar way as two parallel resistances are competing for current in a simple electronic CVS circuit. As discussed in Sec. 1.1.3, the quantum efficiency ϕ of the molecule describes the ratio between the radiative and total decay rate. The quantum efficiency is therefore an essential parameter in describing the response of light sources.

For a collection of emitters, four rate equations describe the population of the different energy levels. These levels are illustrated in Fig. 2.1. Molecules are excited from the ground state (level 0) to the excited state (level 3) with pump rate γ_p. Rapid nonradiative transitions let molecules decay from this excited state to the lowest vibrational sublevel of the excited state (level 2). Molecules can then decay either radiatively by spontaneous or stimulated emission with rate γ_r and W_{21} respectively, or nonradiatively with rate γ_{nr} to a vibrational sublevel of the ground state (level 1)[1]. These sublevels either depopulate nonradiatively to the ground state with rate γ_{10} or radiatively by stimulated absorption to level 2 with rate W_{12}. The radiative transitions from level 2 to level 1 constitute our light

---

[1]The stimulated transitions between level 1 and 2 are assumed to be due to an applied electromagnetic field. The radiated photons by the molecules of course contribute to this field, but these contributions are neglected in the current discussion. They do of course play a significant role in lasers as will be shown in the next section. The values for W_{21} and W_{12} are determined by the Einstein B coefficient and the spectral electromagnetic energy density ρ_ω by $W_{12} = W_{21} = B\rho_\omega$ [16].

source. The rate equations[2] for the four levels read

$$\frac{dN_0}{dt} = -\gamma_p N_0 + \gamma_{10} N_1 \tag{2.1}$$

$$\frac{dN_3}{dt} = \gamma_p N_0 - \gamma_{32} N_3, \tag{2.2}$$

$$\frac{dN_2}{dt} = \gamma_{32} N_3 - (\gamma_r + W_{21} + \gamma_{\text{nr}}) N_2 + W_{12} N_1, \tag{2.3}$$

$$\frac{dN_1}{dt} = (\gamma_r + W_{21} + \gamma_{\text{nr}}) N_2 - (\gamma_{10} + W_{12}) N_1. \tag{2.4}$$

We are now particularly interested in finding the stationary rate of photon production, $(\gamma_r + W_{21})N_2$, expressed in terms of the pump rate and the radiative and non-radiative decay rates. Putting $(\gamma_{10} + W_{12})N_1 = (\gamma_r + W_{21} + \gamma_{\text{nr}})N_2$ obtained from Eq. (2.4) in Eq. (2.1) gives

$$N_2 = N_0 \frac{\gamma_{10} + W_{12}}{\gamma_{10}} \frac{\gamma_p}{\gamma_r + W_{21} + \gamma_{\text{nr}}}, \tag{2.5}$$

and hence for the net photon production rate Γ_{ph}

$$\Gamma_{\text{ph}} = (\gamma_r + W_{21})N_2 - W_{12}N_1 = \left(\frac{\gamma_{10} + W_{12}}{\gamma_{10}} \frac{\gamma_r + W_{21}}{\gamma_r + W_{21} + \gamma_{\text{nr}}} \gamma_p - \frac{W_{12}}{\gamma_{10}} \gamma_p \right) N_0, \tag{2.6}$$

$$\approx \left(\frac{\gamma_r + W_{21}}{\gamma_r + W_{21} + \gamma_{\text{nr}}} \right) \Gamma_e \tag{2.7}$$

In the second step, a moderate pump rate is assumed such that the system is far away from saturation. In that case the depopulation of the ground level N_0 is negligible and the factor $\Gamma_e \equiv \gamma_p N_0$ is taken as the effective excitation rate. In addition, fast non-radiative relaxations are assumed to dominate over stimulated absorption in level 1: $\gamma_{10} \gg W_{12}$.

Based on Eq. (2.7), we are able to distinguish two classes of light sources. The rate of radiative decay can be enhanced by an increased rate of spontaneous or stimulated emission, where changing the spontaneous emission rate comes down to manipulating the LDOS at the source position. However, Eq. (2.7) shows that in the absence of a nonradiative decay channel the output power is independent on the rates of radiative decay. Every photon that comes in, comes out. An unsaturated unity quantum efficiency source is thus a Constant Power Source (CPS). On the other hand, for sources with a large non-radiative decay channel, the number of transitions is conserved, but the power emitted by the source is dependent on the rates of the radiative decay channel. These sources are named Constant Amplitude Sources (CAS) which stems from a Green function analysis discussed in Sec. 2.4.

In this chapter, the influence of light source typology on the generation of light in complex media is studied. We provide a clear demonstration of the relevance of our classification with new random laser experiments, where different kinds of light sources act as different gain media. The experimental methods and results are described in Sec. 2.2. In Sec. 2.3, a model is developed to analyze the sources used in experiment. Besides these new experimental results, we show in Sec. 2.4 how the output power of a classical dipole source, a CAS

---

[2]The population can either be described in terms of densities or in terms of total number of molecules, since in the latter the volume of the system can be divided out.
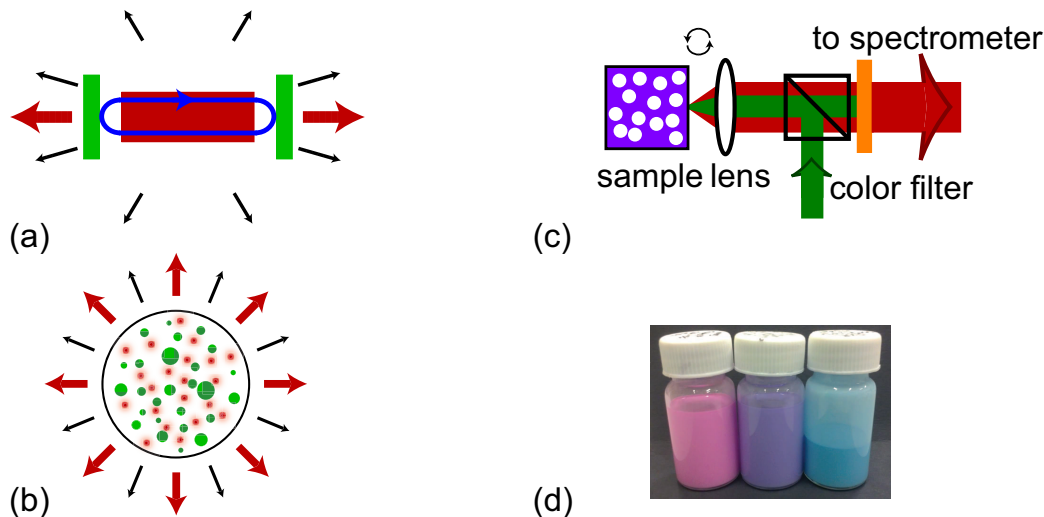
Figure 2.2: Illustration of emission directionality below threshold (black arrows) and above threshold (red arrows) in (a) a conventional laser and (b) a random laser. In a random laser the emitted light by an ensemble of sources is always omnidirectional. (c) Experimental apparatus for random laser experiment. Pump light (green arrow) generated by an OPO is focussed onto the sample by a lens. The fluorescent light (red arrow)is filtered from the pump light and analyzed by a grating spectrometer. (d) The three suspensions used as samples in the experiment. From left to right: Rhodamine 640 P, Cresyl Violet, and Nile Blue. All samples contain 1% titania particles in volume.

by definition, is dependent on its environment by performing a Green function analysis of a single scatterer and a source. This calculation allows for discussing the impact of CPS and CAS in studies on light sources and passive multiple scattering media and an expression for a CPS is given. Using a transfer matrix calculation, the intensity profile inside a 1D localizing sample is analyzed in Sec. 2.5. The type of source used in the computation turns out to be crucial in order for the ensemble averaged data to converge.

2.2 Random laser experiment

In a random laser [93] the role of sources is twofold: first, they are seeds of spontaneous light emission; second, they amplify light by stimulated emission of radiation. Due to the multiple-scattering feedback mechanism, random lasers form a unique laser system. In contrast to conventional lasers, they have a statistically isotropic mode selectivity as illustrated by the cartoons in Fig. 2.2(a) and (b). The mode selection is solely determined by the spectral shape of the gain curve. In a random laser, measuring the emitted energy into a large enough solid angle corresponds to measuring the total emitted intensity: it is as if diffusion mimics an integrating sphere. In our experiments, we utilize this much neglected property of random lasers to study the energy emitted by light sources with different quantum efficiencies for varying pump rates.

Samples

Three molecular light sources were studied in a random laser configuration by suspending titania particles (R900 DuPont, volume fraction 1%, $\ell \approx 5$ µm) into three different 1 mM solutions of organic dyes in methanol. The three dye solutions acted as gain media and were chosen based on their quantum yields (ϕ) reported in literature [15, 103–105]: Rhodamine
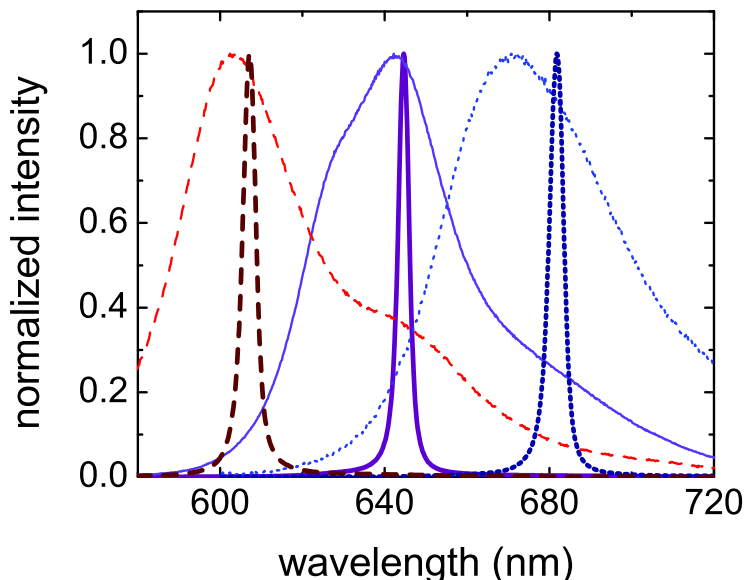
Figure 2.3: Normalized experimental emission spectra below and narrowed spectra above random laser threshold for three different light sources: Rhodamine 640 P (red dashed lines), Cresyl Violet (purple solid lines), and Nile Blue (blue dotted lines). The β-factor is determined by the quotient of the area of the normalized spectra above and below threshold.

640 P ($\phi = 1$), Cresyl Violet ($\phi = 0.54$), and Nile Blue ($\phi = 0.27$). A photograph of the samples is shown in Fig 2.2(d). Experiments with Rose Bengale samples ($\phi = 0.11$ [106]) were also explored, but these samples turned out unsuitable since the random laser threshold could not be reached. To prevent aggregation and sedimentation of titania particles all samples were treated in an ultrasonic bath before and spinned during measurement, and a small amount of $CaCl_2$ (0.06 g/L) was added to the Nile Blue sample. Experiments were then performed within 30 min. after preparation of the sample, in order to make sure that sedimentation effects were negligible. In fact, at these dye and titania concentrations, we did not measure changes in the diffusive profile of the random laser for over 2 hours. Quartz cuvettes were used as experimental cells (Hellma, inner dimensions 10×10×45 mm, wall thickness 1.25 mm). After experiment, the samples were inspected by eye to ensure the high pump powers did not damage the cuvettes.

Optical measurement scheme

The experimental apparatus is schematically shown in Fig 2.2(c). Excitation light generated by an optical parametric oscillator (Opolette, 20 Hz, 5 ns) was focussed onto the samples by an aspherical lens (F/#=1.5). The same lens collected the emission which was then spectrally analyzed using a spectrograph (Oriel MS-257) connected to an EMCCD camera (Hamamatsu, C-9100). The power of the pump beam was measured with an Ophir power meter (PD300-3W). By placing calibrated neutral density filters in between the sensor and the beam, it was ensured that the power meter did not saturate. The pump wavelength was set at 535 nm for the Rhodamine and the Cresyl Violet sample, and at 563 nm for the Nile Blue sample.
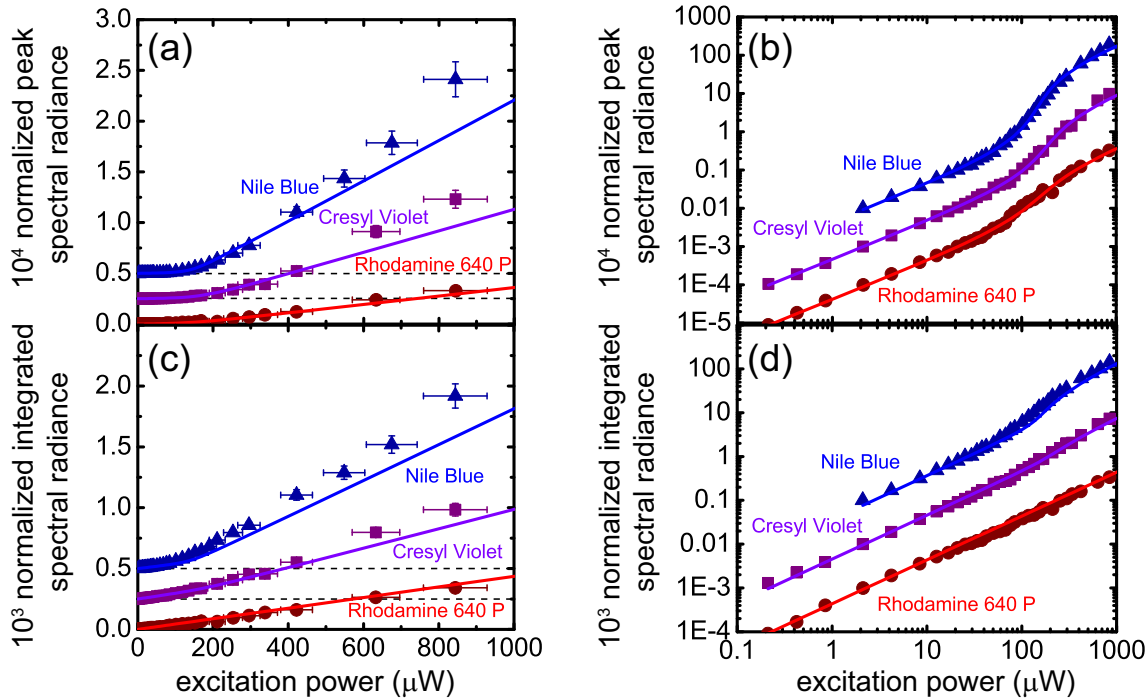
Figure 2.4: Input-output diagrams for random lasers consisting of light sources with low and high quantum efficiencies. (a)-(b) peak spectral radiance versus pump power for three random lasers with different molecular light sources on (a) a linear and (b) a log-log scale. The solid lines are fits to the experimental data. (c)-(d) integrated spectral radiance versus pump power for three random lasers on (c) a linear and (d) a log-log scale. The solid lines are theoretical calculations. The Rhodamine 640 P random laser does not show a clear threshold. All data points in (a)-(d) were normalized to the values at 2.1 μW and the results for the Nile Blue and Cresyl Violet random lasers were shifted vertically for clarity.

Results

For all random laser samples, the fluorescent emission spectra were recorded for different values of the pump fluence below and above threshold. In Fig. 2.2(c) normalized emission spectra far below and far above threshold are plotted. The spectra above threshold are narrower by a factor ∼ 10 compared to the spectra below threshold and the peaks are slightly red shifted due to reabsorption. In this chapter this reabsorption effect is of minor importance, but we will revisit this effect in *chapter 5* and show how reabsorption can lead to spectrally tunable random lasers.

Figure 2.4 shows (a)-(b) the peak and (c)-(d) the integrated spectral radiance versus the excitation power. To compare the threshold behavior of the three random lasers, the intensities were normalized to the value at 2.1 μW. The normalization constants for the peak spectral radiance were 47, 105, 291 counts/s for Nile Blue, Cresyl Violet, and Rhodamine respectively. As expected the highest quantum efficiency gain medium thus returns the highest absolute output power below threshold. We note though that differences in absolute output power are also caused by varying absorption cross sections. The peak spectral radiance shows a clear threshold for all the three random laser systems around 100 μW. After crossing the threshold, the spectral peak values become comparable and are all on the order of $1 \cdot 10^6$ counts/s at a pump power of 840 μW. The increase in absolute peak spectral radiance is thus higher for the Nile Blue and Cresyl Violet random lasers compared to the

Rhodamine random laser. As a consequence the threshold of these low quantum efficiency lasers is more pronounced in Fig. 2.4(a) and (b).

In a conventional laser angular redistribution of light emission causes a threshold in the spectrally integrated power of the output beam irrespective of the chosen gain medium. However, in the experimental results shown in Fig. 2.4(c)-(d) we observe that for the random laser with the highest quantum efficiency gain medium (Rhodamine) such a threshold in the integrated spectral radiance is absent. The integrated spectral radiance increases linearly for all excitation powers. The random lasers made of lower quantum efficiency sources do show a threshold in the total output power versus input power graph.

2.3   Random laser model

Standard lasers are described with rate equations [15] describing the number of photons in the cavity mode, $q(t)$, and the number of molecules in the upper laser level, $N(t)$. For a four-level system it is usually assumed that only the population of the ground state and the upper-laser level are significant. This assumption significantly simplifies the population rate equations of Sec. 2.1. In a conventional laser, the cavity mode and its cavity decay time are well-defined. In contrast, the number of modes that contribute to lasing in a diffusive random laser is very high (typically on the order of a few thousand). All these modes have different center frequencies and different cavity decay times. In our random laser model, the lasing modes are lumped together into a single "mode" with an effective cavity decay rate. Furthermore, to monitor the total output energy of the random laser, we extend the laser rate equations with an equation describing the number of photons, $w(t)$, emitted outside the lasing mode

$$\frac{dq}{dt} = -q\gamma_c + \beta\gamma_r Nq + \beta\gamma_r N, \tag{2.8}$$

$$\frac{dw}{dt} = -w\gamma_c + (1 - \beta)\gamma_r N, \tag{2.9}$$

$$\frac{dN}{dt} = R - N\gamma_{\text{tot}} - \beta\gamma_r Nq. \tag{2.10}$$

Here, R is the pump photon rate, γ_c is the effective cavity decay rate and γ_{tot} is the total decay rate with $\gamma_{\text{tot}} = \gamma_r + \gamma_{\text{nr}}$ where γ_r and γ_{nr} are the radiative and nonradiative decay rates respectively.

As discussed in Sec. 1.1.5, the spontaneous emission factor β describes what fraction of spontaneous emission events contributes to lasing [107]. Due to the absence of angular mode selection in a diffusive random laser, the β-factor of the effective laser "mode" reduces to describing what part of the spectrum contributes to the laser light. The above threshold spectrum thus suffices for distinguishing photons inside and outside the lasing mode: for photons emitted in the wings of the spectrum stimulated emission is neglected in rate Eq. (2.9), whereas for photons emitted into the peak of the spectrum, Eq. (2.8), stimulated emission is added to the spontaneous emission rate. The random lasers considered here have a smooth spectrum above threshold and are well in the diffusive regime: $\ell \ll L$ where L is the characteristic system length. The particular cases of random lasers outside the diffusive regime or with narrow spectral features [85] require different formulations [86], which we discuss in more detail in *chapter 6*. In short, these type of random lasers do not have an isotropic mode selectivity and the β-factor ceases to be only spectrally dependent. We determine the β-factor for the three random lasers by calculating the ratio of the integrated

spectra above and below threshold after normalizing to the peak value [107]: for Rhodamine $\beta = 0.099$, for Cresyl Violet $\beta = 0.088$, and for Nile Blue $\beta = 0.076^3$.

To infer the threshold, the steady-state solutions to Eqs. (2.8)-(2.10) for the number of photons in the peak and the wings of the spectrum are calculated

$$q = -\frac{1}{2\beta\phi} + \frac{R}{2\gamma_c} + \frac{1}{2}\sqrt{\left(\frac{1}{\beta\phi} - \frac{R}{\gamma_c}\right)^2 + 4\frac{R}{\gamma_c}}, \tag{2.11}$$

$$w = \left(\frac{R}{\gamma_c} - q\right)\frac{1-\beta}{\phi^{-1}-\beta}. \tag{2.12}$$

Above threshold the slope of the solution for q changes and the β-factor and ϕ determine the "smoothness" of the transition. Far below and far above threshold, q and $q+w$ depend linearly on R. Analytical expressions for the threshold for the peak and integrated spectral radiance are obtained by extrapolating the linear expressions for the far above threshold number of photons to $q = 0$ and $q + w = 0$:

$$R_{\text{th}}^{\text{peak}} = \left[(\beta\phi)^{-1} - 1\right]\gamma_c, \tag{2.13}$$

$$R_{\text{th}}^{\text{int}} = \left[(\beta\phi)^{-1} - \beta^{-1}\right]\gamma_c. \tag{2.14}$$

Thus, it is wrong practice to use $R_{\text{th}}^{\text{int}}$ to find the threshold of a random laser, because $R_{\text{th}}^{\text{int}} \to 0$ when $\phi \to 1$. A unit quantum efficiency random laser that is analyzed by its integrated spectral radiance falsely suggests a thresholdless laser, one of the holy grails in laser physics [108, 109]. Equation (2.13) and (2.14) also emphasize that a clear definition of the quantity that is plotted versus the input power is required to be able to compare thresholds of different random lasers.

A fit of the experimental peak spectral radiance with Eq. (2.11) gives ϕ and R/γ_c. This second fit parameter scales the power axis. A third fit parameter scaled the y-axis. These fits are shown in Fig. 2.4(a)-(b) and yielded the following values for the quantum efficiency: Rhodamine $\phi = 1 \pm 0.09$, Cresyl Violet $\phi = 0.57 \pm 0.04$, and Nile Blue $\phi = 0.25 \pm 0.02$. A systematic deviation might be caused by the method used for estimating the β-factor [107]. A single random laser experiment thus suffices for analyzing the quantum efficiency of a light source in a complex medium. Using Eq. (2.12) and the measured values for β and ϕ we can make a theoretical prediction for the integrated spectral radiance versus excitation power. These theoretical curves are plotted in Fig. 2.4(c)-(d) and are in great agreement with the experimental data.

As a rule of thumb the β-factor and ϕ can be determined directly *without* fitting from the logarithmic input-output plots. Fig. 2.5 illustrates this rule of thumb procedure by considering curves for the peak and integrated spectral radiance calculated using Eqs. (2.11)-(2.12). To find β and ϕ in these log-log plots, the line connecting the far below threshold output intensities needs to be extrapolated to the above threshold region. The extrapolated line runs parallel to the line connecting the above threshold data points. The ratio between the extrapolated below threshold line and the above threshold line returns ϕ in the case of the integrated spectral radiance, and $\beta\phi$ in the case of the peak spectral

---

[3]By using the spectra below threshold rather than the neat dye spontaneous emission spectra of the gain media, the β-factor is reduced to describing the narrowing of the spectrum. The main advantage of using only spectra obtained from the multiple scattering samples, is that, to a large extent, they automatically take into account reabsorption. Therefore reabsorption in Eqs. (2.8)-(2.10) can be neglected. Technically, this β-factor ceases to be the true spontaneous emission factor, although deviations are only of order 1.
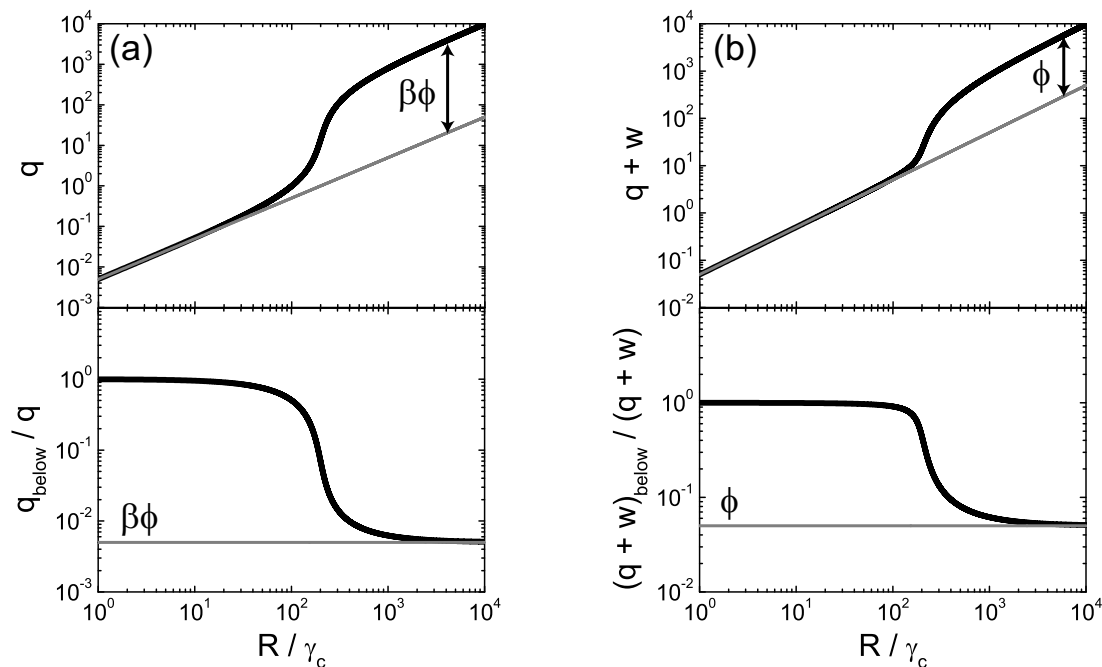
Figure 2.5: Theoretical illustration of the rule of thumb for determining the quantum efficiency and the spontaneous emission factor in random lasers. Values used: $\beta = 0.1$ and $\phi = 0.05$. (a) log-log plot of the peak spectral radiance (black line) versus pump rate. Gray line: extrapolated below threshold peak spectral radiance. The ratio between the below threshold peak spectral radiance and the peak spectral radiance equals $\beta\phi$ as illustrated in the lower panel. (b) log-log plot of the integrated spectral radiance (black line) versus pump rate. Gray line: extrapolated below threshold integrated spectral radiance. The ratio between the below threshold peak spectral radiance and the peak spectral radiance equals ϕ as illustrated in the lower panel.

radiance. Using a Taylor expansion for low pump rates, one can confirm these ratios analytically from Eqs. (2.11)-(2.12). Applying the rule of thumb to our data in Fig. 2.4(b) and (d) gives values for β and ϕ that lie within a factor 2 from the fitted values. From this procedure one understands that log-log input-output graphs are more insightful than linear plots in the field of random lasers.

The remarkable observation of a different behavior of the integrated spectral radiance, that is the total emitted power, for the three random lasers as a function of input power is well explained by the concept of CPS and CAS. The random laser threshold indicates the transition from spontaneous emission to stimulated emission as the main mechanism of radiation. In the case of a gain medium consisting of sources with near unity quantum efficiency, this transition does not influence the ratio between the number of excitation photons that are absorbed and the number of photons that are emitted: the total emitted power scales linearly with the total absorbed power. Hence, we classify these high quantum efficiency dye molecules as CPS for light. The threshold in the peak spectral radiance simply indicates the energy is spectrally redistributed from the wings to the peak of the spectrum. For a gain medium consisting of sources with a low quantum efficiency, the transition from spontaneous emission to stimulated emission also changes the ratio between the non-radiative and the radiative decay channels. The number of transitions is conserved but the load of the radiative decay channel is decreased causing the total emitted power to scale non-linearly with the pump power. Low quantum efficiency molecules should be classified

41

as CAS for light as will be discussed in the following section.

2.4   A classical dipole source in a complex environment

In the previous section we showed how in a random laser invoking stimulated emission of radiation changes the "impedance" of a radiative transition, thereby changing the output power in the case of a low quantum efficiency source. An alternative knob for changing the impedance of the radiative transition is by changing the spontaneous emission decay rate. Such a change can be achieved photonically by engineering the LDOS at the position of the source. In this section, we analyze the output power of a widely used classical dipole source in a complex medium and argue that it is equivalent to a source with a low quantum efficiency. Then a generalized expression for a four-level source is introduced that is based on the rate equation analysis in Sec. 2.1. This generalized expression incorporates both high and low-quantum efficiency sources.

For a point source with constant amplitude, a CAS by definition,

$$j(\mathbf{r}, t) = j_0 \delta(\mathbf{r} - \mathbf{R_s}) \exp(-i\omega t) + \text{c.c.} \tag{2.15}$$

the output power can be calculated by using Green functions. A Feynman representation of the Green function[4] G_ω describing propagation to $\mathbf{r}$ from a unit source ($j_0 = 1$) located at $\mathbf{R_s}$ in presence of a scatterer at $\mathbf{R_x}$ is

$$G_\omega(\mathbf{r}, \mathbf{R_s}) = \underline{\quad} \circledast + \underline{\quad} \times \underline{\quad} \circledast. \tag{2.16}$$

In a homogeneous background, this Green function is given by

$$G_\omega(\mathbf{r}, \mathbf{R_s}) = g_\omega(\mathbf{r} - \mathbf{R_s}) + g_\omega(\mathbf{r} - \mathbf{R_x}) t(\omega) g_\omega(\mathbf{R_x} - \mathbf{R_s}). \tag{2.17}$$

Here g_ω is the bare Green function and $t(\omega)$ is the t-matrix of the scatterer. To find out the power, P_{src}, radiated by the source in Eq. (2.15) we integrate the divergence of the cycle-averaged current $\langle \mathbf{J} \rangle_{\text{cycle}} = \langle \left(\frac{\partial \Psi}{\partial t} \right)^* \nabla \Psi \rangle_{\text{cycle}}$ for an infinitesimally small volume around the source, where the wave amplitude is related to the Green function by $\Psi(\mathbf{r}, t) = j_0 G_\omega(\mathbf{r}) e^{i\omega t} + \text{c.c.}$. The cycle-averaged current and its divergence read

$$\langle \mathbf{J} \rangle_{\text{cycle}} = i\omega |j_0|^2 G_\omega \nabla G_\omega^* - i\omega |j_0|^2 G_\omega^* \nabla G_\omega, \tag{2.18}$$

$$\nabla \cdot \langle \mathbf{J} \rangle_{\text{cycle}} = i\omega |j_0|^2 G_\omega \nabla^2 G_\omega^* - i\omega |j_0|^2 G_\omega^* \nabla^2 G_\omega. \tag{2.19}$$

With definition (1.40) of the Green function at hand, $\nabla^2 G_\omega(\mathbf{r}) = -k^2 \epsilon(\mathbf{r}) G_\omega(\mathbf{r}) - \delta(\mathbf{r})$, the above expression simplifies to

$$\nabla \cdot \langle \mathbf{J} \rangle_{\text{cycle}} = - i\omega |j_0|^2 G_\omega k^2 \epsilon(\mathbf{r}) G_\omega^* - i\omega |j_0|^2 G_\omega \delta(\mathbf{r})$$
$$+ i\omega |j_0|^2 G_\omega^* k^2 \epsilon(\mathbf{r}) G_\omega + i\omega |j_0|^2 G_\omega^* \delta(\mathbf{r}), \tag{2.20}$$
$$= 2\omega |j_0|^2 \delta(\mathbf{r}) \text{Im} G_\omega. \tag{2.21}$$

The last step is only valid when ϵ is real. However, these ϵ terms vanish in any case when integrating over an infinitesimal volume around the source as long as they do not contain

---

[4]In contrast to *chapter 1* the spectral dependence of the Green functions is important here, since light sources often involve multiple frequencies. We therefore denote the frequency of the Green functions explicitly in this section by using a subscript.

delta functions at the source position. Using Eq. (2.20), the output power normalized to the output power in vacuum is found

$$P_{\text{src}}^{\text{CAS}}/P_0 = \int_{V \to 0} \nabla \cdot \mathbf{J} d\tau \bigg/ \int_{V \to 0} \nabla \cdot \mathbf{J_0} d\tau = \frac{4\pi c}{\omega} \text{Im} G_\omega(\mathbf{R_s}, \mathbf{R_s}) \equiv \frac{4\pi^2 c^3}{\omega^2} \rho(\mathbf{R_s}, \omega),$$

(2.22)

where P_0 is the emitted power without the scatterer present and ρ is the LDOS. The final step is only valid for absorption-free environments. We prefer to phrase our discussion in terms of LDOS, but the reader is notified that external absorption can easily be included by replacing the LDOS with[5] $\frac{\omega}{\pi c^2} \text{Im} G_\omega$. The emitted power is thus dependent on the LDOS, which acts as the inverse of a load on the source. This dependence of the output power on the environment is valid for any complex system. Since the emitted power can both be higher and lower compared to the vacuum situation, the CAS we introduced in Eq. (2.15) is clearly different from a CPS. This result might be counterintuitive, but can be interpreted as follows. Feedback onto the source induced by scattering requires the source to radiate more or less energy, in order to keep the amplitude of the source constant.

Source (2.15) with a constant amplitude is precisely the source that was used to derive the C_0-correlation in Sec. 1.3.2. When the LDOS of a medium exhibits strong spatial fluctuations, the output power of a CAS will depend on the source position correspondingly. As a consequence these fluctuations in the output power result in speckle patterns with an offset in intensity compared to the ensemble averaged intensity. These offsets yield the infinite range correlations induced by a source. The equivalence of the C_0-correlation with fluctuations in the LDOS [110] is thus a natural outcome of starting the analysis with a CAS in the first place.

2.4.1 Generalized expression for a source

The steady-state rate equation analysis in Sec. 2.1 showed that the photon production rate for a source with nonradiative and radiative decay channels in the absence of stimulated emission is proportional to $\Gamma_e \frac{\gamma_r}{\gamma_r + \gamma_{\text{nr}}}$. When $\gamma_{\text{nr}} \gg \gamma_r$, the output power normalized to the output power in vacuum equals $\gamma_r/\gamma_r^{(0)} = \rho(\mathbf{R_s}, \omega) \frac{4\pi^2 c^3}{\omega^2}$, where we have applied Fermi's Golden Rule to express the radiative decay rate in terms of LDOS. This power is precisely the expression found for the CAS in Eq. (2.22). Therefore we conclude that a low quantum efficiency source is accurately described by a CAS. Our goal is to generalize the axiomatic expression for CAS, in such a way that the new expression incorporates high quantum efficiency sources as well. To do so, we adjust the source term such that the resulting power becomes proportional to $\Gamma_e \frac{\gamma_r}{\gamma_r + \gamma_{\text{nr}}}$, that is

$$P_{\text{src}}/P_0 = \frac{\gamma_r}{\gamma_r + \gamma_{\text{nr}}} \bigg/ \frac{\gamma_r^{(0)}}{\gamma_r^{(0)} + \gamma_{\text{nr}}} = \frac{4\pi^2 c^3}{\omega^2} \rho(\mathbf{R_s}, \omega) \frac{\gamma_r^{(0)} + \gamma_{\text{nr}}}{\gamma_r + \gamma_{\text{nr}}}.$$

(2.23)

This equation implies the original expression (2.15) for a CAS needs to be adjusted to

$$j(\mathbf{r}, t) = \sqrt{\frac{\Gamma_e}{\gamma_r + \gamma_{\text{nr}}}} \delta(\mathbf{r} - \mathbf{r_0}) \exp(-i\omega t) + \text{c.c.}.$$

(2.24)

---

[5]The relationship between the LDOS and the imaginary part of the Green function sometimes appears in the literature with an additional minus sign. This sign is caused by multiplying the scalar Helmholtz Eq. (1.31) with a factor -1.

This is our generalized expression for a light source. In the case of a CPS ($\gamma_{\text{nr}} = 0$), the output power is independent of the environment, whereas in the case of a CAS ($\gamma_{\text{nr}} \gg \gamma_r$) the output power depends on the radiative decay rate and thus the local environment of the emitter. The amplitude of a CAS is given by $\sqrt{\Gamma_e/\gamma_{\text{nr}}}$. In our derivation we have assumed a constant, non-photonic excitation rate and a rapidly decaying atomic coherence. Our analysis needs to be expanded when the system is pumped into saturation, since in the case of saturation a change in the total decay rate will also change the excitation rate.

To find the correct wave function from a single source or collection of sources,

$$\psi(\mathbf{r}) = \int G_\omega(\mathbf{r}, \mathbf{r_0}) j\{G_\omega(\mathbf{r_0}, \mathbf{r_0})\} d\mathbf{r_0}, \tag{2.25}$$

then becomes very involved since it requires knowledge of the Green function for both the propagation and the generation of light. Although this dramatically hinders analytic calculations, it should be straightforward to correctly adjust the source strength in numerical calculations as we show in the next section. Introducing stimulated emission into our analysis and eventually into Eq. (2.24) leads to an increase in the radiative decay rate. This increase leaves a CPS unaltered, but a CAS will start to look more like a CPS. Stimulated emission and the LDOS can thus both be used to engineer light sources with $\gamma_r/\gamma_{\text{nr}}$ as control parameter.

2.5 Numerical example: 1D localization

In this section it is shown how a CAS and CPS lead to very different results in numerical calculations. A clear definition of the used source is therefore essential. Our goal is to find a theoretical estimate for the localization length in a 1D random system from the ensemble averaged intensity distribution of an embedded source. Figure 2.6 illustrates the system. This system becomes experimentally relevant in the next chapter, when microwave propagation is studied in a (1+1)D system. To find the localization length, we set up a transfer matrix model [111, 112]. The transfer matrix $\mathbf{S}$ relates the incoming electric field E_0 to the transmitted electric field in layer $m+1$ E_{m+1}.

$$\begin{bmatrix} E_0^+ \\ E_0^- \end{bmatrix} = \begin{bmatrix} S_{11} & S_{12} \\ S_{21} & S_{22} \end{bmatrix} \begin{bmatrix} E_{m+1}^+ \\ E_{m+1}^- \end{bmatrix}. \tag{2.26}$$

Here the $+$ and $-$ denote a forward and a backward propagating wave respectively. The total transfer matrix is calculated by multiplying transfer matrices of the interfaces $\mathbf{I}_{jk}$ between the bars and air with diagonal propagation matrices $\mathbf{L}_j$:

$$\mathbf{S} = \prod_{v=1}^{m} \mathbf{I}_{(v-1)v} \mathbf{L}_v = \begin{bmatrix} e^{-i\beta_j d_j} & 0 \\ 0 & e^{i\beta_j d_j} \end{bmatrix}; \qquad \mathbf{I}_{jk} = \frac{1}{t_{jk}} \begin{bmatrix} 1 & r_{jk} \\ r_{jk} & 1 \end{bmatrix}, \tag{2.27}$$

where r_{jk} and t_{jk} are the Fresnel complex reflection and transmission coefficients respectively. The electric field at position x in layer j of the medium can be calculated by using the transfer matrices to the left $\mathbf{S}'_j$ and right side $\mathbf{S}''_j$ of the layer:

$$E_j(z) = \frac{S''_{j11} e^{-i\beta_j(d_j-z)} + S''_{j21} e^{i\beta_j(d_j-z)}}{S'_{j11} S''_{j11} e^{-i\beta_j d_j} + S'_{j12} S''_{j21} e^{i\beta_j d_j}} E_0^+, \tag{2.28}$$
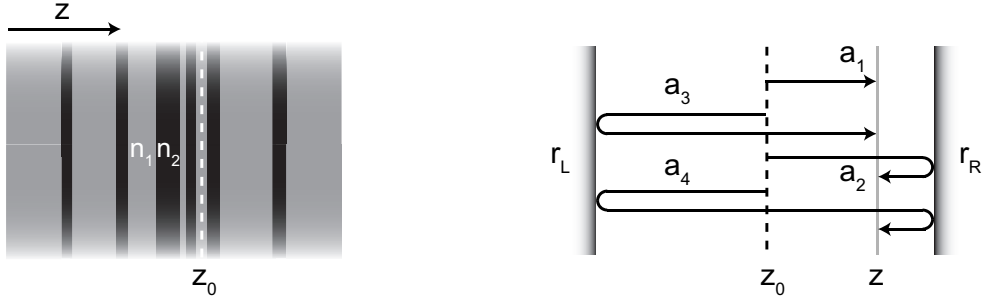
Figure 2.6: (left) The transfer matrix model calculates the intensity distribution inside a 1D dielectric stack with refractive indices n_0 and n_1 due to a source at z_0 (dashed line). (right) The dressed Green function describing propagation from the source z_0 to z inside the hostlayer has four contributions. The higher order terms due to repetitive scattering from the left and right stack are included by geometric series.

where $\beta_j = k_0 n_j$ with k_0 the vacuum wave number and n_j the refractive index of the layer, and d_j is the thickness of layer j.

The above formalism only considers side excitation. In order to take the excitation from a source into account we expand our analysis with a Green function approach. We assume a unit CAS at position z_0 in the middle of a hostlayer with thickness L_d that is surrounded by a stack on the left and right side. This amplitude source radiates a propagating wave with amplitude $\frac{i}{2\beta_h}\exp(i\beta_h|z - z_0|)$, where β_h denote the propagation constant in the hostlayer. The reflection coefficient of the left r_L and right stack r_R can be calculated with transfer matrices. The dressed Green function inside the hostlayer at position z is then constructed out of four parts [113], as depicted graphically on the right side of Fig. 2.6:

$$G(z, z_0, \omega) = \frac{i}{2\beta_h}(a_1 + a_2 + a_3 + a_4), \tag{2.29}$$

$$a_1 = \frac{\exp(i\beta|z_0 - z|)}{1 - r_L r_R \exp(i\beta 2L_p)} \tag{2.30}$$

$$a_2 = \frac{r_R \exp(i\beta(L_p - z_0 - z))}{1 - r_L r_R \exp(i\beta 2L_p)} \tag{2.31}$$

$$a_3 = \frac{r_L \exp(i\beta(L_p + z_0 + z))}{1 - r_L r_R \exp(i\beta 2L_p)} \tag{2.32}$$

$$a_4 = \frac{r_R r_L \exp(i\beta(2L_p - |z - z_0|))}{1 - r_L r_R \exp(i\beta 2L_p)}. \tag{2.33}$$

These four elements are all the sum of a geometric series as seen by the denominator, while the numerator describes how the wave can reach point z without having made a full round trip in the host layer: namely without reflecting from the boundaries (a_1), with one reflection from either the left (a_3) or the right boundary (a_2) or by reflecting once from both the left and the right boundary (a_4).

Since we now know the forward and backward propagating wave entering the left and right stack, we can use the transfer matrix model, Eq. (2.28), to recover the electric field in the whole sample. The forward propagating wave E_0^+ for the right sample consists of $\frac{i}{2\beta}(a_1(\frac{1}{2}L_p) + a_3(\frac{1}{2}L_p))$ and for the left sample of $\frac{i}{2\beta}(a_1(-\frac{1}{2}L_p) + a_2(-\frac{1}{2}L_p))$.

A system consisting of 50 layers on the left side and 50 layers on the right side of the host layer is considered. The frequency of the radiation is set at 9 GHz and the layers have
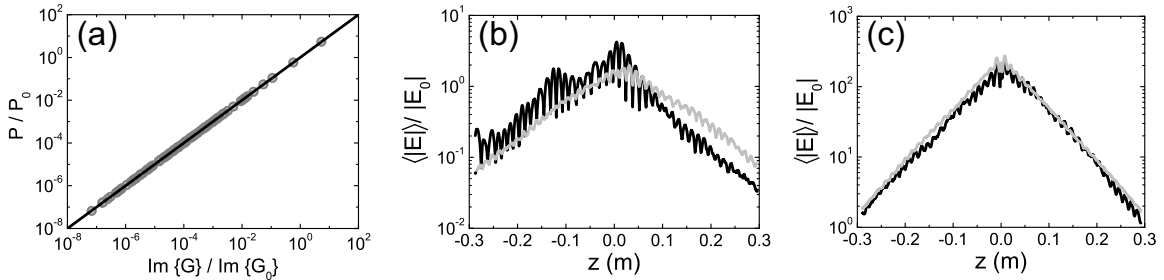
Figure 2.7: (a) Calculated output power versus imaginary part of the Green function for 100 1D stacks of air and nylon layers on a log-log plot at 9 GHz. Both quantities are normalized to their values in vacuum. Light gray disks: power calculated using net current generated by the source. Gray open circles: power calculated using intensity in the outer layers. The black line indicates equality between the y-and x-axis. (b) Ensemble averaged amplitude profile for 100 (black) and 1000 (gray) samples obtained with a CAS. (c) Ensemble averaged amplitude profile for 100 (black) and 1000 (gray) samples obtained with a CPS.

refractive indices of 1 (air) and 1.73 (nylon). The thickness of the air layers is given by a Poissonian distribution with mean 10 mm. The thickness of the nylon layers is fixed at 3 mm. Figure 2.7(a) shows a plot of the output power of the source versus the imaginary part of the Green function for 100 different realizations of disorder. The output power was evaluated by both calculating the net current around the source and by calculating the intensity in the outer layers. The two methods yielded identical results. As expected from our analysis in Sec. 2.4 the output power is linearly related to the imaginary part of the Green function at the source position.

Next, we consider the ensemble averaged amplitude distribution of 100 and 1000 samples obtained with a CAS as plotted in Fig. 2.7(b). The amplitude profiles do not converge, which becomes particularly clear at the right side of the profiles. Instead, the ensemble averaged amplitude profiles are dominated by a handful elements of the ensemble that happen to have a high LDOS at the source position. In the case of a CAS ensemble averaging is of little use. For a CPS on the other hand, displayed in Fig. 2.7, the ensemble averaged intensity profile converges. The profiles can be used to fit a localization length ξ. For the parameters under consideration, we find $\xi = 6.1$ cm in the case of a CPS. Remarkably the localization length obtained in case of the CAS ensemble averaged data is significantly higher, namely $\xi = 9.7$ cm, which again stresses the importance of using a well-defined source.

2.6 Conclusion and discussion

We have developed a new classification scheme for four-level light sources. Sources with unit quantum efficiency are classified as constant power sources for light and those with a low quantum efficiency are classified as constant amplitude sources. We demonstrated that this classification directly influences the interpretation of photonic experiments. In the case of a CAS, both stimulated emission and changes in the LDOS alter the load of the radiative transition and thereby the output power. Full control over sources could be achieved when the LDOS is made artificially small, *e.g.*, by constructing photonic crystals around the source, and at the same time the power of a control beam is used to engineer the radiative decay rate by stimulated emission.

In random lasers, stimulated emission leads to an increased output power for low quantum efficiency sources. An extended rate equation model enables us to extract the quantum efficiency from the development of the integrated spectral radiance as a function of pump power. Our experimental studies emphasize the importance of a clear definition of the reported threshold and illustrate a possible application of random lasers in the future.

In passive random media, recently predicted infinite range correlations are caused by an interaction between a CAS and a nearby scatterer [51]. Since for a classical dipole source this C_0 correlation is equivalent to fluctuations in the LDOS [110, 114], it is very likely that a CPS will yield different results. For a CPS the equivalence between intensity fluctuations and decay rate fluctuations [115] disappears and as a consequence decay rate fluctuations cannot be used to measure the C_0-correlation. Experimentally, infinite range intensity correlations are probably easier to observe by a fluctuating LDOS at the excitation rather than the emission frequency. Since in such a situation the use of high quantum efficiency sources also leads to different output power. In practice, this requires a more complicated measurement scheme since emission can then no longer be used to simultaneously measure the LDOS and the C_0-correlation [116]. Our work assists in choosing the right type of source for the desired measurement. Studying how other type of sources such as three-level systems and second harmonic generation fit within our framework might lead to new insights on the behavior of sources in random media.

Probing the dynamics of Anderson localization through spatial mapping

In this chapter (1+1)D transverse localization of electromagnetic radiation at microwave frequencies is studied by two-dimensional spatial scans. Since the longitudinal direction can be mapped onto time, our experiments provide unique snapshots of the build-up of localized waves. The ensemble averaged evolution of the wave functions is in great agreement with numerical calculations. The excitation of the system with a source in its close vicinity leads to oscillatory behavior of the wave functions. These oscillations are explained in terms of a beating between the system's eigenstates.

3.1   Transverse localization

Recent years witnessed a renaissance in experimental studies on Anderson localization. This phenomenon, introduced in Sec. 1.2.5, originally described the absence of diffusion of electrons in random lattices due to interference [61]. Since Anderson localization is in essence a wave phenomenon, physicists have successfully extended the scope of localization studies to electromagnetic waves [117–120], ultrasound [69], and matter waves [121–123].

Similar to other phase transition phenomena, dimensionality plays an important role. For $d \leq 2$, all states are localized, whereas for $d = 3$ a phase transition from diffusive to localized behavior occurs at a critical scattering strength [62]. In the special case of transverse localization, formulated by De Raedt *et al.* [124], one dimension is designed not to be disordered, whereas disorder is introduced in the other dimension(s). As a consequence, waves spread out in the disorder-free dimension, but are confined in the other dimensions. Waves are always localized in the transverse directions as long as the transverse system length L is larger than the localization length ξ. In the paraxial limit transverse localization is described by an equation which closely resembles the time-dependent Schrödinger

equation [124] where z plays the role of time

$$i\frac{\partial \psi}{\partial z} = \frac{1}{2kn_0}H\psi,$$ (3.1)

with ψ the wave field and k the vacuum wave number. The effective index of refraction is given by $n_0^2 \equiv L^{-1}\int_L n^2(x)dx$. The Hamiltonian is defined as

$$H \equiv \frac{\partial^2}{\partial x^2} + k^2[n^2(x) - n_0^2].$$ (3.2)

Effectively, transverse localization reduces the number of spatial coordinates in the system: the coordinate along which the sample is extruded can be seen as the time-axis in the time-dependent Schrödinger equation. Stationary transverse localization experiments could thus provide a unique insight into how a localized wave develops over time. Studying and understanding this intriguing aspect of transverse localization experimentally is the central topic of this chapter.

Pivotal experiments on weakly scattering disordered photonic lattices [34, 125, 126] have focussed on the observation of localized wave functions after a certain fixed propagation distance and the effect of nonlinearity on the transverse localization length. Both theoretical and experimental studies have revealed interesting dynamical properties of the periodically kicked quantum rotator which bears close resemblance to Anderson localization [127, 128], suggesting that studying the dynamics of localization itself is important. The unique property of transverse localization experiments that enables us to map one spatial dimension onto time is ideally suited for this purpose.

The experimental apparatus used to study transverse localization with microwaves is discussed in Sec. 3.2. Ever since localization was introduced for classical waves, the issue of absorption has been the subject of immense discussions and various opinions [117, 129]. Tackling this issue has shown to be unavoidable in any experiment [66, 67, 130–132]. Our measurements are performed on samples consisting of scattering bars placed parallel to each other in an open system. In such samples out-of-plane scattering plays the role of dissipation and we therefore analyze what the impact of these losses is on our experiment. The size of the nylon bars is small compared to the wavelength and therefore guided modes are leaky in x-direction. As a consequence our system cannot be analyzed in terms of a coupled set of discrete Schrödinger equations [125]. The experimental results on disordered samples are presented in Sec. 3.3. Instead of probing the intensity at the end of our samples, our experiment allows us to study the evolution of the extent of the waves as a function of propagation distance. In Sec. 3.4, the experimental results are compared with numerical solutions to the 2D Schrödinger-like equation. Interesting non-stationary behavior of single wave functions is observed. These oscillations are analyzed by decomposing these functions into the system's eigenstates semi-analytically. We discuss how the source of radiation that is used to excite the system influences the dynamics of the wave functions.

3.2 Experimental methods

Figure 3.1 shows a sketch of the experimental apparatus. Samples were fabricated by placing nylon bars (3 mm × 10 mm × 1000 mm) on top of an oxygen free copper plate (500 mm × 1000 mm). These nylon bars ($n = 1.73$ at 10 GHz [133]) are the scatterers in our system. Disorder was introduced into the system by varying the spacing between the nylon bars.
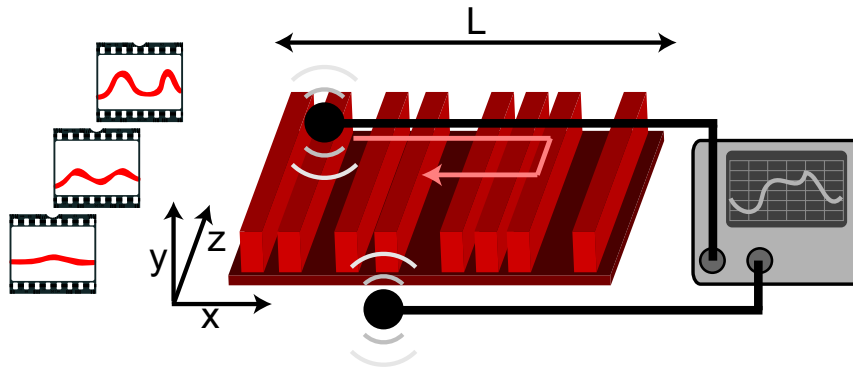
Figure 3.1: Experimental set-up. Nylon bars (red) are placed on top of an oxygen free copper plate, the distance between the bars is random in the transverse x-direction. The z-direction is disorder free. One of the two microwave antennas (black disks) is scanned over the sample and a vector network analyzer is used to measure the transmitted spectrum between the two antennas. Each scan along the x-axis is equivalent to a snapshot in time.

The spacings were chosen randomly from a Poissonian distribution with a mean of 10 mm, and a minimum of 1 mm. Introducing Poissonian disorder makes sure that the presence of stop band effects is negligible [134]. Styrofoam spacers ensured parallel alignment of the nylon bars. The samples were studied by measuring the microwave transmission spectrum around 10 GHz using a vector network analyzer (Rhode and Schwartz ZVA 67). Two coax-to-waveguide adapters functioned as antennas. The detection antenna was scanned over the sample by using a stepper motor (Newport ESP 301) and a home-built scanning stage. A typical two-dimensional scan (40 cm × 40 cm with ∼4000 spatial measurement points and 200 spectral points) took approximately 2.5 hours. The excitation antenna was aligned along the z-axis, whereas the detection was aligned along the y-axis.

The end facets of both antennas are placed in the near-field of the sample. This measurement scheme has two advantages. First, the source radiates over a large range of solid angles that is caused by diffraction of waves at the end facet of the waveguide adapter. In contrast to plane wave excitation, such a source has the capability of exciting modes with different k-vectors at once. Second, the evanescent waves that are due to wave guiding in the nylon bars can be detected.

3.2.1 Measurement characterization

To test our experimental apparatus and to investigate the photonic strength of the nylon bars, periodic structures were used. An ordered sample was fabricated with a lattice spacing of 20 mm. The transmission spectrum of such a Bragg stack [135, 136] was measured in a waveguide configuration by putting a second copper plate on top of the sample and by placing the two antennas opposite to each other perpendicular to the position of the bars. The spectrum of an empty waveguide was taken as a reference. Figure 3.2(a) shows that the transmission of the Bragg stack drops significantly around 7, 13, and 20 GHz. In 1D, the spectral and angular positions of the stopbands in a periodic structure can be calculated analytically [136]. The calculated stopbands at normal incidence are shown by the gray shaded areas in the spectrum of Fig. 3.2(a). The minima in transmission correspond with the position of the calculated stopbands, from which we conclude our sample is photonic and the refractive index of the nylon bars is in agreement with the used literature value.
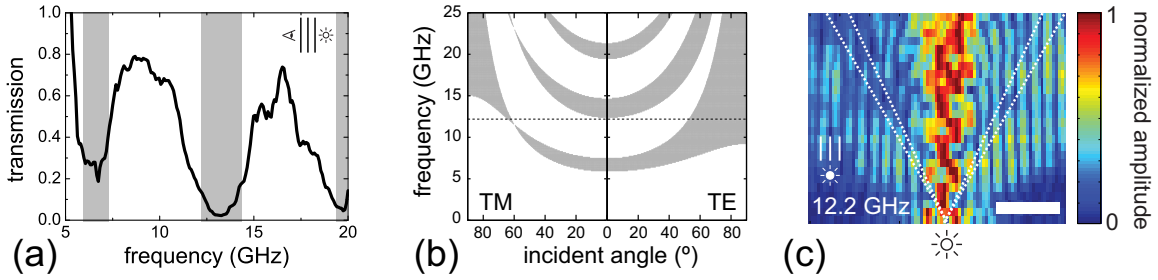
Figure 3.2: (a) Measured transmission spectrum for a Bragg-stack of nylon bars and air layers. The small cartoon illustrates the position of the two antennas with respect to the alignment of the nylon bars. The gray shaded areas indicate the calculated stop bands. The structure consists of alternating air ($n = 1$, $d = 17$ mm) and nylon ($n = 1.73$ and $d = 3$ mm) layers. (b) Calculated band diagram for TM and TE polarized waves. Black dashed line: frequency of spatial scan. (c) False color image of the measured amplitude distribution above the surface of the Bragg stack at 12.2 GHz. White lines: angular position of the TM stop band. White scale bar: 100 mm.

The complete band diagram, Fig. 3.2(b), shows that TM and TE polarized waves behave differently when the angle of incidence becomes larger. For TE modes propagation along the bars (corresponding to an incident angle of 90°) is impossible for frequencies larger than ∼10 GHz, whereas for TM modes propagation along the bars is allowed until ∼15 GHz. Moreover, around 11 GHz waves are allowed to propagate in nearly all directions for TM modes. The two-dimensional scanning scheme enables us to study the full band diagram experimentally. Figure 3.2(c) provides the distribution of the field amplitude obtained by a two-dimensional spatial scan above the surface of the Bragg stack at 12.2 GHz. The data was normalized for every row to enhance the visibility of the wave function far away from the source. Most of the measured radiation propagates in forward direction parallel to the orientation of the bars. For a small range of angles the radiation is suppressed. These angles correspond with the calculated stopbands of the TM modes. Thus, the orientation of our detection antenna is such that it primarily picks up the evanescent waves of the TM mode, which is a consequence of the perpendicular alignment of the detection and excitation antenna.

The impact of losses

Our "open" experimental configuration requires that we analyze the role of out-of-plane scattering in our experiment. In Fig. 3.3(a), the integrated transmitted intensity between the two antennas is plotted versus propagation distance for a 1D photonic crystal with 2 cm lattice spacing at 9.2 GHz and 12.2 GHz. For the measurement at 12.2 GHz, the integrated intensity drops by about 50% in the first 10 cm. After 300 mm of propagation the integrated intensity flattens off. A similar trend is observed for the data at 9.2 GHz. The first 100 mm witnesses a drop in intensity of a factor 4, but from that point onwards the integrated intensity hardly decreases anymore. These trends indicate that contributions from out-of-plane scattering are foremost present close to the excitation antenna. Far away from the excitation antenna, the main contribution of the detected fields stems from the evanescent waves surrounding the nylon bars. These waves experience very low loss and therefore the integrated intensity hardly decreases anymore.

Theoretically the role of homogeneous dissipation or out-of-plane scattering can be analyzed by adding a term $-i\alpha$ to H in definition (3.2) creating an effective Hamiltonian
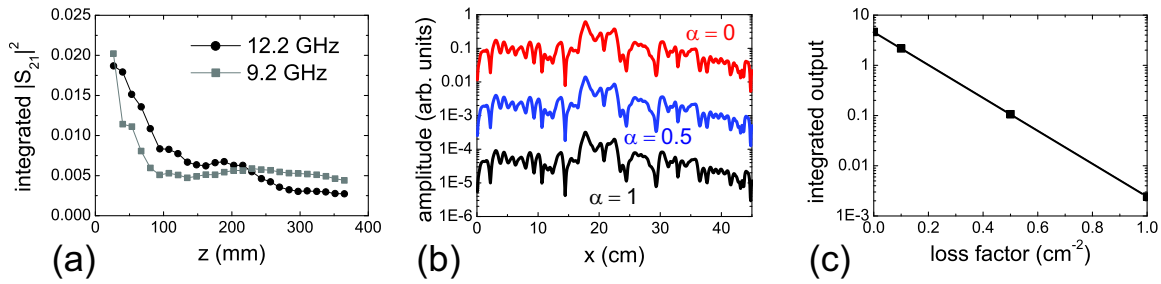
Figure 3.3: (a) Integrated transmitted intensity versus propagation distance measured for a 1D photonic crystal at 12.2 GHz (black dots) and at 9.2 GHz (gray dots). The data for 9.2 GHz has been scaled down with a factor 10. (b) Calculated mode amplitude profile versus transverse distance for different values of the loss coefficient α after 350 mm of propagation. Red: $\alpha = 0$ cm^{-2}. Blue: $\alpha = 0.5$ cm^{-2}. Black: $\alpha = 1$ cm^{-2}. (b) Calculated integrated output versus loss coefficient on a semilog scale.
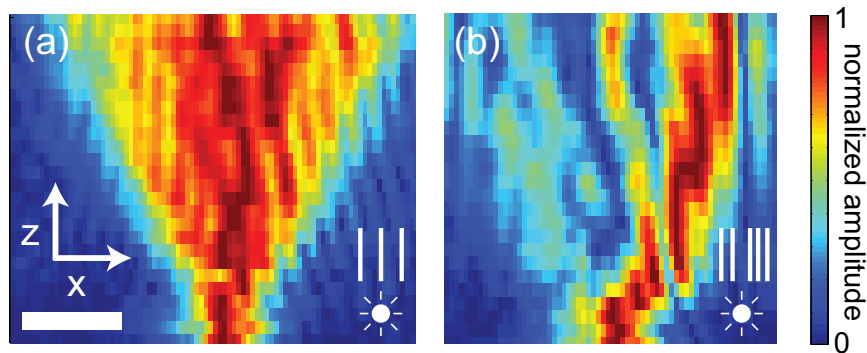
Figure 3.4: Experimentally determined amplitude distribution for (a) an ordered and (b) a disordered sample at 9.2 GHz . Every row is normalized independently. The scale bar denotes 100 mm.

that also describes losses. The amplitude profile is calculated after 350 mm of propagation for a single realization of disorder for various values of α. To calculate the amplitude, partial differential Eq. (3.1) is rewritten as a set of ordinary differential equations in z by using the method of lines [137]. After separating the real and imaginary part of ψ, we use MatLab to solve the equation numerically by means of a Runge-Kutta algorithm. The xz-plane is discretized in $600{\times}200$ steps. Figure 3.3(b) plots the amplitude profile for different values of α. For higher values of the absorption coefficient, the amplitude decreases, but the wave function shape does not alter. We conclude from these curves that absorption merely scales the wave intensity thereby supporting our experimental approach of studying transverse localization in the possible presence of out-of-plane losses. In Fig. 3.3(c), the integrated output is plotted versus the absorption coefficient. The output intensity clearly attenuates exponentially, confirming that homogeneous dissipation only introduces an exponential scaling [130].

3.3 Results on disordered samples

The propagation of waves within an ordered and a disordered sample is shown in Fig. 3.4. The excitation frequency was set at 9.2 GHz. At this frequency the angular position
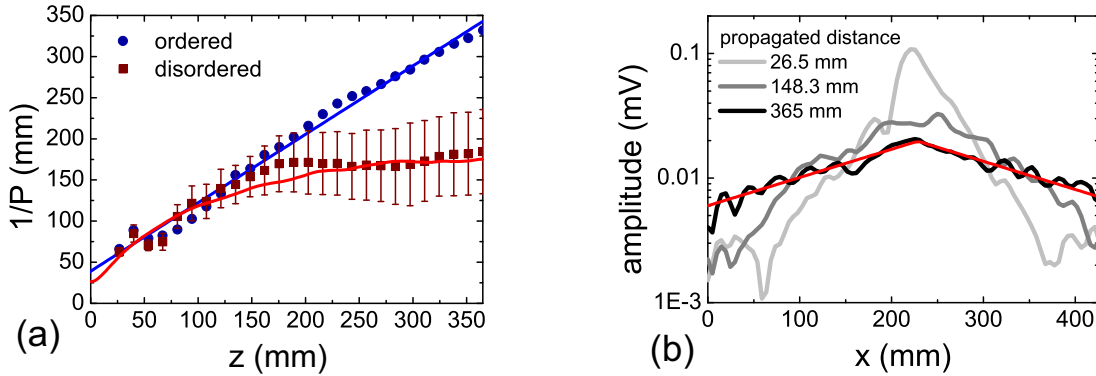
Figure 3.5: (a) Participation ratio versus propagation distance at 9.2 GHz for an ordered sample (blue) and a disordered ensemble (red). Red line: calculation for an ensemble of 100 disordered samples. Blue line: linear fit. (b) Transverse ensemble averaged amplitude distribution for different propagation distances. Red line: exponential fit.

of the stop gap hardly affects the diffraction from the excitation antenna. The data was normalized for every row in the xz-plane to enhance the visibility of the wave function far away from the source. In the ordered sample, Fig. 3.4(a), waves spread out ballistically as a function of propagation distance. However, for the disordered sample, Fig. 3.4(b), the wave propagation is strikingly different: the wave initially spreads out, but at a certain stage stays confined to a bounded region. In contrast to the amplitude distribution in the ordered sample, the amplitude in the disordered sample is not symmetric around the source position. These type of two-dimensional spatial scans provide us with exceptional data for analyzing transverse localization in unprecedented detail. In this section, we start by studying ensemble averaged data and then focus on single realizations.

3.3.1 Ensemble averaged data

In order to quantify the transverse confinement of wave intensity as function of propagation distance, the inverse participation length (IPL) [138] is calculated. The IPL for a one-dimensional intensity distribution $I(x)$ is defined as

$$P(z) \equiv \frac{\int I^2(x, z)\mathrm{d}x}{\left(\int I(x, z)\mathrm{d}x\right)^2} \tag{3.3}$$

and has a unit of inverse length. The IPL is inversely proportional to the spread of the wave function: a homogeneously extended wave spread out over the entire sample length L leads to an IPL of $1/L$. To obtain a reliable value for the spread of wave functions, the ensemble averaged intensity profiles were determined by averaging over 20 realizations of disorder.

Figure 3.5(a) shows how the inverse of the IPL develops with increasing propagation distance for both the ordered sample and the ensemble of disordered samples at 9.2 GHz. In agreement with the qualitative picture we obtained from Fig. 3.4, we see that the extent of the wave intensity given by the inverse of the IPL increases linearly for the ordered sample. For the disordered ensemble on the other hand the IPL flattens off after a certain propagation distance. This settling of the IPL to a finite value constitutes a direct experimental observation of the spatial evolution of transversely localized waves.
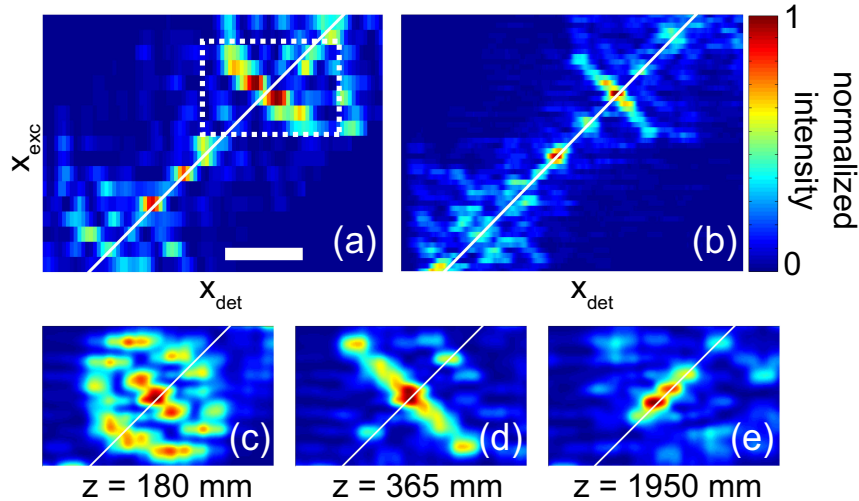
Figure 3.6: (a) Experimental and (b) numerically calculated plots of the normalized wave function intensity in transverse direction after 365 mm of propagation along the z-direction for different positions of the excitation antenna at 9.2 GHz. The white lines indicate the position of the excitation antenna. The dashed box marks an anti-diagonal wave profile. Scale bar denotes 100 mm. (c)-(e) show calculations using mode decomposition for the area marked with the dashed box in (a) for 180, 365, and 1950 mm of propagation respectively. Beating of eigenmodes can result in (c) circular, (d) anti-diagonal, or (e) diagonal patterns.

Besides a different evolution of the waves' extent, the eventual spatial shape of the ensemble averaged wave function changes while propagating through the sample. In contrast to Gaussian shaped extended wave functions, ensemble averaged localized wave functions obtain exponential tails. Figure 3.5(b) shows the ensemble averaged wave function profile for three different propagation distances on a semi-logarithmic scale. Close to the excitation source, the ensemble averaged wave function is strongly peaked in the transverse dimension. For longer propagation distances, the intensity in the wings of the wave function increases and the peak becomes less pronounced. The ensemble averaged wave function quenches once the IPL saturates. Its shape is well described by an exponential. However we note that the decay in amplitude is too little to make conclusive statements on its shape. From an exponential fit to the data we find a characteristic length of 192 ± 6 mm. This length might come as a surprise since in the previous chapter we calculated localization lengths for the same type of structures that were on the order of 100 mm. The deviation between this experimental value and this transfer matrix result is due to the excitation of the sample by a source in the near-field. Analyzing the system by one k-vector as done in the transfer matrix model is then invalid. In that sense, the characteristic length found by fitting the data in Fig. 3.5(b) does not represent the localization length, but rather a localization length averaged over several k-vectors. In the next sections, we will see how the near-field excitation leads to another unexpected result

3.3.2 Single realizations of disorder

After having studied these ensemble averaged properties of our system, we now aim to understand the propagation of waves for single realizations of disorder. To map a sample completely, two-dimensional scans were taken for different positions of the excitation
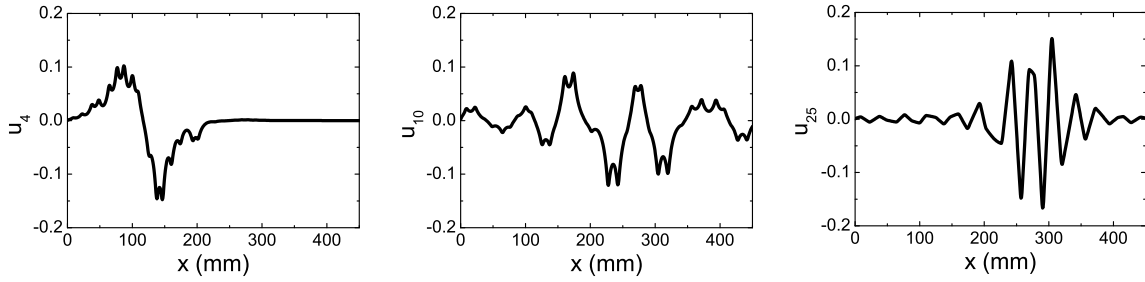
Figure 3.7: Three eigenstates of the transverse localization Hamiltonian. The eigenstates are normalized such that $\langle u_n | u_n \rangle = 1$.

antenna. This measurement procedure allows us to construct excitation maps.

In Fig. 3.6(a), the spatial profile for 17 different excitation positions in one sample after 365 mm of propagation is plotted. Based on Fig. 3.5, this distance ensures we are looking at wave functions of which the IPL is saturated. The individually measured spatial profiles are strongly dependent on the position of the excitation antenna. To a large extent the detected radiation follows the position of the excitation antenna as indicated by the white diagonal. The excitation map displays a high degree of symmetry along the diagonal. Naively, one might expect for a localizing sample clearly isolated regions of higher intensity that are independent on the position of excitation. Such patterns would appear as vertical stripes in Fig. 3.6(a) and represent the localized modes of the sample. However, much to our surprise, the spatial patterns of these isolated regions along the transverse dimension x are dependent on the excitation position. In fact, for the measurement shown in Fig. 3.6, some patterns appear to be anti-diagonal.

3.4 Model

In order to build a basis for understanding the ensemble averaged data and the remarkable excitation dependence of localized wave functions in single realizations of disorder, the system is analyzed numerically and semi-analytically. Numerically, the system is solved by rewriting the Schrödinger like Eq. (3.1) as a set of ordinary differential equations and using a Runge-Kutte routine, as explained in Sec. 3.2. The initial wave at $z = 0$ is modeled as a Gaussian with a width of 1.15 cm given by the aperture of the excitation antenna. To compare the numerical calculation with experiment, we convolved the intensity of the calculated wave function with the aperture of the detection antenna.

In Fig. 3.5(a), the mean of the participation length for an ensemble of 100 realizations of disorder was shown. This theoretical value for the waves' extent falls within the standard deviation of the experimentally determined values. Motivated by the experimentally observed and unforeseen excitation dependence of the wave functions, we also calculated the excitation-detection patterns. In Fig. 3.6(b), it is shown that the position and shape of these patterns roughly correspond with the measurements. The anti-diagonal shapes are also clearly present in our numerical calculation, indicating that they are not caused by spurious effects such as mode perturbation due to the proximity of the receiver antenna.

An alternative analysis of the system in terms of eigenstates rather than the previous "brute force" numerical calculation has the advantage of reducing the problem's complexity. When $\alpha = 0$, the solutions to Eq. (3.1) can be written as a linear combination of the Hamiltonian's eigenstates $u_n(x)$: $\psi(x, z) = \sum_n c_n u_n(x) \exp(-i\lambda_n z)$, where λ_n is the eigenvalue
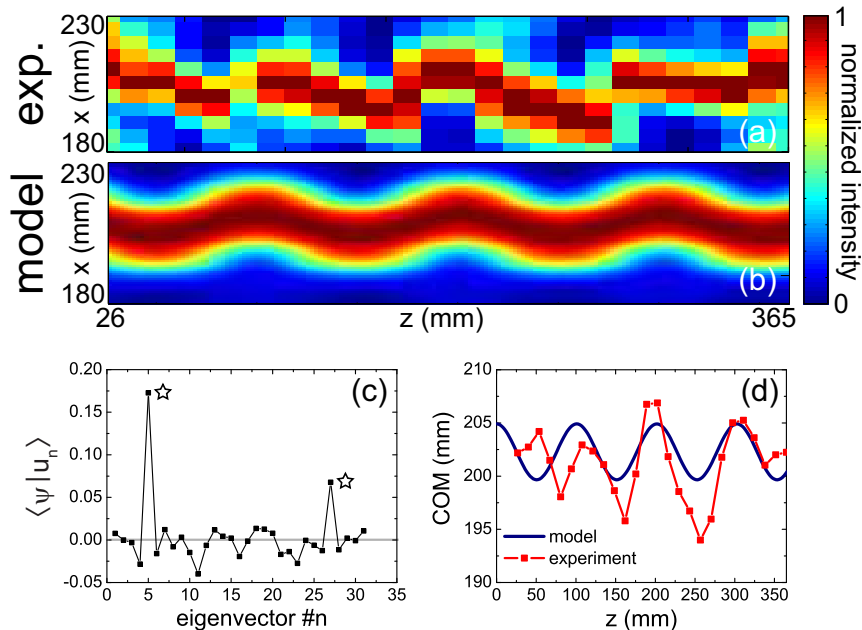
Figure 3.8: (a) Experimental and (b) calculated oscillations in the intensity profile for one sample excited at 10.2 GHz. Every column is normalized independently. (c) Expansion coefficients for the different eigenstates. Only two eigenstates, indicated by the stars, contribute significantly. (d) Center of mass of the intensity versus propagation direction for both the calculated and experimental data shown in (a) and (b).

belonging to eigenstate u_n and c_n is the n'th expansion coefficient given by $c_n = \langle \psi | u_n \rangle$. The eigenstates and eigenvalues are calculated by diagonalizing a 598×598 matrix. The diagonal of the matrix contains the potential $k^2 [n^2(x) - n_0^2]$ and the derivative in x is approximated by using central differences creating a tridiagonal matrix when assuming absorbing boundary conditions. In principle, diagonalizing a $N \times N$ matrix results in N eigenvalues and eigenstates. However, most of these eigenvectors contain too high spatial frequencies, $k_n > k$, that are not excitable in our system. Figure 3.7 shows three calculated eigenstates for one of the disordered samples used in experiment. By calculating the Fourier spectrum of these eigenstates, one can analyze whether the states are excitable. As a result of this Fourier analysis, we end up with only 30 eigenstates that obey the relation $k_n \leq k$ for $f = 9.2$ GHz. This number could have been anticipated, since the total number of modes in our 1D system is given by $2Lf/c \approx 30$. The number of modes that are excited depends on the source used in experiment.

The small number of modes in the system can lead to observable beatings of the system's eigenstates in our two-dimensional spatial scans. A prerequisite for the occurrence of such beating effects is that more than one mode is excited in the first place. In our experiment this condition is fulfilled, because we use a spatially confined source radiating in all directions in close proximity to the sample. Alternatively, defects or scattering particles inside the structure provide a different method for exciting modes with different k-vectors.

Figure 3.8(a) shows a clear example of beating behavior of the wave intensity in experiment. The image of the scan has been rotated by 90 degrees with respect to the spatial scans shown in Fig. 3.4. A decomposition into the system eigenstates for this particular sample reveals just two eigenstates contribute significantly to the wave function as shown in Fig. 3.8(c). Using only these two eigenstates and their corresponding eigenvalues, we

calculated the z-development of the wave function in Fig. 3.8(b). To compare experiment with theory, the center of mass was calculated for all z-positions as shown in Fig. 3.8(d). The calculated oscillations are quantitatively similar to those observed in experiment.

In general, the number of significantly contributing eigenvectors is often higher than two, which makes the beatings less visible. Yet, the anti-diagonal patterns shown in Fig. 3.6(a) and (b) are another observable consequence of the beating between the system's eigenstates. Depending on the accumulated phase during propagation, these anti-diagonal excitation-detection patterns can in fact become circular or diagonal as shown in Fig. 3.6(c-e). The patterns are to a large extent point-symmetric which originates from a flip in sign of the expansion coefficients when the excitation antenna crosses the central position of the beating oscillation.

3.5   Conclusion and discussion

We have measured how electromagnetic wave functions develop over time in localizing samples by carrying out a (1+1)D transverse localization experiment. Because of the limited number of modes in our system, excitation by a source in the near-field can be described as a superposition of a few of the system's eigenstates. The different eigenvalues and simultaneous excitation of these eigenstates lead to observable beatings in wave functions.

Out-of-plane scattering was used as an experimental analog of energy dissipation. The ensemble averaged extent of the wave profiles is in quantitative agreement with calculations from a numerical solution to a Schrödinger type of equation. By introducing homogeneous dissipation into this model, we deduce that dissipation is of no influence to the occurrence of transverse localization except for an exponential attenuation.

Since the transverse localization scheme allows for measuring snapshots of wave functions in time, it is a very convenient tool for studying the effect of different forms of disorder on wave propagation as put forward by recent work on photonic quasicrystals [126, 139]. Our work on transverse localization and dissipation suggests that transverse localization can also be an excellent platform for studying the influence of perturbations and partial incoherence on localization [140]. Transverse localization experiments require samples to be ordered in one dimension. Introducing scatterers at random positions inside the sample might reveal how strict the condition of a well aligned system is in experiment. A single scatterer excites modes with widely varying k-vectors probably leading to beating effects even in the case of plane wave excitation. It would be interesting to study when a description in terms of eigenstates of the transverse localization Hamiltonian breaks down.

CHAPTER 4

Spatial threshold in amplifying random media

In this chapter the transport and generation of light in multiple scattering media with optical gain is studied both experimentally and numerically. By imaging the spatial distribution of light escaping from the side of the sample, the propagation depth is analyzed. Far below and far above random laser threshold the spatial profile of emission light is independent on pump intensity, while around threshold the spatial distribution of emission light changes profoundly. The experimental results are explained by interpreting the numerical solutions to a set of coupled time-dependent diffusion equations on a non-uniform spatial grid. Our studies provide a new and easily accessible method for observing the random laser threshold.

4.1 Transport of light inside random media

Understanding the transport of light inside multiple scattering media is of paramount importance for both life scientists [141] and physicists [64]. Recently, the study of light sources inside disordered media has attracted much interest [33, 51]. In the previous chapter, the propagation of radiation in transverse localizing samples originating from a source in the near-field was studied. We now focus on the propagation of light in amplifying random media where sources generate light by both spontaneous and stimulated emission.

The majority of experimental random laser studies have focussed on spectral analysis [92, 93, 142]. The spatial distribution of random laser light inside the scattering medium is largely uncharted territory. Understanding the propagation of light in amplifying random media is of relevance, since it determines the number of modes involved in the lasing process and the distribution of gain inside the medium. New side imaging techniques enabled the determination of important transport parameters in passive random media, such as the transport mean free path and the extrapolation length [143], and were essential in explaining the directionality of lasing in weakly scattering active media [88]. The extrapolation length is an important parameter in diffusion studies. This parameter depends on the reflectivity
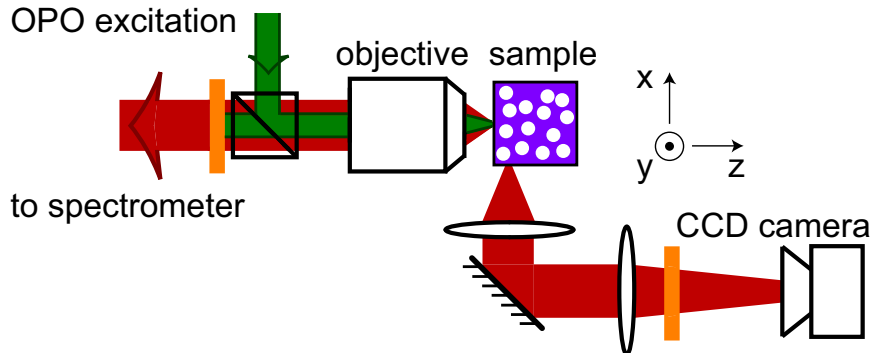
Figure 4.1: Schematic top-view of the experimental apparatus. Green: pump beam. Red: emission light. The orange bars represent color filters.

at the boundaries of a diffusive sample and indicates at what distance outside the sample the extrapolated diffusive intensity becomes zero.

In this chapter, we exploit these new techniques to study the effect of gain on the spatial profile of emission light inside scattering samples. The experimental methods are presented in Sec. 4.2. In Sec. 4.3, the extrapolation length and the transport mean free path of the sample are determined. The spatial profile of emission light is studied as function of pump power. A remarkable expansion in emission volume is observed around the threshold. The spatial distribution of emission light in a random laser is described by a set of diffusion equations. In Sec. 4.4, we explain how this set can be solved in three dimensions using cylindrical coordinates. The results of the numerical calculation and the experiment are compared in Sec. 4.5. The experiments are shown to be in qualitative agreement with diffusion theory. The implications of our studies on other work in random lasers is discussed in Sec. 4.6. We note beforehand that some constants in this chapter slightly deviate from the ones in Ref. [144] due to the accumulation of knowledge over the years. These differences have however no effect on the conclusions of our work.

4.2   Experimental methods

In Fig. 6.2 the experimental apparatus is schematically shown. Excitation light generated by an optical parametric oscillator (Opolette, 20 Hz, 5 ns, $\lambda = 563$ nm) is focused onto the sample by a microscope objective (Leitz, 0.25 NA). By slightly defocusing the sample the pump spot size could be controlled. The emission collected in reflection is spectrally analyzed using a spectrograph (Oriel MS-257, resolution 0.5 nm) connected to an EMCCD camera (Hamamatsu, C-9100). The emission in reflection was also used to determine the diffuse fluorescence Full-Width at Half-Maximum diameter by imaging the diffuse spot on a CCD camera.

We extended the conventional random laser setup with the sample side imaging technique shown by the lower arm in Fig. 6.2. An aspherical lens ($F/\# = 1.5$) collects the light exiting the sample from the side and another lens images the sample surface onto a CCD camera (Mightex or AVT Pike). Color filters were used in both detection paths to remove excitation wavelengths. The sample was placed on a translation stage in order to control the distance between the focus spot and the edge of the sample. The aspherical lens was also placed on a translation stage to ensure the sample surface remained in focus on the CCD camera. Figure 4.2(a) shows a typical CCD image obtained from the side
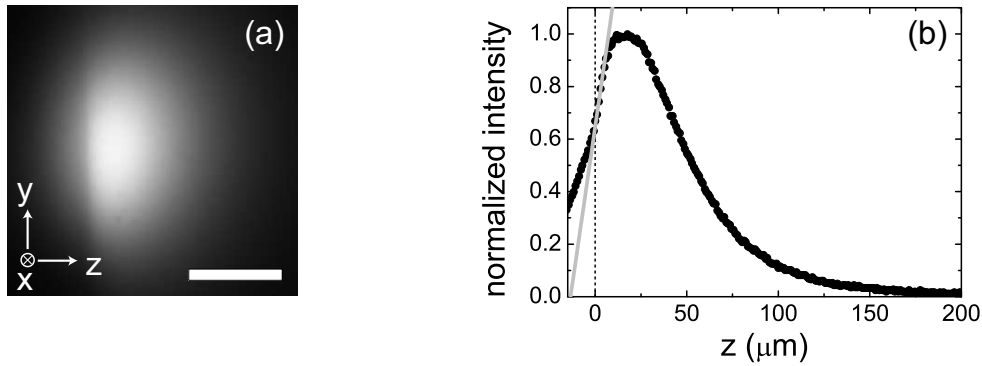
Figure 4.2: (a) CCD-image of emission from the side of the cuvette below random laser threshold. The scale bar denotes 100 μm. (b) cut along the z-axis through the middle of the diffusive spot normalized to the peak value. Black dashed line: cuvette boundary. Gray line: linear fit to the data points around $z = 0$. The interception of the fit with the line $z = 0$ gives the extrapolation length.

of a sample. At the edge of the sample the intensity drops, although a hue of the diffuse intensity remains visible. During experiments care was taken that the CCD camera did not saturate by placing neutral density filters in front of the camera and by adjusting the exposure time.

Samples were fabricated by suspending TiO_2 particles (R900, DuPont, median particle size 410 nm according to specifications, volume fraction 1%) in an acidic solution of 1 mM Rhodamine 640 P in methanol. The experimental cell was a quartz cuvette (Hellma, inner size 10×10×45 mm, wall thickness 2.5 mm). Experiments were performed within one hour after treatment in an ultrasonic bath before significant sedimentation of TiO_2 particles occurred.

The side images of the diffusive samples allow us to analyze the sample's extrapolation length. Figure 4.2(b) shows a cut along the z-axis through the middle of the diffusive spot displayed in Fig. 4.2(a). The intensity profile shows a kink at the boundary of the sample. We determine the extrapolation length z_e of the sample by first fitting the first five data points for $z > 0$ with a line. The interception of this line with $z = 0$ then returns the extrapolation length $z_e = 13.5 \pm 2$ μm.

The relationship between the extrapolation length and the transport mean free path is determined by the internal reflection coefficients at the boundaries of the sample. In the case of glass cuvettes, both the reflection at the sample-glass and the glass-air interface need to be taken into account. This second interface causes a relatively large extrapolation ratio z_e/ℓ of 1.77 [145]. From this ratio, we deduce that $\ell = 7.6$ μm ± 1 μm. Enhanced backscattering experiments [59] were also performed on the sample. The width of the cone provides us with an alternative way of determining the mean free path. We find $\ell = 6.0$ μm at $\lambda = 610$ nm with an estimated error of 3 μm, which is mostly due to a reduced value for the enhancement factor [146]. These two values are also comparable with extrapolated values found in the literature ($\ell = 8.3 \pm 1.3$ μm) [147], where we note that the size of the R900 titania particles was reported to be different from the manufacturer values [147, 148]. We conclude that the transport mean free path is at least an order of magnitude shorter than the system length and the absorption length of the gain medium. The sample is thus clearly in the multiple scattering regime.

4.3   Experimental results and analysis
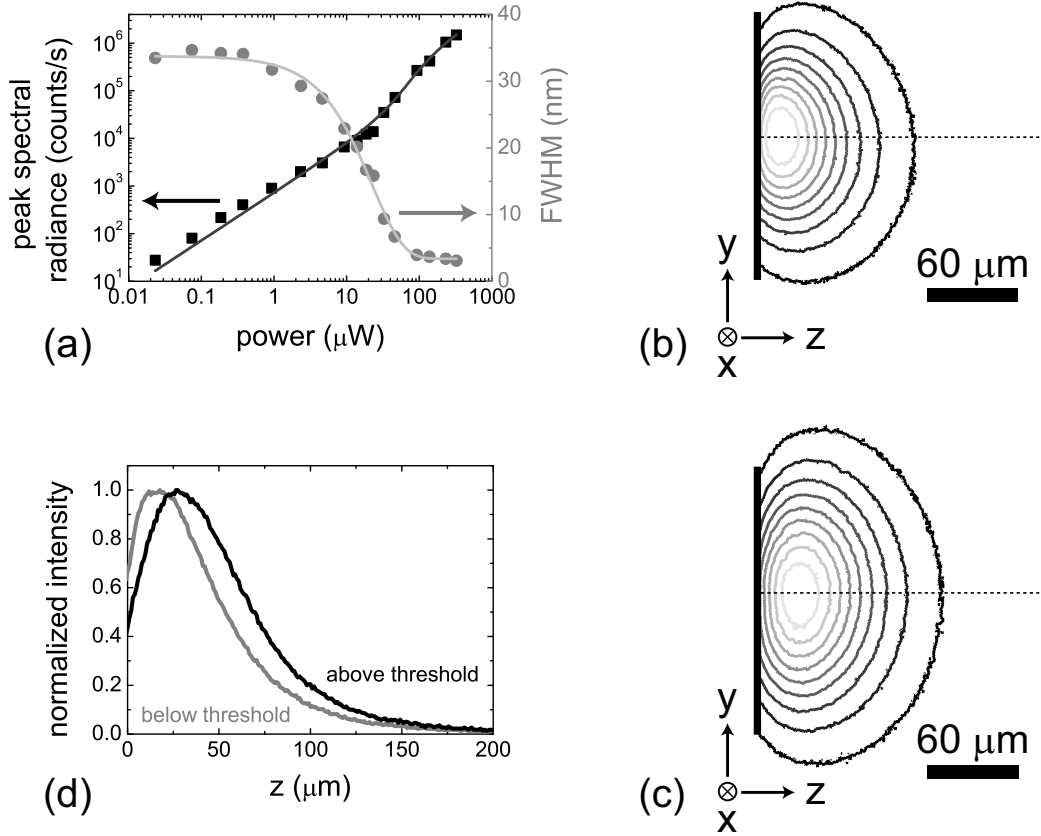
Figure 4.3: (a) the peak spectral radiance (left axis, black squares) and the FWHM of the spectrum (right axis, gray dots) versus the pump power on a loglog and a semilog scale respectively. The dark gray line is a fit of the peak spectral radiance with the rate equations. The light gray solid line is a sigmoidal fit to the FWHM of the spectrum and serves as a guide to the eye. (b) Contour plot of the spatial distribution of emission light below threshold (0.2 μW). The contour interval is 0.1 times the maximum value in the plot. (c) Contour plot of the spatial distribution of emission light above threshold (140 μW). The contour interval is 0.1 times the maximum value in the plot. (d) Cuts along the z-axis through the center of the contour plots below (gray line) and above threshold (black line).

The photoluminescent emission spectrum centered around 610 nm was measured for various values of the pump fluence. Figure 4.3(a) show the peak spectral radiance and the width of the output spectrum versus the averaged pump power. A fit of the peak spectral radiance with the rate equations discussed in Sec. 2.3 returns a narrowing factor of 0.13. This value is larger than the one found in Sec. 2.3. The difference is caused by the fact that in this chapter the spectra below threshold are narrower ($\sim$ 10 nm) due to excitation with a smaller pump spot. Such a smaller pump spot reduces the effect of reabsorption and thereby spectral broadening [89]. The peak spectral radiance and the spectral width show a clear threshold around 20 μW.

The side imaging technique makes it possible to study the propagation of light in active random media directly. The spatial profile of the random laser emission exiting the medium from the side was monitored for all values of the pump fluence. When the focus of the pump
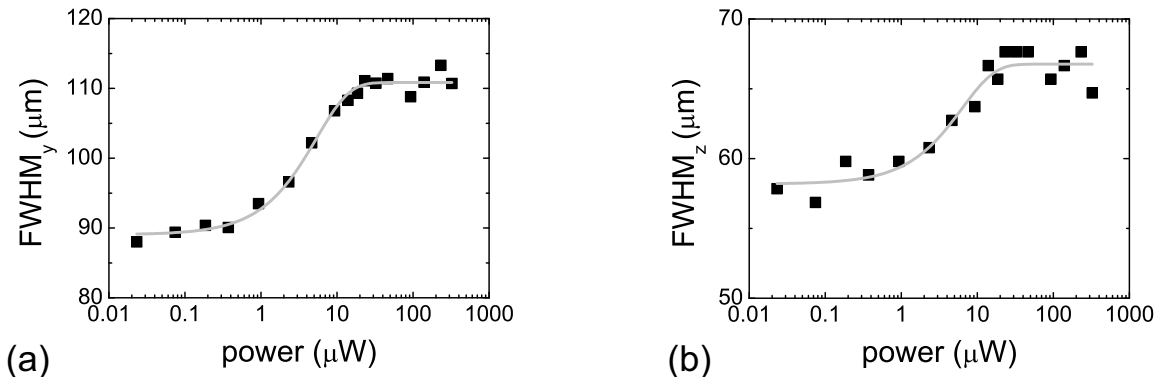
Figure 4.4: (a) Width of the diffusive side image along the y-direction versus pump power. The line is a guide to the eye. (b) Width of the diffusive side image along the z-direction versus pump power. The line is a guide to the eye.

is brought in close proximity to the edge of the sample (at half the FWHM of the diffuse fluorescent spot, $\sim$30 µm) the spatial distribution of emission light exiting the random laser from the side changes around the threshold. Figure 4.3(b) and (c) show contour plots of the spatial profile below (0.2 µW) and above threshold (140 µW). Compared to the below threshold spatial profile, the above threshold profile of the emission light is expanded in both y- and z-direction. The cuts along the z-axis through the center of the diffusive side image in Fig. 4.3(d) clearly show that the maximum of the emission profile lies deeper within the sample above threshold.

We made sure that the observed changes around threshold are not due to possible sedimentation effects by minimizing the time between the experiments. For larger distances between the spot and the edge of the sample the spatial distribution remains unaltered for all pump fluences, which is another clear indication that the passive transport properties of the sample remain constant during experiment. Moreover, once the random laser is pumped above threshold increasing the pump rate has no effect on the distribution of emission light. In Fig. 4.4, the widths of the diffusion profile along the y-and z-direction are shown as a function of pump power. For the y-direction these widths were obtained after fitting the profile with a Gaussian. For the z-direction such a straightforward fitting procedure is not possible due to the presence of the boundary and the asymmetric lineshape. Therefore the widths along the z-direction were determined by hand after extrapolating the data. The graphs demonstrate that around the random lasing threshold the diffusive volume expands, whereas far below and far above threshold the volume remains the same. The largest changes occur between 1 and 10 µW, that is at the beginning of the threshold region according to Fig. 4.3(a).

4.4   Diffusion theory with gain

In *chapter 2*, a space independent rate equation model was used to describe the input-output characteristics of a random laser. To understand the spatial distribution of light inside a random laser such an approach does not suffice.

To explain the experimental results of this chapter, we need to model transport of light with diffusion equations in which gain and absorption are incorporated. Instead of phrasing the equations in terms of number of photons q in the laser mode and the number

of molecules N in the upper laser level, the local energy and population *densities* need to be considered [89, 149]. The three equations that describe the diffusion of laser photon density[1], $W_q(\mathbf{r}, t)$, pump photon density, $W_p(\mathbf{r}, t)$, and the density of molecules in the upper laser level, $n_1(\mathbf{r}, t)$, are:

$$\frac{\partial W_q}{\partial t} = D\nabla^2 W_q + (\sigma_e c n_1 - \sigma_r c n_0) W_q + \frac{\beta}{\tau} n_1, \tag{4.1}$$

$$\frac{\partial W_p}{\partial t} = D\nabla^2 W_p - \sigma_a c n_0 W_p + \frac{1}{\ell} I_{\text{in}}, \tag{4.2}$$

$$\frac{\partial n_1}{\partial t} = \sigma_a c n_0 W_p - (\sigma_e c n_1 - \sigma_r c n_0) W_q - \frac{1}{\tau} n_1. \tag{4.3}$$

Here D is the diffusion constant, σ_e, σ_r, and σ_a are the emission, reabsorption, and absorption cross-section of the dye molecules, τ is the spontaneous emission lifetime, and n_0 is the density of molecules in the ground state. The source term for the pump light, $\ell^{-1} I_{\text{in}}(r, z, t)$, is a pulse with width τ_p and decays exponentially in z with an extinction length $\ell_{\text{ext}}^{-1} = \ell_a^{-1} + \ell^{-1}$ (with ℓ_a the absorption length). Here $I_{\text{in}}(r, z = 0, t)$ is the local and instantaneous intensity, which refers to the number of pump photons per unit area per unit time incident at position $(r, z = 0)$. In our system scattering is responsible for most of the extinction ($\ell \ll \ell_a$) and hence the source term is treated as power independent.

Comparing the diffusive rate Eqs. (4.1)-(4.3) with the single mode cavity rate Eqs. (1.20)-(1.21), identifies several important differences. First, the Laplacian $D\nabla^2$ takes the role of the cavity decay rate γ_c. This replacement illustrates that the local "loss" of energy density in a random laser is due to diffusive transport. Second, the spontaneous emission factor β is not part of the stimulated emission term. Instead, the stimulated emission cross section appears. The appearance of this factor is caused by the fact that the stimulated emission rate has to be replaced by the stimulated emission rate per unit energy density [89]. In essence, the cross section represents the Einstein B coefficient, which is proportional to the Einstein A coefficient by the inverse of the LDOS [16, 150]. Third, in the diffusive random laser the pump rate $\sigma_a c n_0 W_p$ is not a constant but varies locally and its spatial distribution is also given by a diffusion equation. Fourth, reabsorption of emission light is explicitly included. Although the reabsorption cross section is typically two orders of magnitude smaller than the stimulated emission cross section at the random laser output frequency, it does influence the propagation of emission light inside the sample. Despite these significant differences, the effective cavity approach and this diffusive approach have one important point in common. They both split up the spectrum in a lasing and a non-lasing part by use of the effective spontaneous emission factor. In *chapter 5* the spectral shape of random lasers receives more attention.

4.4.1 Numerical solution to diffusive random laser equations

To solve the set of diffusive laser rate equations, the method of lines is used. In this method a partial differential equation is converted into a set of ordinary differential equations (ODE's) in time by introducing a spatial grid and by approximating the spatial derivative at every grid point with finite differences. Below threshold a steady state solution can be found by matrix inversion, where the non-diagonal matrix elements are due to the finite difference approximation of the spatial derivatives and the energy and population densities are vectors.

---

[1]For convenience the energy densities at frequency ω are normalized to the energy of one photon $\hbar\omega$.

Around threshold this method method breaks down, because the matrix to be inverted becomes singular [89].

The set of equations thus has to be solved numerically. For that purpose, we use the ode15s function from MatLab's extensive ODE library, which is particularly suited for solving stiff ODE's [137]. The experimental configuration is obviously threedimensional. Unfortunately, the required computational power increases substantially for every added dimension. To be able to perform our calculations on a reasonable timescale (order of hours), we reduce the number of dimensions in our system by using cylindrical coordinates and impose rotational symmetry. As a consequence the boundary in the yz-plane close to the center of the diffusive spot is ignored.

Moreover, the cylindrical grid is made non-uniform to allow the calculation of a relatively large system in two dimensions and at the same time have detailed spatial information close to the origin. Defining $h_+ \equiv x_{i+1} - x_i$ and $h_- \equiv x_i - x_{i-1}$, the finite difference form of the first and second derivative read [151]

$$\frac{\partial f}{\partial x} \rightarrow \frac{f(x + h_+) - f(x - h_-)}{h_+ + h_-}, \tag{4.4}$$

$$\frac{\partial^2 f}{\partial x^2} \rightarrow \frac{h_- f(x + h_+) - (h_+ + h_-)f(x) + h_+ f(x - h_-)}{0.5 h_+ h_- (h_+ + h_-)}. \tag{4.5}$$

The well-known equations for central differences are retrieved when $h_+ = h_- = h$. In cylindrical coordinates with rotational symmetry the Laplacians in Eqs. (4.1) and (4.2) become

$$\nabla^2 W = \frac{\partial^2 W}{\partial z^2} + \frac{\partial^2 W}{\partial r^2} + \frac{1}{r}\frac{\partial W}{\partial r}. \tag{4.6}$$

Due to the factor $1/r$ in the third term and the boundary condition $\frac{\partial W}{\partial r}\big|_{r=0} = 0$, the equation for the Laplacian becomes indeterminant at $r = 0$. To circumvent this problem we invoke l'Hôpital's rule [137] to rewrite

$$\lim_{r \to 0} \frac{1}{r}\frac{\partial W}{\partial r} = \frac{\partial^2 W}{\partial r^2}. \tag{4.7}$$

Besides the $1/r$ factor, the analysis around $r = 0$ is further complicated by the fact that central differences cannot be applied because $r \geq 0$ by definition. However, since at $r = 0$ the derivative of any quantity vanishes in the absence of δ-functions, the central difference equation for the first derivative shows that $f(x + h) = f(x - h)$. Where we have used a uniform step size. Central difference formula (4.5) for the second derivative can then be written as

$$\frac{\partial^2 W}{\partial r^2}\bigg|_{r=0} = 2\frac{W(h) - W(0)}{h^2}. \tag{4.8}$$

To solve the set of ODE's, boundary conditions need to be implemented. The two differential equations describing the laser light and the pump light, Eqs. (4.1) and (4.2), obey mixed boundary conditions. The photon densities are assumed zero at a characteristic length scale, the extrapolation length, outside the sample. The equation describing the population of the upper laser level obeys a Dirichlet boundary condition, which means n_1 and n_0 are both zero outside the sample.

The sample is modeled as a cylinder with dimensions $r = 150\ell$ and $z = 150\ell$. Both the r and the z axis are divided into a coarse and a fine interval which results in a rz-grid
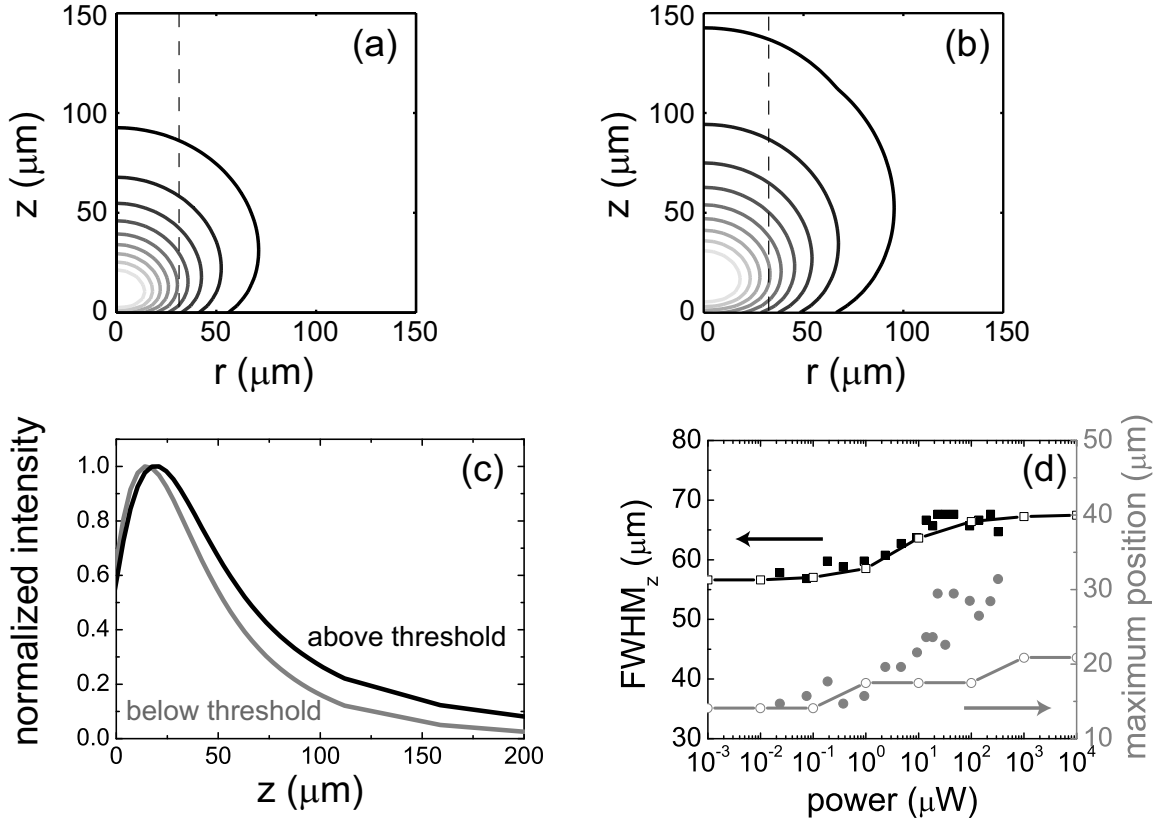
Figure 4.5: (a) Time-integrated contour plot of the emission intensity below threshold ($P = 10^{-3}$ µW). The contour interval is 0.1 times the maximum value ($18{\cdot}10^{-4}$) in the plot. (b) Time-integrated contour plot of the emission intensity above threshold ($P = 10^3$ µW). The contour interval is 0.1 times the maximum value ($18{\cdot}10^3$) in the plot. (c) Cuts along the dashed lines in (a) and (b). (d) theoretical and experimental characteristics of the spatial profiles along the dashed lines in (a) and (b) versus pump power. Black open squares ($\square$): the numerically calculated values of the FWHM of the cut of the spatial distribution of laser light. Black closed squares ($\blacksquare$): experimentally determined values from the profile cut. Gray open disks ($\circ$): numerically determined position of the laser light maximum in depth. Gray closed disks ($\bullet$): the experimentally determined values.

that is divided into four segments. In the calculation all spatial parameters were scaled to the transport mean free path and the dynamical parameters to ℓ^2/D. The time taken into consideration spans 40 ns. Realistic experimental situations ($\ell = 7$ µm, $z_e = 14$ µm, $\rho = n_1 + n_0 = 6 \cdot 10^{23}$ m^{-3}, $\sigma_a = 3.7 \cdot 10^{-20}$ m^2, $\sigma_r = 0.058 \cdot 10^{-20}$ m^2, $\sigma_e = 3.8 \cdot 10^{-20}$ m^2, $\beta = 0.07$, $\tau_p = 5$ ns, $\tau = 4$ ns, $r = 15$ µm) were calculated on a 40×50×57 ($t \times r \times z$) grid. Using slightly different parameters did not significantly change the outcome of the numerical calculation. The calculation was performed on an Intel 2.67 GHz Quad processor with 4.00 GB of RAM with Windows XP 64-bit as an operating system. Below threshold, the computation time is approximately 10 minutes. For pump powers around and above the threshold the computation time increases to several hours.

4.5 Numerical results and analysis

In Fig. 4.5(a) and (b) contour plots of the numerically determined time integrated diffusive emission photon density profile in the rz-plane below and above threshold are shown. The
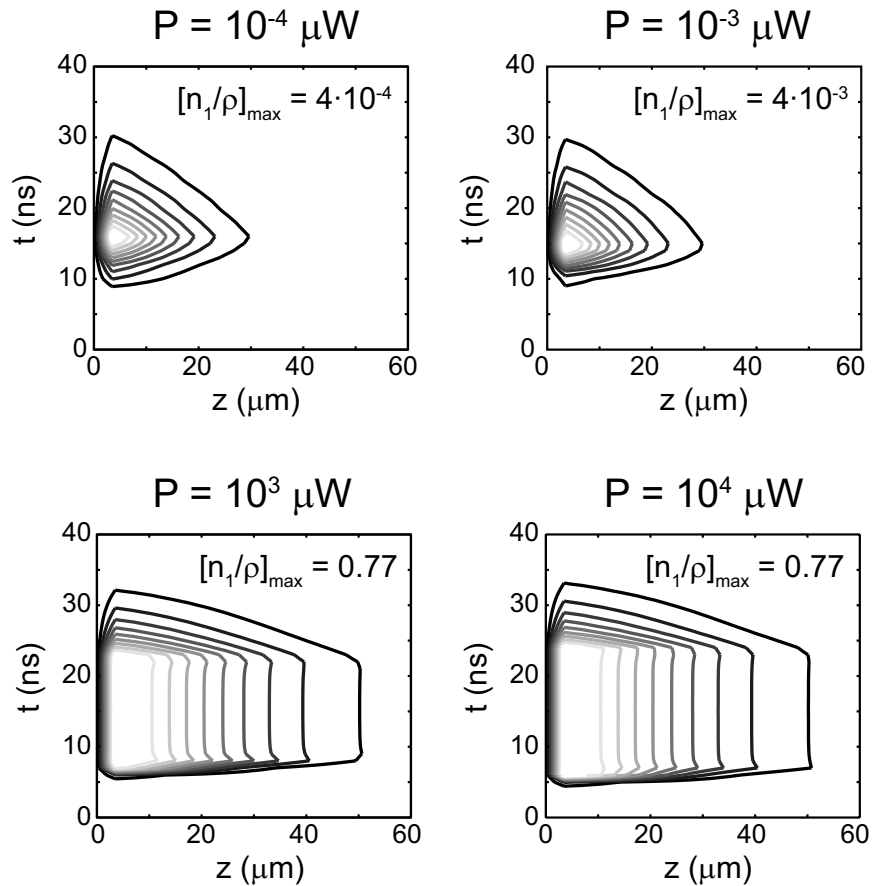
Figure 4.6: Calculated contours of the excited state profile in the zt-plane at $r = 0$ for different pump powers far below and far above threshold. The contour interval is 0.1 times the maximum value in the plot. Below threshold (the two upper graphs) an increased pump rate results in more spontaneous emission events, but does not lead to a change in population profile. Above threshold (the two lower graphs) stimulated emission has become the main mechanism of radiation. The maximum value for the population inversion is determined by the diffusive loss close to the boundary.

profile above threshold is expanded compared to the profile below threshold. In order to compare experiment and theory, we analyze cuts from the numerical data at $r = 34$ μm in the rz-plane. Two of these cuts are shown in Fig. 4.5(c). The cuts show that the trends in the numerical data match the trends in experiment. The values for z at which the intensity profile reaches its maximum and the width of the intensity profile are plotted versus the pump power for both the numerical calculation and the experiment in Fig. 4.5(d). In agreement with experimental observations the spatial width of the laser light profile increases around threshold, but remains constant far above threshold. The inclusion of reabsorption is important in order to make the results agree quantitatively with experiment.

To understand why the spatial profile is fixed far below and far above threshold, we analyze the contribution of spontaneous and stimulated emission to the total emission in time. Figure 4.6 shows calculated contours of the population of the upper laser level for pump powers below and above threshold in the zt-plane at $r = 0$ μm. Far below threshold, the origin of the emitted light is spontaneous emission. In this regime, the set of equations is linear: an increase in the pump fluence simply leads to more spontaneous emission events

everywhere in the sample, but does not change the normalized spatio-temporal profile of the population.

Above threshold, stimulated emission is responsible for most ($> 99\%$ for $P/P_{\text{th}} > 1$, where P_{th} is the pump power threshold) of the light emitted by the dye molecules. Gain compensates for the losses in the system, but the gain can never, except for temporal fluctuations, exceed the losses. The main losses in a random laser are due to the diffusive loss term, $\nabla^2 W_q$, which is only non-zero close to the origin. As a consequence, the gain length in a random laser is strongly spatially dependent. Once above threshold, the stronger the system is pumped, the deeper inside the sample reabsorption losses are compensated for. The cancelation of reabsorption hardly changes the diffusive laser light profile, since the required gain is small compared to the gain needed to compensate the diffusive losses. Analogous to conventional laser systems the gain saturates above threshold [15]: the maximum density of excited molecules, n_1/ρ, is fixed for all pump powers above threshold.

The numerical calculation succeeds in explaining the main experimental features. Yet Fig. 4.5(d) shows that the changes in the numerical data are smaller than in the experiment. We attribute these differences to the main limitation in our model: the system is modeled in cylindrical coordinates, whereas in experiment the sample configuration is not radially symmetric. An extra loss factor that is induced by the presence of the boundary from which light escapes at the side of the sample, is thus not taken into account. Taking all boundaries into account properly would imply a three-dimensional model, which is computationally intensive.

4.6   Conclusion and discussion

In conclusion, we have introduced a new approach for studying the transport and generation of light originating from light sources inside a multiple scattering medium. Our side imaging method is a novel experimental way to determine and study the random laser threshold. Around the random lasing threshold, the spatial distribution of emission light expands. Far below threshold, each pump photon increases the number of excited molecules following a pump power independent spatial profile. Far above threshold, each pump photon eventually results in a stimulated emission event following again a pump power independent spatial profile. Our analysis emphasizes that the gain length in a diffusive system is a spatially dependent variable [152]. Moreover, above threshold the minimal gain length is determined by the diffusive loss inside the system and is not easily tuned by the excitation power. Our observations relate to random laser systems in which spectral spikes are observed. The expansion of the lasing volume rather than a decrease in gain length is an important factor not yet taken into account for explaining the observation of increasing number of spikes with increasing pump power [85]. In the next chapter, a direct consequence of the expansion in emission volume becomes evident.

Tuning random lasers by engineered absorption

Spectral control over the emission wavelength of a random laser is the central theme of this chapter. For that purpose the amount of absorption at the emission frequency is adjusted. Experimentally, the system consists of elastic scatterers in a high quantum efficiency gain medium to which a non-fluorescent dye is added. This non-fluorescent dye shifts the net gain curve and thereby the emission peak of the random laser. Competition effects are observed and explained. Our results are interpreted by a model that describes the spectral response of the system as a function of the effective cavity decay time and (re)absorption processes.

5.1 Emission wavelength of a random laser

So far our treatment on random lasers has relied on the use of an effective β-factor for describing both the input-output response in *chapter 2* and the distribution of diffuse emission light in *chapter 4*. Although such an approach proved to be very powerful, it is ill-suited for describing the frequency output of a random laser. This frequency output is precisely what interests us in this chapter as we seek control over the emission wavelength of a random laser.

Analogous to conventional lasers, the frequency at which an amplifying random media starts to lase is determined by the net balance between gain and loss. Better control over these emission properties of a random laser has been a central issue in the field [142, 153–155]. The diffusive laser rate Eqs. (4.1)-(4.3) show that the loss term is governed by a combination of diffusive losses and reabsorption losses, whereas the gain term is simply determined by the stimulated emission cross section of the gain medium. This decomposition of the rate equations suggests three routes for manipulating the output wavelength of a random laser: (1) by making the diffusive loss term spectrally dependent, (2) by changing the frequency dependence of the reabsorption term, or (3) by changing the spectral shape of the gain curve. The last suggestion can be accomplished in a trivial manner by simply

changing the gain medium altogether as shown in, *e.g.*, Fig. 2.3.

In a convincing series of recent experiments, Gottardo *et al.* [156] have shown that Mie resonances of the individual scatterers can shift the peak wavelength of a random laser by a few line widths. These Mie resonances introduce a wavelength dependent diffusion constant. The diffusive loss term thereby becomes spectrally dependent as well, leading to a spectral shift in the net gain curve. By creating a random laser out of liquid crystal scatterers, Wiersma and Cavalieri [153] were able to switch off a random laser by increasing the temperature. Again, this control is due to a change over the diffusive properties of the sample.

5.1.1   Exploiting absorption

Surprisingly, the much easier alternative of controlling the amount of absorption at the emission wavelength has never been used to tailor intrinsically disordered lasers. Perhaps absorption has been overlooked, because it is generally regarded as unwanted in the optics community. Absorption shares with scattering of light that it is detrimental to most optical devices, since both processes lead to extinction of an incident light beam [28]. Absorption is therefore preferably minimized, for instance in the field of surface plasmon polaritons [157, 158] and in the field of random media [66, 67, 159]. A notable exception is the field of photovoltaics [160], where small percentages of increased absorption of sunlight can mark significant progress. As we discussed in introductory Sec. 1.2, disordered scattering media are currently being exploited to overcome fundamental limits of conventional optics [33, 37, 161]. These experimental studies emphasize that scattering is transforming from an annoyance into a tool. Similarly, absorption received more attention recently as it enables the detection of single non-fluorescent molecules at room temperature [162–165] and forms the basis of the anti-laser [166, 167].

Optically pumped random lasers [92, 93, 142, 168] rely on absorption for creating a population inversion. The gain curve of the emission molecules is the main mode selection mechanism in a random laser [107, 169] as we have also extensively discussed in *chapter 2*. Above threshold most light is emitted close to the maximum of the gain curve. Reabsorption, however, slightly shifts the emission to the red of the gain curve maximum. In this chapter, additional absorption is introduced as a means of controlling the output wavelength. First, the sample fabrication is discussed in Sec. 5.2. The shift in emission frequency is demonstrated experimentally in Sec. 5.3 and then analyzed in Sec. 5.4.

5.2   Samples

Random laser samples were fabricated using a Rhodamine 640 P (Rh640) solution in methanol as a gain medium and titania particles (R900, Du Pont, 1% vol.) as elastic scatterers. We added different quantities of Quinaldine Blue (Qblue), a non-fluorescent dye (quantum efficiency 0.1% [170]), in methanol to control the random laser emission with absorption. The absorption and emission spectrum of both a 5 μM solution of Rh640 and Qblue in methanol were measured using a UV-VIS spectrophotometer and a 535 nm pulsed optical parametric oscillator (Opolette, 20 Hz, 5 ns, 535 nm) respectively. These absorption and emission spectra are shown in Fig. 5.1. The emission cross section was calculated using $\sigma_e(\lambda) = \frac{\lambda^4 L(\lambda)}{8\pi c \tau \eta^2}$. Here $\int L(\lambda) d\lambda = \phi$ where ϕ is the quantum efficiency and η is the effective refractive index. We assumed a radiative lifetime of 4 ns in solution [77] and a quantum
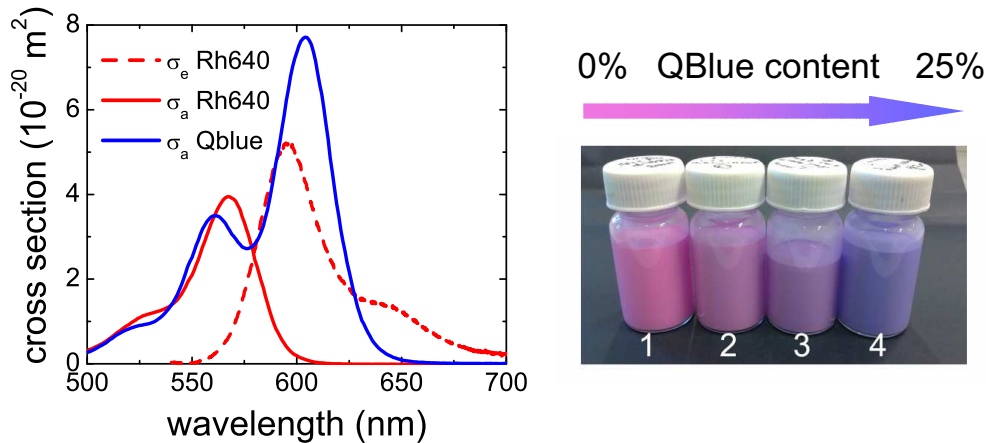
Figure 5.1: (left) Absorption (red line) and emission (red dashed line) spectra of Rhodamine 640 P and absorption spectrum of Quinaldine Blue (blue line) dissolved in methanol. (right) Photographs of samples 1-4 containing varying percentages of the absorber dye Quinaldine Blue.

efficiency of 1 for Rhodamine 640 P as determined in *chapter 2* [169]. The maximum absorption cross section of Qblue lies around the maximum emission cross section of Rh640, which makes Qblue very suited for engineering a Rh640 random laser. Moreover, Qblue has a stimulated emission cross section that is $\sim 100\times$ smaller than the emission cross section of Rh640. Therefore we can attribute all emission in the random laser experiments directly to emission originating from Rh640 molecules. We prepared four samples by combining a 1 mM solution of Rh640 with a 1 mM solution of Qblue such that $n_{\text{Rh640}} + n_{\text{Qblue}} = 1$ mM: sample 1 (100% Rh640), sample 2 (96% Rh640 and 4% Qblue), sample 3 (90% Rh640 and 10% Qblue), and sample 4 (75% Rh640 and 25% Qblue). A photograph of these samples is shown in Fig. 5.1. The samples become more blue when adding more Qblue, since Qblue absorbs most of the red part of the spectrum. A fifth sample was made by adding Qblue in crystalline form to a 1 mM solution of Rh640 (molar ratio QBlue/Rh640 = 0.4). To prevent aggregation and sedimentation of titania particles all samples were treated in an ultrasonic bath before measurement.

The experimental setup used was similar to the one in *chapter 2*. Excitation light generated by the optical parametric oscillator was focused onto the samples by a lens (f = 5 cm). The size of the fluorescent spot could be varied by moving the sample in and out of the focal plane. The same lens collected the emission which was then spectrally analyzed using a spectrograph (Oriel MS-257) connected to an EMCCD camera (Hamamatsu, C-9100).

5.3   Experimental results

For all random laser samples, the emission spectrum was monitored for different values of the pump fluences. Above a certain pump value, the threshold, the emission spectrum narrows. We analyze the wavelength of the peak of the emission spectrum for the different samples. In Fig. 5.2(a) the spectra above threshold are plotted for the samples 1-4. The peak wavelength for a pure Rh640 random laser lies at 607 nm and shifts gradually to the blue when more Qblue molecules are added. When the ratio between Rh640 and Qblue molecules lies around 10:1 (sample 3), the peak is already shifted by about 2 line widths to 598 nm.

The spectrum of sample 4 is shifted by 14 nm compared to sample 1, which corresponds
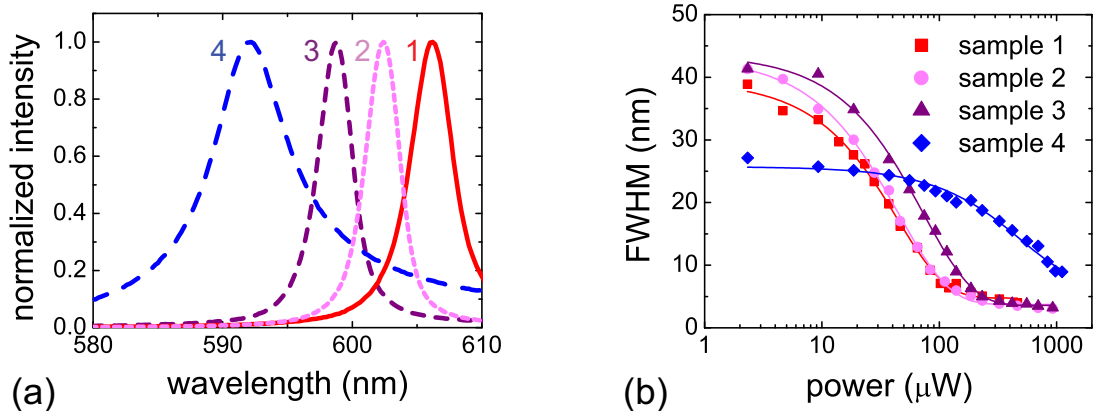
Figure 5.2: (a) emission spectrum above threshold for random laser samples 1-4. Pump powers: 465 μW for sample 1, 930 μW for sample 2 and 3, and 1114 μW for sample 4. (b) Width of the spectrum versus pump power for random laser samples 1-4.

to 3-4 line widths. The spectra of sample 1, 2, and 3 are significantly narrower than the spectrum of sample 4. To understand why the spectrum of sample 4 is relatively broad, it is insightful to plot the width of the spectra versus pump power as shown in Fig. 5.2(b). The widths were determined by the FWHM of the raw spectra, except for the first nine data points of sample 4 where two Lorentzians were fitted from the data from which the width was extracted. This fitting procedure was applied because these nine spectra consisted of two overlapping peaks. From this figure, we conclude that the threshold increases when the density of absorbers becomes larger. Sample 4, having the largest concentration of absorbers, has such a high threshold that the width is not yet converged to the far above threshold value at the maximum available input fluence.

5.3.1 Mode competition

When the concentration of the absorber is further increased, the random laser responses strikingly different. In Fig. 5.3(a), the normalized spectra below and above threshold are plotted for sample 5. Below threshold, two peaks can be observed in the emission spectrum: one around 590 nm and another lower one around 650 nm. For higher pump powers around the threshold, this situation is reversed: the peak at 650 nm dominates over the peak at 590 nm. Figure 5.3(b) shows the peak spectral radiance for the two peaks versus excitation power. The pump power was increased monotonically to avoid irreversible artifacts. The ratio of the two peaks (peak at 590 nm/ peak at 650 nm) first increases with increasing pump power and then drops dramatically far above threshold. While the pump power increases, the peak emission wavelength changes significantly as shown in Fig. 5.3(c). The peak at the blue side of the spectrum shows a blue shift of 3 nm, whereas the peak at the red side of the spectrum shows a red shift of 9 nm.

5.4 Model

To describe and understand our experimental findings, we present an analytical expression for the peak wavelength of the random laser. In principle, for a constant mean cavity decay time and negligible depletion of the ground state, the peak wavelength of a random laser does not change as a function of pump power. Therefore, to describe the spectral response

(a)

(b)

(c)
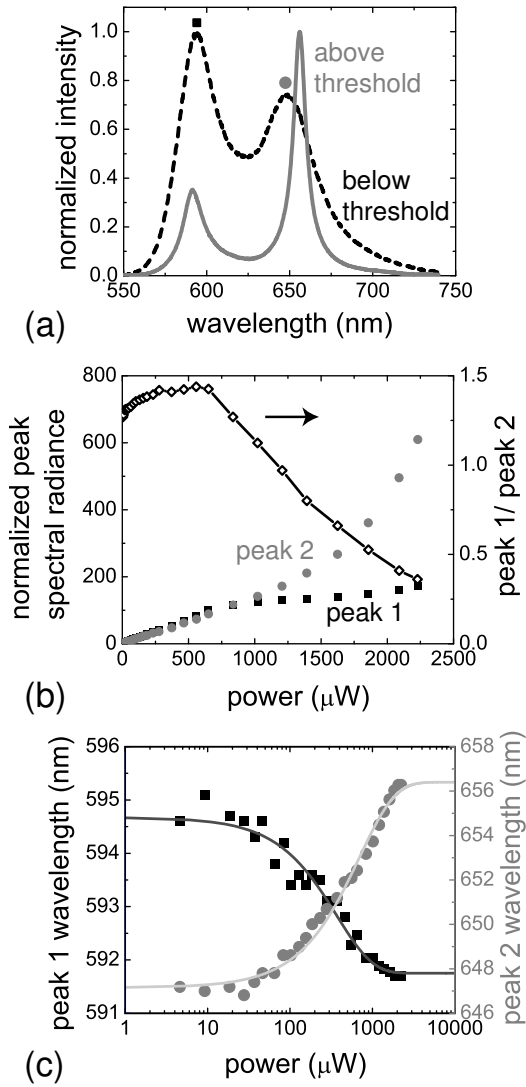
Figure 5.3: (a) spectra below (black, 84 μW) and above (gray, 2230 μW) threshold for sample 5. The absolute peak spectral radiance is a factor ~30 higher for the spectrum above threshold. Peak indicated by black square: peak 1. Peak indicated by gray disk: peak 2. (b) peak spectral radiance for peak 1 (black squares) and peak 2 (gray disks) normalized to the data point at 4.6 μW versus pump power. The black line is the ratio of the absolute values of the two peaks. (c) Wavelength of peak emission versus pump power for sample 5. Peak 1 (black squares), located at the blue side of the spectrum (left y-axis) shows a blue shift, whereas peak 2 (gray disks), located at the red side of the spectrum (right y-axis), shows a red shift. The solid lines are guides to the eye.

of the different random laser samples we study the steady-state solution of the rate equation for the photon density q_ω below threshold

$$\frac{dq_\omega}{dt} = -\gamma_c q_\omega - cn_1\sigma_\omega^{a,1}q_\omega - cn_2\sigma_\omega^{a,2}q_\omega + \gamma_r nL_\omega, \tag{5.1}$$

$$q_\omega = \left[\gamma_c + cn_1\sigma_\omega^{a,1} + cn_2\sigma_\omega^{a,2}\right]^{-1}\gamma_r nL_\omega. \tag{5.2}$$

Here n is the density of molecules in the upper laser level, γ_c is the effective cavity decay rate [80], γ_r is the radiative decay rate, c is the speed of light, $\sigma_\omega^{a,1}$ is the absorption cross section at frequency ω for the Rh640 molecules with density n_1, $\sigma_\omega^{a,2}$ is the absorption cross section at frequency ω for the Qblue molecules with density n_2, and L_ω is the probability of a spontaneous emission event at frequency ω with a certain frequency bandwidth $\Delta\omega$. In the above equations we assume $n \ll n_1$, which is valid below threshold. Equation (5.2) describes how the spontaneous emission spectrum of a pure dye, L_ω, is affected by the cavity decay rate and (re)absorption processes by the form factor $\left[\gamma_c + cn_1\sigma_\omega^{a,1} + cn_2\sigma_\omega^{a,2}\right]^{-1}$.

The effective cavity decay time, γ_c^{-1}, can be approximated by the Thouless time, $\tau_T = $
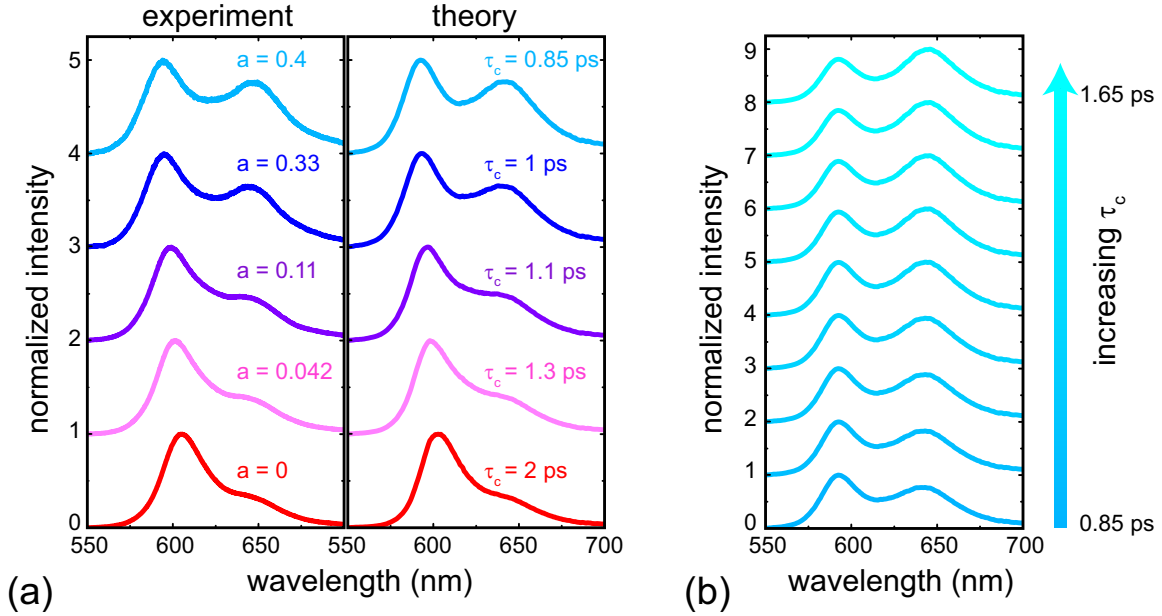
Figure 5.4: (a) Experimental and theoretical normalized emission spectra below threshold for sample 1 (bottom curve) to 5 (top curve). The number a denotes the ratio $n_{\mathrm{QBlue}}/n_{\mathrm{Rh640}}$. Excitation powers: 9.3 µW sample 1-4 and 18.6 µW for sample 5. Normalization constants for experimental curves: 851, 606, 356, 150, and 5.6 counts/s. To reproduce the experimental spectra in the calculation, the experimental concentrations were used with varying cavity decay times as indicated in the figure. (b) Calculated normalized emission spectra below threshold for $a = 0.4$ and linearly increasing values for the cavity decay time. The red peak becomes more pronounced for increasing cavity decay times.

$\frac{1}{\pi^2}\frac{L^2}{D}$, which describes the average time a photon spends in a slab with diffusion constant D and thickness L [171]. In our experimental configuration the exact value for the Thouless time is not known, since the excitation spot does not resemble a slab. If we assume the FWHM of the diffuse fluorescent spot on the sample surface to be the characteristic length scale (FWHM ≈ 130 µm) and a transport mean free path of ≈ 5 µm, the Thouless time is on the order of picoseconds.

Figure 5.4(a) shows experimental spectra below threshold and calculated spectra for different values of the ratio $a = \rho_{\mathrm{Qblue}}/\rho_{\mathrm{Rh640}}$. For the calculation the expression for the form factor was used together with the experimentally determined cross section spectra of Fig. 5.1. The effective cavity decay times in the theoretical plots were estimated manually by optimizing the correspondence between the theoretical and experimental spectra. We typically find cavity decay times of about 1 ps, which is of the same order of magnitude as values for the decay time as determined from relaxation oscillations in random lasers [172] and our estimation of the Thouless time. It should be noted that while our model is able to reproduce the shape of the experimental spectra, it does not reproduce the absolute intensities. In order to do so, the effect of the absorber on the number of excited molecules needs to be taken into account as well. For increasing concentrations of Qblue the peak emission shifts to the blue as is both observed in experiment and theory. Moreover, for increasing concentrations of the absorber the cavity decay time in the calculation needs to be decreased in order to obtain spectra that correspond with experiment. This decrease is due to shrinking of the emission volume at higher absorber concentrations.

In Fig. 5.4(b) calculated spectra are shown at a fixed concentration and various cavity

decay times. The dominant peak in the spectrum changes from the blue part to the red part of the spectra for a cavity decay time of 1.15 ps. At lower concentrations of Qblue, this shift in peak position occurs at higher cavity decay times

This theoretical analysis on the role of the cavity decay time on the output wavelength enables us to understand the experimentally observed mode competition effect. In *chapter 4*, we showed experimentally and numerically [144] that around the random lasing threshold the emission volume expands. Such an expansion in volume leads to a larger mean cavity decay time and can thus lead to a spectral switch of the main random laser peak. For spectra measured above threshold the switch becomes more pronounced than the calculated spectra shown in Fig. 5.4(b), because the two peaks compete with each other for the same gain. The dominant peak "eats" all the gain, thereby leading to a suppression of the second peak. This conclusion very likely also holds for other observations of mode competition in the literature [156]. In addition, expansion of the lasing volume explains the gradual change of the peak emission wavelength for increasing pump powers that is observed in most random lasers. Looking at the expression of the form factor in Eq. (5.2) suggests that a change in the concentration of molecules in the ground state also affects the form factor. However, such a depletion of the ground state cannot explain our experimental results since it would lead to less reabsorption and hence spectral shifts towards the gain maximum.

5.5 Conclusion and discussion

We have shown that introducing absorption leads to control over the peak emission wavelength of a random laser. A simple theoretical model enables to predict the position of the peak for various concentrations of the absorber. Our studies can be extended to absorbers other than non-fluorescent dyes, such as metal complexes and plasmonic metal nanoparticles [173, 174], in order to increase the flexibility in the output of a random laser. A very interesting twist to our work would be to pump around the gain medium in a random laser sample thereby enabling a change of the absorber concentration in situ.

In our analysis, the effective cavity decay time is considered to be constant over the whole spectrum. For increasing concentrations of the absorber, this assumption becomes invalid. Inclusion of a spectrally dependent effective cavity decay time is then necessary. Introducing a spectrally dependent cavity decay time in the analysis also enables a better understanding of Mie-tailored random lasers.

CHAPTER **6**

Narrow spectral features in random lasers

In this chapter, we systematically study the presence of narrow spectral features in a wide variety of random laser samples. The occurrence of narrow spectral features is shown to be strongly dependent on the sample preparation and configuration. By interpreting our data in terms of mode competition, we are able to explain the observed experimental trends. Smooth random laser spectra are a consequence of competing modes for which the loss and gain are proportional. Spectral spikes are associated with modes that are uncoupled from the mode competition in the bulk of the sample.

6.1 A short history of spikes: a scattered field

In the previous chapters on amplifying random media, the combination of multiple scattering and gain led to narrowing of the emission spectrum with increasing pump powers [74, 77, 93]. The introduction of new experimental and analytical methods, enabled us to determine the quantum efficiency of the gain medium in *chapter 2*, to discover the expansion of lasing volume in *chapter 4*, and to tune the output wavelength in *chapter 5*. In all these experiments the measured output spectra were smooth curves with at most two peaks.

These smooth spectra stand in sharp contrast with the spectrally narrow emission features that have been found in a subset of the experiments on random lasers [84, 85, 91]. The experimental discovery of amplifying random media that exhibit several peaks in the emission spectrum by Cao *et al.* [85] has truly boosted the field of random lasing as a whole. In fact, about one third of the random laser literature[1] deals with these features. The origin of these so-called spikes remains much debated even after more than a decade

---

[1]This fraction was estimated by counting the number of articles dealing with narrow spectral features out of all articles that appeared when using the keyword "random laser" at www.webofknowledge.com on February 23, 2012.

of research. Understanding this intriguing phenomenon promises to give more insight in random lasers and multiple scattering of light in general [93].

Historically, experimental groups have been divided between two schools of thought attributing spikes to either localized [84] or extended modes [91, 175]. A fundamental difference appeared between systems in which spikes reproduce at a fixed spectral position [85, 176] and systems in which the positions of spikes are uncorrelated from shot-to-shot [91]. In the case of fixed spectral positions, a spatial structure inside the sample can be associated with a spectral spike [87]. In several experimental papers, the spatial extent of these random laser "modes"[2] was studied [176–179]. The observation of structures confined in space has led to the interpretation of random lasing as a manifestation of Anderson localization [85, 178]. No experiments have been performed that show Anderson localization in both passive and active random media simultaneously. Therefore, an explanation of random lasing in terms of Anderson localization remains elusive.

More recently, three pioneering experiments have led to alternative explanations for the observation of spikes in random lasers. Fallert *et al.* [178] argue that localized and extended modes can co-exist while reaffirming that strong scattering of light is a prerequisite for random lasing. Tulek *et al.* [180] on the other hand attribute lasing to resonators inside the sample [179] and argue that strong scattering is detrimental to random lasing. In the work of Leonetti *et al.* [181] the explanation in terms of extended and localized modes is abandoned all together and mode coupling is suggested to be decisive in order for narrow spectral features to appear. Parallel to the ongoing experimental research, great progress has also been made in understanding random lasers theoretically. Several groups have shown that even the low quality modes of a weakly scattering sample can end up as lasing modes in lower dimensional systems [86, 87, 182]. An ab-initio self-consistent theory based on strong mode interactions has been worked out by Türeci *et al.* [86, 183] that is able to explain spectral spikes in random lasers for weakly scattering media without the need to invoke the concept of Anderson localization. Despite these numerous studies in both theory and experiment, it remains a challenge to link insights in theory to experiment and vice versa.

6.2   Systematically studying narrow spectral features

Puzzled by the rich variety of interpretations in the random lasing community, we decided to unscramble the vast amount of literature on random lasers that are made by dispersing a colloidal scattering material in a solution of laser dye [77, 184]. Unique to dispersive random lasers is the ability to *independently* control the scattering strength and the gain strength by controlling the concentrations of scattering particles and dye molecules separately. We ordered the available literature by the type of reported spectra and by extracting the mean free path and gain length [77, 89, 91, 144, 156, 168, 184–191]. We conjecture that the mean free path and gain length are the decisive quantities in understanding the physics of a random laser, because together they represent the two essential ingredients of any laser: feedback and gain. We shall see later on that neglecting the dependence on the size of the excitation area is oversimplified. For those experiments where the mean free path and

---

[2]Mathematically, a "mode" refers to an element of an orthogonal set of eigensolutions to a particular equation in a closed system. Experimental studies on random lasers are done in open environments by definition. Therefore, the use of the term "mode" is technically incorrect. We use the term in this chapter rather loosely, to refer to the electromagnetic intensity distribution associated with a narrow spectral feature.

Figure 6.1: Overview of spike observations in the literature plotted in the gain length (ℓ_g) versus mean free path (ℓ) plane. Every point represents a measurement on a dispersive random laser system. Filled disks (•): spikes reported. Open squares (□): no spikes reported. The gray shaded area is a guide to the eye that indicates the region of smooth spectra.
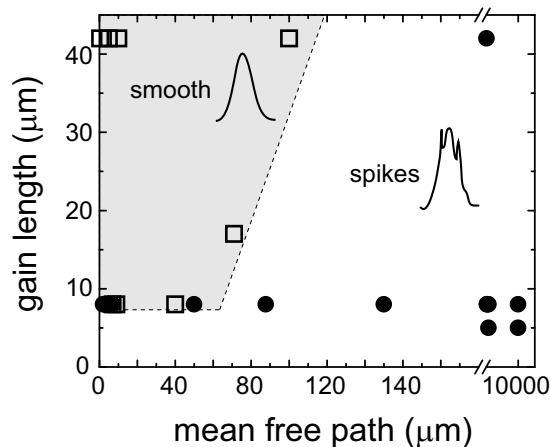
gain length have not been reported, an estimation was made based on the concentration of scatterers and dye. The literature survey, summarized in Fig. 6.1, suggests a remarkable trend: spectral spikes are predominantly reported in systems where the mean free path is large with respect to the gain length, *i.e.* where scattering is weak compared to gain. This trend might already come as a surprise, since many studies hint at strong multiple scattering being a requirement for spikes.

The ordering of the literature illustrates how a systematic study on narrow spectral features [192] enables the discovery of remarkable experimental trends. Part of the difficulty in understanding the occurrence of spikes in random lasers is caused by the wide variety of samples and interpretations used in the literature. The experiments described in this chapter show that observing random laser spikes often relies on subtleties in the used experimental methods.

In the first part of this chapter, we experimentally study random lasing phenomena in a strongly scattering porous semiconductor (GaP) infiltrated with and surrounded by laser dye in Sec. 6.3. We choose this type of sample, discussed in Sec. 6.3.1, as it has been put forward [176] as an ideal system for studying random lasers in which the narrow spectral features reproduce. Using a new experimental arrangement, based on confocal microscopy techniques, we gain access to the microscopic mode structure at the surface of this random material. In Sec. 6.3.2, the experimental apparatus is discussed. Measured spatial profiles associated with random lasing spikes are presented and analyzed in Sec. 6.3.3. The spatial structure of random lasing modes is compared to speckle in a passive medium. Several key parameters are identified, such as pump power and pump area, which influence the presence of reproducible spikes in the emission spectrum. Quantitative tools to study the reproducibility of spectral spikes are given and discussed. We carefully study how laser dye located outside the random medium influences the random lasing emission in Sec. 6.3.4.

In the second part of this chapter, we elaborate on our literature survey and investigate systematically how the gain length, ℓ_g, and the mean free path, ℓ, affect the occurrence of spikes in random lasers in Sec. 6.4. For this purpose, random laser samples were fabricated over a wide range of gain and scattering strengths as we discuss in Sec. 6.4.1. Statistical information on the properties of spikes is important for the connection between new theories and experimental observations. However, only a small number of articles present such an analysis [176, 180, 186, 189, 192–195]. We characterize our random laser spectra by
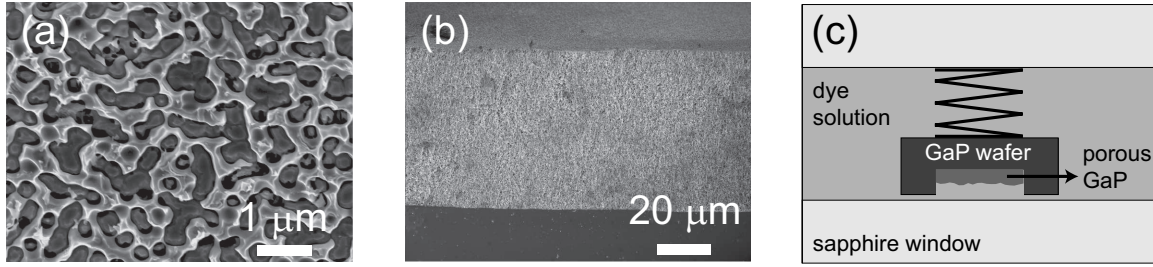
Figure 6.2: (a) top SEM image of a porous GaP sample. (b) a slightly tilted side view of a porous GaP sample. (c) sample configuration. A light spring pushes the sample onto a sapphire window.

analyzing every spike individually in Sec. 6.4.2. This analysis provides us with a rich data set on the distribution of the height, line width, spectral position, and spectral spacing of spikes, which we discuss in Sec. 6.4.3.

Our interpretation of the narrow spectral features is discussed separately at the end of this chapter. By introducing a two-mode model that includes gain competition in Sec. 6.5 we are able to explain our results qualitatively.

6.3 The spatial structure of random laser modes

6.3.1 Sample fabrication and configuration

Random laser samples were made by infiltrating strongly scattering porous GaP with an acidic solution of 20 mM Rhodamine 640 perchlorate in methanol. The dye solution was put in an ultrasonic bath for 30 minutes to ensure the dye was completely dissolved.

The porous GaP samples were fabricated by electrochemically etching a 9×9 mm^2 piece of a 0.5 mm thick crystalline GaP wafer (MTI corporation, carrier concentration $= 2\text{-}8\times10^{17}$ cm^{-3}, n-type, S-doped, (100) orientation) in a 0.5 M aqueous solution of H_2SO_4 under dark conditions. In general, the size of the pores, the pore density, and the shape of the pores depend on the dopant density, the potential at which the sample is etched, and the used electrolyte [196]. A highly reflective top layer is formed during the etching process. To remove this top layer we used an intermediate etching step at a high potential lying in the regime of passivation [176]. After fabrication, the samples were cleaved and inspected with a Scanning Electron Microscope (SEM). Figures 6.2(a) and (b) show two SEM images of one the porous GaP samples used in our experiments. From a two-dimensional autocorrelation analysis of the top SEM image, we find the typical correlation length at the surface of the sample to be 100 ± 50 nm.

The transport mean free path of the porous GaP samples in air was determined by an enhanced backscattering experiment [53, 54]. Infiltration of the porous structure with the dye solution slightly increases the transport mean free path, due to a lower refractive index contrast. After correcting for this lower refractive index contrast [197], we determined the transport mean free path in the two used random laser samples to be $\ell = 0.5 \pm 0.1$ µm and $\ell = 1.4 \pm 0.1$ µm at $\lambda = 632.8$ nm. Since the disorder in porous GaP is quenched (that is: the position of the scatterers does not change in time), the samples are well suited for static speckle and random laser experiments.

For the experiments, the samples were placed in a sample holder which was filled with the 20 mM dye solution, see Fig. 6.2(c). A spring was used to press the porous GaP sample against a 3 mm thick sapphire window. Both pumping and collection of the random laser
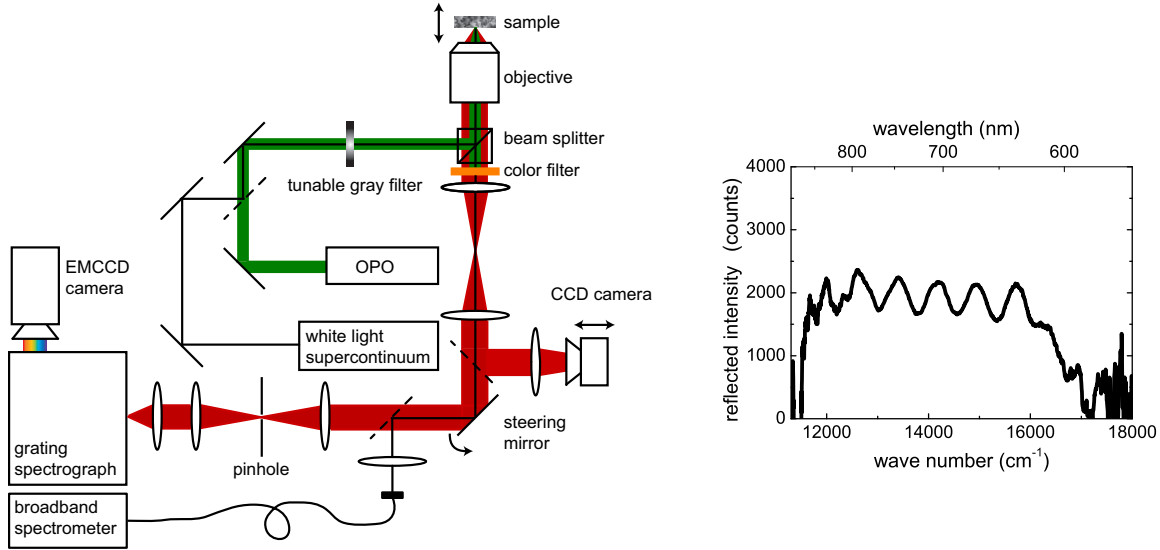
Figure 6.3: (left) Schematic overview of the experimental apparatus. The dashed line represent a flip mirror. (right) Interference fringes due to space between the porous GaP sample and the sapphire window. The sample was illuminated by a white-light supercontinuum source. The shape of the spectrum is corrected for the spectrum of the white light source.

emission was done via this sapphire window. The holder was mounted onto two translation stages to allow for selecting different areas on the sample manually.

6.3.2 Apparatus for spatially resolved spectral measurements

Figure 6.3 shows a schematic overview of the experimental setup. The excitation scheme is similar to the one in *chapter 4*. The wavelength of the pulses was selected in a range between 555 and 565 nm at an energy below the indirect band gap of GaP (548 nm), in order to prevent damage due to absorption. Light emitted by the random laser was collected using the excitation microscope objective and filtered by a 567 nm long pass filter (Semrock). To enable two-dimensional spatial mapping of the random laser emission at the sample surface, we introduced a spatially and spectrally selective detection scheme as shown by the red shaded region in Fig. 6.3. This detection path consisted of a bi-directional steering mirror (FSM-300, Newport), two achromatic lenses ($f = 100$ mm) and a pinhole (20 µm). Two 200 mm relay lenses placed before the steering mirror prevented the beam from walking in the detection path. The scanning experiments were done with a 0.55 NA microscope objective (CFI LU Plan Epi ELWD 50x, Nikon). The spatial resolution was 750 ± 50 nm. All other experiments were done with a 0.25 NA microscope objective (Leitz). After passing the detection path, the light was detected using a spectrograph (Oriel MS-257, resolution 0.5 nm) and an EMCCD camera (C9100-02, Hamamatsu).

Determination of distance between sample and sapphire window

In the geometry of our experiment, it is unavoidable that a thin fluid layer is present between the multiple scattering sample and the sapphire window. The thickness of this fluid layer is a crucial parameter in our random laser studies since it determines how much amplification of light takes place outside the multiple scattering sample. Typical values for this thickness lie between 5 and 15 µm. The distance between the sample and the window
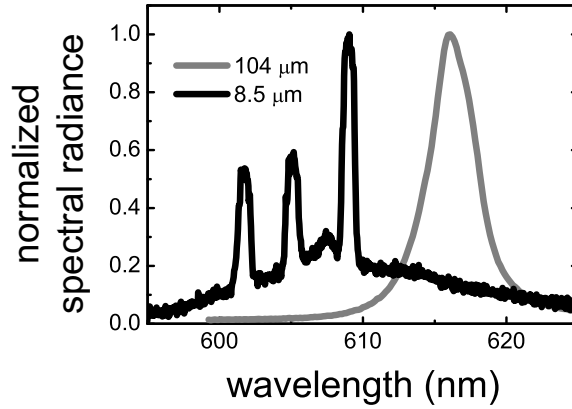
Figure 6.4: Emission spectra of a porous GaP random laser above threshold for two different excitation conditions. The black line shows the spectrum above threshold for a random laser with a fluorescent profile of 8.6 μm in radius. Clear spikes are observed. The gray line shows the spectrum above threshold for a random laser with a fluorescent profile of 104 μm in radius. The emission spectrum is narrowed, but no spikes are observed.

depends on the particular configuration of the sample inside the sample holder and cannot be controlled manually. In order to determine the thickness of the fluid layer we used the method of white light interferometry. Light from a white light supercontinuum source (Fianium SC-450) was coupled into the setup and subsequently analyzed with a broadband fiber spectrometer (Ocean Optics USB 4000). An example of a reflection spectrum is shown on the right side of Fig. 6.3. In this figure the reflected intensity is shown as a function of wave number. Clear interference fringes are visible. The intensity has been corrected for the spectral shape of the white-light source. The fringes are due to multiple reflections between the sapphire window and the porous GaP sample and their visibility is not constant for all sample positions. Fringes with higher visibility are observed when crystalline GaP is illuminated. The spacing of the fringes, the free spectral range, is dependent on the distance between the sample and the window, L, by [135] $\Delta\nu_{\text{fsr}} = c/(2nL)$. Here $\Delta\nu_{\text{fsr}}$ is the free spectral range, c is the speed of light in vacuum, and n is the refractive index of the medium enclosed by the two reflecting surfaces.

6.3.3 Results on GaP random laser

In this section we discuss the outcome of three different experiments with porous GaP random lasers. In general, a power threshold is present around which the emission spectrum changes. For small excitation areas (< 1000 μm^2) the emission spectra above threshold become dominated by spikes, whereas for large excitation areas the output spectrum is narrowed but smooth. The different character between the spectra above threshold is striking in Fig. 6.4 in which normalized single-shot spectra 1.3 times above threshold are plotted for a small excitation spot (8.6 μm in radius, 0.078 μW/μm^2) and a large excitation spot (104 μm in radius, 5.2 $\cdot 10^{-3}$ μW/μm^2). For the small pump spot, clear spikes are visible. For the large pump spot, the output spectrum consists of a smooth narrowed amplified spontaneous emission (ASE) spectrum.

In a first experiment, the spatial structure of random laser modes associated with spectral spikes is measured using confocal microscopy techniques. The size of random laser modes is compared to the size of speckles. Two experiments to investigate the presence and
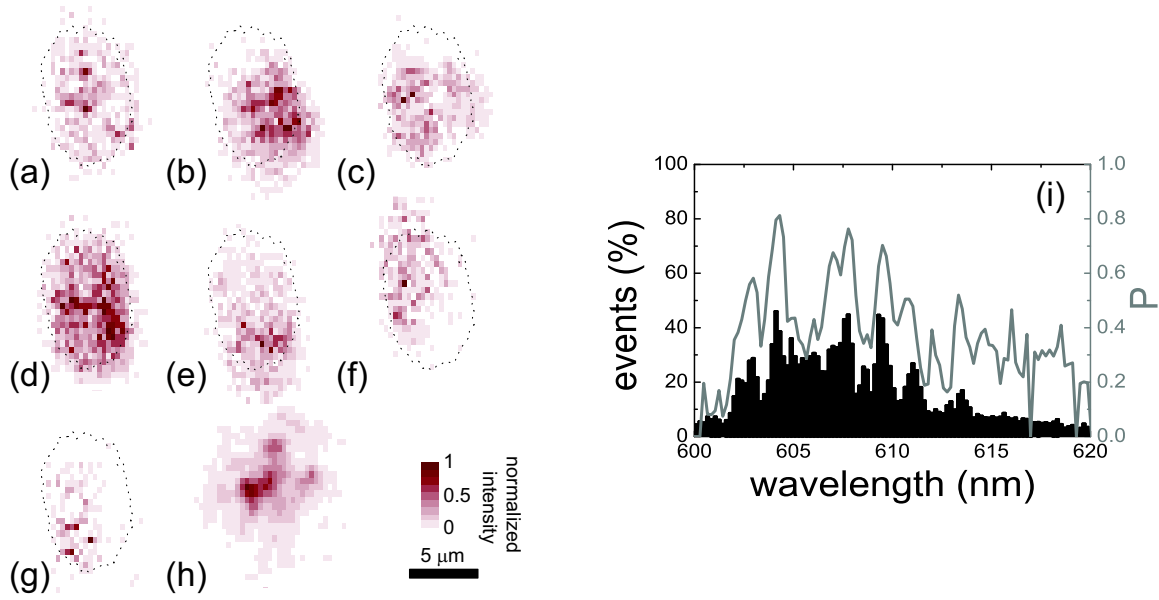
Figure 6.5: Experimentally determined spatial mode maps for seven modes at seven different wavelengths. (a) 603 ± 0.2 nm, (b) 604.3 ± 0.2 nm, (c) 607 ± 0.2 nm, (d) 607.8 ± 0.2 nm, (e) 609.5 ± 0.2 nm, (f) 610.8 ± 0.2 nm, (g) 613.3 ± 0.2 nm. The black dotted line is the 50% intensity contour of the diffuse fluorescence spot. The color coding for each plot is independent. In (h) an OPO speckle pattern (605.1 nm) is shown. (i) The black histogram denotes the percentage of pixels on which a spike with a certain wavelength is detected (left y-axis). The red dashed-dotted line is the correlation coefficient between two subsets (P_S, right y-axis) that indicates the stability of the measurement.

reproducibility of spectral spikes under various experimental conditions are presented and discussed.

Spatial structure of random laser modes

We studied the spatial structure of random laser modes in the regime where spikes are clearly visible in the output spectrum. Spatial maps of the entire region excited by the pump spot in the random laser sample were made by confocal scanning (excitation energy: 0.5 ± 0.1 μJ per pulse). The x-position of the detection area on the sample was scanned in steps of 330 nm, the y-position in steps of 440 nm. The total scan comprised 41×41 pixels. At every pixel in the scan, 25 spectra were measured with an exposure time of 0.2 s. The spectra were smoothed by adding four adjacent data points in order to average out the read-out noise of the EMCCD camera. Figure 6.5 shows spatial intensity maps for spikes at seven different wavelengths together with the 50% intensity contour of the diffuse fluorescence spot (diffusion of both the pump and fluorescence light increases the excited volume inside the sample). The profile of the fluorescence spot follows the profile of the population inversion in the gain medium. The diffuse fluorescence spot is slightly elliptical which allows us to study the effect of this asymmetry on the mode structure. The maps are constructed by adding the spike intensity for the 25 measured spectra at one pixel.

The spatial mapping experiment gives an insight in how random lasers work. Figure 6.5 reveals three key characteristics of modes in GaP random lasers. First, modes of different frequency have a significant spatial overlap at the surface. Second, the intensities of the modes fluctuate in space. Third, the positions of the modes do not always coincide with

the peak intensity of the pump spot.

Stability analysis of spatial mode maps

Spatial mode maps can be constructed from the raw data for every wavelength. In this rather technical subsection, we determine at which wavelengths the spatial mode maps are reproducible, in order for us to be able to separate useful information from noise.

The Pearson correlation coefficient between two different data sets, x and y, is defined as [198]

$$P \equiv \frac{\sum_i (x_i - \bar{x}) (y_i - \bar{y})}{\sqrt{\sum_i (x_i - \bar{x})^2 \sum_i (y_i - \bar{y})^2}}. \tag{6.1}$$

The correlation coefficient is one when the data sets are fully correlated, and zero when they are not correlated at all. For every wavelength, we now construct two spatial mode maps: the first map is calculated using 12 out of the 25 available spectra per pixel, the second map is calculated using the remaining 13 spectra. The Pearson correlation coefficient between these two maps, P_S, is calculated for every wavelength. In this case, the subscript i in Eq. (6.1) denotes a particular pixel in the map.

Figure 6.5(i) shows P_S as a function of wavelength together with a histogram of the percentage of pixels that contain a certain spike. We consider spatial maps at wavelengths where P_S is higher than 0.5 to be sufficiently stable for further analysis. Seven modes fulfil this criterion, namely all the modes shown in Fig. 6.5(a)-(g).

Size of random laser modes and speckle

The grainy intensity profile of random laser modes might at first glance resemble speckle. To compare the size of random laser modes with the size of speckles we study the intensity-intensity autocorrelation

$$C(\Delta r) \equiv \frac{\sum_{x,y} [I(x,y) - \langle I(x,y) \rangle] [I(x',y') - \langle I(x',y') \rangle]}{\sum_{x,y} [I(x,y) - \langle I(x,y) \rangle]^2}. \tag{6.2}$$

Here $I(x,y)$ denotes the measured intensity at pixel (x,y) and $(\Delta r)^2 = (x'-x)^2 + (y'-y)^2$. The triangular brackets denote ensemble averaging. Figure 6.6 shows the 2D ensemble averaged autocorrelation of the seven converged random laser modes and of twenty speckle patterns in reflection obtained by illuminating the sample with light (605.1 nm) generated by the optical parametric oscillator (OPO). The ensemble average for the random laser modes was constructed by averaging the seven stable mode profiles. The mode profiles were shifted laterally to let their centers of mass overlap. Not performing this centering procedure does not affect the outcome significantly. For the speckle pattern the ensemble average is obtained by averaging over twenty different realizations of disorder.

In Fig. 6.6, two-dimensional ensemble averaged autocorrelations and cuts through this data are given for both random laser modes and speckle. The red line is a theoretical prediction from Shapiro for the speckle size inside a random medium [199], given by $[\sin k_0 \Delta r / (k_0 \Delta r)]^2 \exp(\Delta r / \ell)$, convolved with the microscope's point spread function.
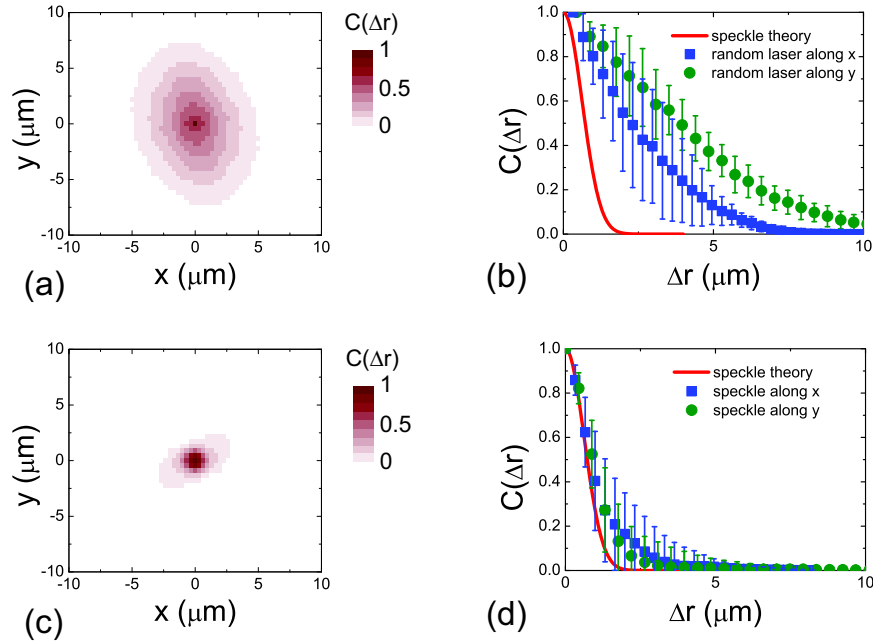
Figure 6.6: Two-dimensional ensemble averaged normalized autocorrelation plot for (a) random laser modes and (c) speckle. Cuts along the x-direction and y-direction are given for (b) random laser modes and (d) speckle. The red solid line is a theoretical prediction for the speckle size. The bars represent the standard deviation.

In this theoretical curve we neglect the minor adjustments made by Freund and Eliyahu [200] for correlations on the surface of a random medium. The point spread function was corrected for the presence of the thick sapphire window, which changes the exit pupil and thereby decreases the effective numerical aperture of the microscope objective from 0.55 to 0.3 as was determined from HeNe speckle measurements (as a side remark we note that polarization does not influence the normalized autocorrelation of speckle). The first point in the random laser autocorrelation graph accumulated all remaining experimental noise due to the intrinsic fluctuations in intensities of spikes, therefore the second point in the graph was used to normalize the data. From the Full-Width at Half-Maximum (FWHM) values of the autocorrelation graphs we find the size of random laser modes to be 3.0 ± 0.7 μm and the size of the speckles to be 0.8 ± 0.1 μm. This measured size of the random laser modes is also an order of magnitude larger than the correlation length of the material disorder in porous GaP. The size of the speckles is in good agreement with the theoretically expected value. The asymmetry that was present in the profile of the pump spot, also appears in the autocorrelation of the random laser modes. This asymmetry in the autocorrelation indicates that the spatial structure of the measured random laser modes is to some extent influenced by the size of the pumped volume. Furthermore, in contrast to speckle in a passive medium, random laser modes do not span the entire excited area, instead random laser modes are confined.

Statistics and reproducibility of spectral spikes

In general, spectral spikes require a careful tailoring of experimental conditions. The intensities of the spikes and in some case the spectral positions differ from shot-to-shot. Studies on the chaotic behavior of spikes have recently been initiated by Mujumdar *et al.* [185] and
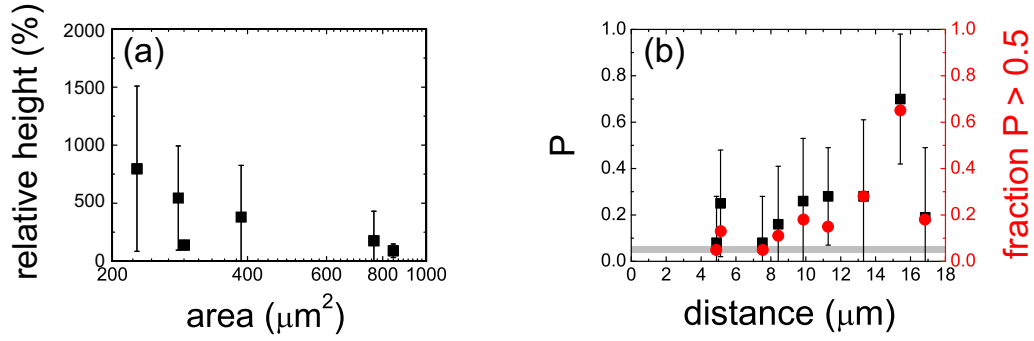
Figure 6.7: (a) Role of excitation area on statistics of spectral spikes. The number of spikes per spectrum (in black) and the relative height of a spike (in red) are plotted versus the excitation area in a semilog plot. The data points represent the mean of the data, the bars the standard deviation. (b) Reproducibility of spike spectral position for different distances between the sample and sapphire window. The black squares represent the mean values of the Pearson correlation coefficient between single-shot spectra, the bars represent the standard deviation. The red dots represent the fraction of coefficients between two single-shot spectra that is higher than 0.5. The gray bar indicates the fraction of coefficients that are higher than 0.5 between single-shot spectra taken at different positions on the sample.

Wu and Cao [201]. To find out more about the nature of the spikes we conducted two additional experiments where no pinhole was present in the setup. In the first experiment, we analyze for the first time the role of the excitation area on spike statistics. Fifty single-shot emission spectra were measured for different excitation areas at a fixed value for the pump fluence, namely 0.07 ± 0.01 μW/μm^2. Second, to understand the role of light amplification outside the random medium, the reproducibility of spectra containing spikes were studied for different distances between the sample and the sapphire window using a similar data analysis as used by Mujumdar *et al.* [185].

Figure 6.7(a) shows the relative height of the spikes in the spectrum versus the excitation area. Peaks in the spectra were named a spike when the spike intensity was higher than eight times the standard deviation of the noise and when data-points adjacent to the spike within the spectral resolution were lower than the spike value itself. The relative height of spikes increases when the excitation area decreases. However, for all values of the pump spot area we find spikes in the spectrum. Similar experiments were performed for different spots on the sample and yielded the same trends.

The reproducibility of spikes in spectral position is studied by calculating the Pearson correlation coefficient as defined in Eq. (6.1) for several distances between the sample and the sapphire window. Now i in Eq. (6.1) denotes a particular position in the spectrum. The correlation coefficient is one when the spectra are fully correlated, and zero when they are not correlated at all. For every distance, 50 single-shot spectra above threshold were recorded, the fluorescence background was subtracted, and the spectra containing spikes were selected for further analysis.

In Fig. 6.7(b) the calculated mean of the correlation coefficient is represented by the data points and the standard deviation is used as an error estimate. For all distances between the sample and the sapphire window, the correlation coefficient between the different spectra is small (< 0.5) except for the one data point at 15 μm. It is therefore tempting, but incorrect, to conclude from this analysis that the spikes appear chaotically in the spectrum and reproduce poorly. In fact, spikes do reproduce in spectral position as can be deduced

from a high value (> 0.5) of the correlation coefficient of some spectra pairs. Therefore, the fraction of coefficients that is higher than a specified value is a better way to study the reproducibility of spectral spikes. The fraction of coefficients higher than 0.5 is plotted in Fig. 6.7(b). The gray bar represents the fraction of correlation coefficients higher than 0.5 between spectra taken at different positions on the sample. Above a distance of 8 μm the fraction of highly correlated spectra taken at one position becomes significantly higher than this background value. We conclude the reproducibility of spikes slightly increases for larger values of the distance between the window and sample.

6.3.4   Influence of dye surface layer on random laser emission

The relative height of spectral spikes decreases with excitation area. The spikes, in other words, disappear in the Amplified Spontaneous Emission (ASE) background for larger pump spots. It has been suggested in the original paper by Letokhov [74] and more recently by Yamilov *et al.* [90] that a reduction of the system volume indeed facilitates the observation of spectral spikes due to a decrease in the total number of modes. There is however a second, experimental, reason for the decrease of the spike height for larger pump spots that obscures this effect. The small layer of dye solution located between the sample surface and the window can also give rise to ASE. In fact, we observed ASE in the cases of non-etched GaP and weakly scattering samples. The threshold for observing ASE in this thin dye layer decreases for larger excitation areas due to the presence of longer paths that receive more gain. For excitation areas larger than 1000 μm^2 the threshold for ASE in this dye layer is lower than the threshold for observing spikes. This dye layer thus prevents studying effects taking place inside the porous GaP for large excitation spots.

The high concentration of dye molecules in our system causes the gain length in the system to be small ($\sim$2 μm when all dye molecules are simultaneously excited to the upper laser level, quenching effects can be ignored, and $\sigma_e = 4 \cdot 10^{-20}$ m^{-2}). Therefore, spikes in the emission spectrum could already arise due to lasing between two weakly reflecting interfaces. For example, a distance of $\sim$5 μm between crystalline GaP ($R = 0.2$) and the aforementioned sapphire window ($R = 0.02$) results in a tiny dye laser under the conditions of our experiment. The reflection coefficient of porous GaP is much lower than the reflection coefficient of crystalline GaP, because scattering randomizes the reflection direction and the effective refractive index of porous GaP is lower than the refractive index of crystalline GaP. In the case of porous GaP ($R = 0.05$) a spacing of $\sim$7 μm between the sample and the window is needed for coherent lasing outside the sample. This value for the spacing is an underestimation, because the quantum efficiency of Rhodamine dyes significantly decreases for concentrations higher than 10 mM [202]. This reduction in quantum efficiency leads to longer minimal gain lengths and therefore to larger required spacings. Based on Ref. [202], the required spacings become twice as large. It also explains why a further increase in dye concentration was to no avail for inducing more spikes in Ref. [172].

Experimentally, we observe spikes for all thicknesses of the fluid layer between the sample and the sapphire window. At the same time, the reproducibility of spectral spikes is slightly enhanced for larger thicknesses of the fluid layer. However, some of the measured thicknesses for the dye layer are still too short to explain the spikes by standard lasing action caused by the averaged reflectivity of the sample and the reflectivity of the window. Hence, we attribute spikes to lasing originating partly from within the porous GaP. The alternative possibility, *i.e.* lasing between the window and areas on the sample that have

a higher than average reflection coefficient, is highly unlikely, since the measured ensemble averaged random laser mode size is an order of magnitude larger than the correlation length of the microscopic disorder in porous GaP. The spectral spacing between the spikes typically remains between 1 and 2 nm for all thicknesses of the fluid layer, which is another clear indication that the amplification takes part partly within the porous GaP and is not solely due to lasing between the sample interface and the sapphire window.

The experiments do show that surface effects play a more important role than was previously assumed. For small distances (in terms of the gain length) between the sample and the sapphire window, most amplification takes place inside the random medium. Due to the high number of modes (order of thousands) available in such a medium [15], there are many possible laser modes. Therefore, which of the available modes turn "on" depend on statistical fluctuations inside the dye solution and change from shot-to-shot. In such a situation the spectral position of the spikes cannot be determined a priori. The focus in the remainder of this chapter lies mostly on explaining the occurrence of spikes themselves, rather than these statistical fluctuations.

6.3.5 Conclusion on random lasing in and around porous GaP

In the field of random lasing three distinct forms of lasing have been reported in the past: lasing in the form of narrowing of the emission output spectrum, lasing in the form of a chaotic appearance of spectral spikes, and lasing in the form of reproducible spectral spikes.

We observed these three different types of lasing in and around a porous GaP sample infiltrated with laser dye. For large excitation volumes (*i.e.* large compared to the transport mean free path and the gain length), Amplified Spontaneous Emission (ASE) dominates the emission spectrum. This ASE is due to a layer of dye between the sample and the sapphire window. For small pump spots that are comparable to the gain length and the transport mean free path, spectral spikes start dominating over the ASE spectrum. Depending on the distance between the sample and the holder window the spikes reproduce in spectral position or appear chaotically in the spectrum. The reproducibility of spectral spikes is enhanced for larger distances, indicating that the relatively large extent of modes outside the random medium is a key property of stable random laser modes. This key property put forward by us [193] has in fact recently been used to tailor a random laser by directed stimulated emission [181, 203].

The intense debate in the experimental literature on the origin of spikes [85, 91, 176, 178] can partly be attributed to the fact that in these studies very different systems were taken into consideration. The outcome of our experiments emphasizes that spikes in random lasers are predominantly an effect occurring near the boundary of the multiple scattering system [86, 183]. The results apply to many random laser experiments, since pumping of random laser systems is almost always done via the outside, and the result is monitored in reflection. The combination of multiple scattering and short pump absorption lengths prevents random laser action to take place in the bulk of the sample. In such experimental configurations the leakiness of random laser modes to the outside is bound to play an important role.

By studying the spatial intensity-intensity autocorrelation of the random laser modes that are associated with spectral spikes, we are able to compare random laser modes directly with diffusive phenomena for the first time. The structure of these modes on the surface of the sample deviates from speckle. Our approach has recently been employed to study

another type of random laser and led to similar results [204]. The gain in an active medium acts as a selection mechanism that chooses a subset of the modes available in the medium to start lasing. The modes are shown to have a significant spatial overlap at the surface, making gain competition effects such as spatial hole burning very plausible.

From an experimental point of view, applying our spatially and spectrally selective detection scheme to random lasers with a smooth emission spectrum is also of relevance as it allows for studying the spatial dependence of the cavity decay rate. We showed in *chapter 5* that differences in the effective decay rate appear as spectral shifts in the emission spectrum. By doing so, we incorporated the distribution of path lengths in a random medium into a single quantity. The proposed experiment, possibly in combination with the side imaging technique of *chapter 4*, probes spectral shifts locally and thereby enables us to retrieve the distribution of path lengths in a random laser.

6.4 Constructing a random laser phase diagram

6.4.1 Sample fabrication

From the interpretation of the available literature presented in Sec. 6.2, we conclude that the appearance of spikes critically depends on the amount of scattering and gain in the system. In the experiment presented in this section, we aim to find the transition from spiky to smooth spectra in the ℓ-ℓ_g plane by applying a bisectional algorithm with respect to the scattering strength of our samples. At a fixed dye concentration, we start with a weakly and a strongly scattering sample. A new sample is then prepared after measuring these two samples. The scattering strength of the new sample is chosen such that it lies halfway in between those of the two closest measured samples that show opposing spiking behavior. This way, we minimize the difference between the scattering strength of our sample and the scattering strength for which the transition from smooth to spiky spectra occurs.

The studied random laser system is a dye solution (Rhodamine 640 P in methanol) in which elastically scattering titania particles (Ti-Pure R-900, DuPont) are dispersed. The characteristic interaction length scales are calculated using $\ell = 1/\rho\sigma$. In this formula ℓ is the gain length (mean free path), ρ is the concentration of particles, and σ is the stimulated emission cross section (scattering cross section). The stimulated emission cross section of the dye is $(4 \pm 0.5) \cdot 10^{-20}$ m^2 at $\lambda = 600$ nm, see *chapter 5* [169]. The scattering cross section of the colloids is $\sim 7 \cdot 10^{-13}$ m^2. The suitability of using $1/\rho\sigma_s$ for the scattering particles under consideration was previously shown to be reasonable [147]. The gain lengths reported in this section assume all dye molecules are excited to the upper laser level and are therefore minimal values. In reality the gain length will be spatially dependent and longer than these reported gain lengths.

The bisectional algorithm is applied on systems having calculated minimal gain lengths of 4, 8, 16, 24, 32, and 40 μm (dye concentrations ranging from 10 to 1 mM). For high dye concentrations (> 1 mM), the suspensions of TiO$_2$ become highly unstable. The titania particles sediment within minutes when the concentration is around 10 mM. To ensure dispersive stability over several hours, a small amount (0.1 g per 10 mL) of polyvinylpyrrolidone (PVP K-30) was added to all samples.

Samples are pumped with OPO light at a wavelength of 535 nm, using 5 ns long pulses at a repetition rate of 20 Hz. Emitted light is collected by the same lens that is used to
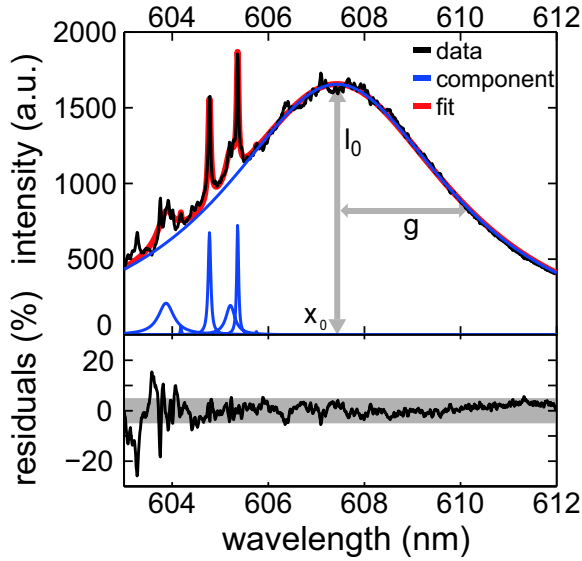
Figure 6.8: (upper panel) Example of a fitted high-resolution spectrum. The black line is the original data, the blue curves are the individual components used to fit the data and the red curve is the fitted sum of all components. The fit parameters, height (I_0), width (γ), and position (x_0) are shown. (lower panel) Residuals between the fit and the data. The grey area indicates a 5% deviation.

focus the pump light on the sample. All experiments are conducted above threshold, with a pump power of 1.5 mW. The area of the slightly elliptical pump spot is $(6.8 \pm 1.4) \cdot 10^3 \, \mu\mathrm{m}^2$. For every sample, 100 single shot spectra are recorded using a spectrometer that is operated at a spectral resolution of either 1 nm or 0.1 ± 0.05 nm.

6.4.2 Data analysis and spike detection

The measured spectra are either smooth narrowed curves with respect to the below threshold spectrum or narrowed curves with distinct spikes superimposed on them. The relative height of the spikes is typically a factor 10 lower compared to the spikes obtained with porous GaP random lasers, which makes their detection somewhat more involved. We have therefore fitted all these individual spectra with Lorentzian lineshapes. After smoothing the data to remove noise, the number and position of spikes is found by analyzing the second derivative of the data. The locations of minima in the second derivative correspond to spikes in the spectrum. Only minima that are considerably deviating (10% of the difference between the global extrema) from their nearest maxima (larger than 0.1% of the original, smoothed data) are selected as corresponding to spikes. Using this method, we find the width, amplitude, and position of every function representing either a spike or the narrowed background.

Figure 6.8 shows an example of a decomposed emission spectrum. The deviation of the original data to the fit is within 5% for the majority of the spectrum. This level of accuracy is typical for all spectra that have been analyzed. From this analysis, we conclude the fitting routine is able to reliably fit the elements of spiky spectra.

6.4.3 Results on dispersive systems

To study whether or not samples exhibit spikes, we analyze the average of the number of detected peaks. The inset in Fig. 6.9 shows the number of detected peaks per sample. A clear distinction is visible that separates spiky from smooth spectra as indicated by the
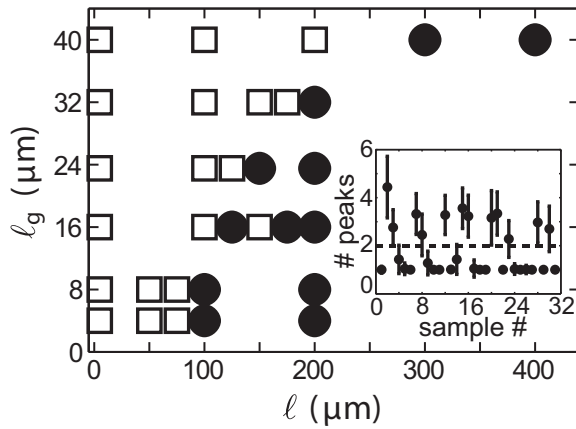
Figure 6.9: The appearance of spikes is shown as function of the mean free path (ℓ) and gain length (ℓ_g) of each sample, measured at 1 nm resolution. Filled disks ($\bullet$): samples with spikes. Open squares ($\square$): samples without spikes. Spectra showing more than two distinct peaks are considered to contain spikes. The inset shows the average number of fitted functions per spectrum, the error bars represent the standard deviation.
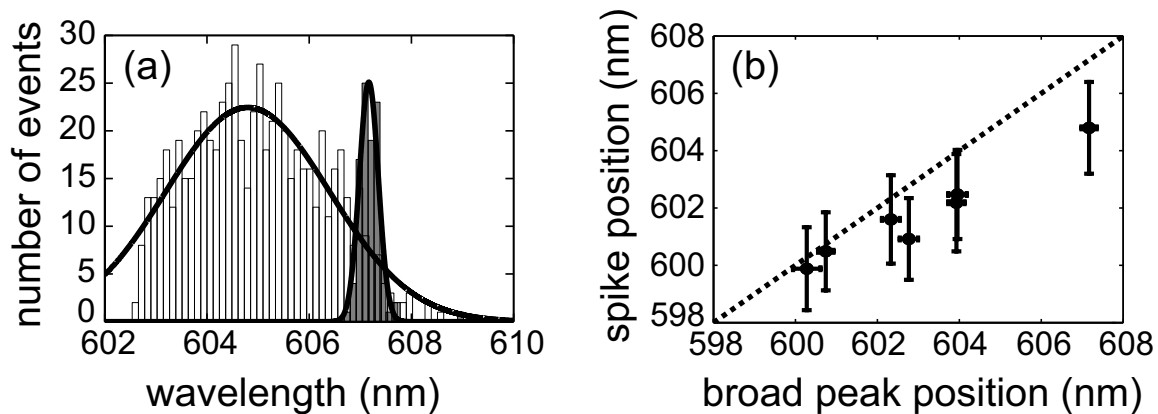
Figure 6.10: (a) Distribution of the central emission wavelength of spikes (open bars) and broad background peaks (filled bars) for our model sample. Both distributions are fitted with Gaussian profiles (black curves). (b) The mean of the spectral distribution of spikes with respect to that of the corresponding background peak. The length of the error bars is determined by the width of the distributions. The dotted line indicates equality of the wavelengths.

dashed line. Sometimes more than one peak is detected in samples that on average are considered to be smooth. These deviations are due to unavoidable uncertainties in the fitting routine. Therefore, we only consider samples that on average have more than two detected peaks per spectrum as "spiky" samples.

In Fig. 6.9, the appearance of spikes is shown as function of the sample parameters ℓ and ℓ_g. A clear trend is observed in this graph: spikes appear only in samples on the right-hand side of the diagram. This result directly implies that strong multiple scattering is not a critical necessity for inducing spikes. On the contrary, the more diffusive the sample becomes the less likely it becomes that spikes appear in the output spectrum. We note that both an increase in transport mean free path and a decrease in gain length lead to a less diffusive sample ($\ell \approx L$ with L the system length), because a decrease in gain length makes samples more absorbing and therefore leads to a shorter system length.

The obtained values for the fitting parameters allow us to study the statistics of spikes in much more detail. We limit ourselves to studying the high-resolution data to make sure all spikes are well separated. We analyze the spectral position of spikes and the broader background on which they reside. In Fig. 6.10(a), we show the spectral position
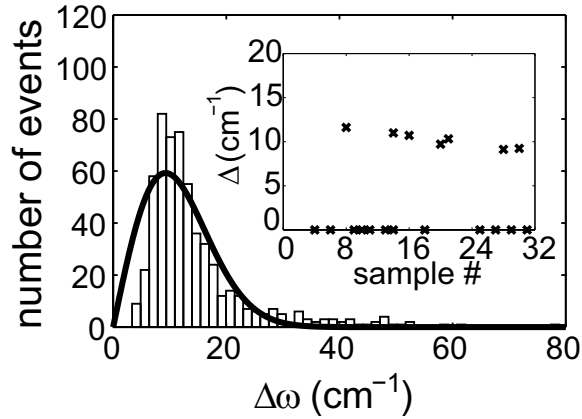
Figure 6.11: A distribution of spectral spacing values collected from one sample (bars). The curve represents Wigner's surmise fitted to the data. Inset: mean mode spacing as found by fitting Wigner's surmise to all collections of mode spacings. Samples with $\Delta = 0$ cm^{-1} have smooth emission spectra.

distribution of both the fitted spikes (white bars) and the fitted broader background (grey bars) for one sample. The spectral spread for the position of the spikes is larger than the spectral spread for the position of the underlying spectrum. Moreover, the spikes reside predominantly on the blue side of the broad profile. In order to compare the statistics of the different samples, these distributions have been fitted with Gaussians. In Fig. 6.10(b), the mean and variance of the spectral positions for the spikes are plotted versus the mean and variance of the underlying broad background. From this graph, we deduce that the emission wavelength of spikes is on average smaller than the central emission wavelength of the broad underlying profile for all samples.

The spectral spacing between neighboring random laser spikes is retrieved from the fitted Lorentzian profiles. A typical distribution of spacing values for one sample is given in Fig. 6.11. The spectral spacing between the spikes is clearly peaked around 10 cm^{-1}. We therefore deduce that level repulsion is present. This phenomenon has previously been reported for random lasers [81, 176]. We fit the spectral spacing distribution to a Wigner's surmise with mean mode spacing (Δ) as fit parameter. The fitted values for Δ are collected for several samples and are shown in the inset of Fig. 6.11. Surprisingly, we observe that the mean mode spacing is comparable for all systems that show spikes: $\Delta = 10.2 \pm 0.9$ cm^{-1}. Since this analysis is performed for systems with different concentrations of scatterers and gain molecules, we conclude that the extent of level repulsion does not significantly depend on the strength of scattering or gain.

The fitted values for Δ make it possible to compare our experimental results with theoretical random matrix calculations. Zaitsev studied the mode spacing of a two mode random laser theoretically [205]. He concluded that for wide gain profiles, the spacing of the lasing modes does not depend on the spacing statistics of the passive system. His conclusion matches with our experimental observation of a constant spacing for a wide range of sample parameters.

6.5 Two-mode model with gain competition

In order to comprehend the transition from smooth to spiky spectra in our dispersive samples and the occurrence of spikes in our GaP random laser, we set up a model consisting of just two laser modes. Although a two-mode model obviously represents a reductionist's

approach of modeling a random laser, it nevertheless provides insight behind the physics of random lasers. In addition, a two-mode model has the advantage of being analyzable analytically. The quasi-modes in a diffusive sample have a wide range of decay times and overlap spatially on intensity level. We therefore postulate that in a random laser, modes with different decay rates compete for the same gain. The number of photons in the two modes, q_1 and q_2, with cavity decay rates γ_c^1 and γ_c^2 are described by two rate equations that both depend on the same number of molecules in the upper laser level N [15]:

$$\frac{dq_1}{dt} = -q_1 \gamma_c^1 + \beta_1 \gamma_r N q_1 + \beta_1 \gamma_r N, \tag{6.3}$$

$$\frac{dq_2}{dt} = -q_2 \gamma_c^2 + \beta_2 \gamma_r N q_2 + \beta_2 \gamma_r N, \tag{6.4}$$

$$\frac{dN}{dt} = R - \gamma_r N - \beta_1 \gamma_r N q_1 - \beta_2 \gamma_r N q_2. \tag{6.5}$$

Where we have considered a unit quantum efficiency gain medium with decay rate γ_r. The factors β_1 and β_2 differ from the *effective* β-factor in earlier chapters in this thesis, because here they describe which part of the spontaneous emission contributes to the lasing process of a *single* mode. As discussed in Sec. 1.1.5, this single mode β-factor in a conventional laser is dependent on both the angular, β_Ω, and spectral, β_ω, overlap between spontaneous emission and the mode [206]: $\beta = \beta_\Omega \beta_\omega$. We propose the solid angle participation ratio of the mode with scattering function $f(\theta, \phi)$ as a convenient way to determine the geometrical part of the β-factor in a random laser by

$$\beta_\Omega = \frac{\left[\int f \mathrm{d}\Omega\right]^2}{4\pi \int f^2 \mathrm{d}\Omega}. \tag{6.6}$$

One of the unique properties of a truly diffusive random laser is the fact that on average no angular mode selectivity takes place [107, 169]. Individual diffusive modes are speckle-like and as a consequence a single mode is omnidirectional as well. Given the speckle intensity Rayleigh distribution, all modes have a similar solid angle participation ratio, and therefore β_Ω is constant for all modes. In this particular case of constant β_Ω, the differences in β-factor stem only from the spectral dependence of the β-factor. For the high gain modes with their spectrum centered around the peak of the gain curve, the β-factor then becomes proportional to the cavity decay rate. If we consider such a diffusive random laser by putting $\gamma_c^1 / \beta_1 = \gamma_c^2 / \beta_2 = \kappa$, we find from a steady-state analysis of Eqs. (6.3)-(6.5): $q_1 = q_2 = \gamma_r N / [\kappa - \gamma_r N]$. Surprisingly, the two modes with widely varying decay time thus contain the same number of photons. In popular terms: modes that waste but also earn a lot become just as rich as frugal modes that earn very little. Extrapolation of the model to a system with n modes sharing the same gain medium, leads to the conclusion that a smooth random laser spectrum is a direct result of the cavity decay rate and the β-factor being proportional to each other for n modes. In this framework, the spectral narrowing observed in diffusive random lasers is explained by the fact that modes in the wings of the gain curve have a smaller β_ω than modes in the center of the gain curve. Very lossy modes with large cavity decay rates located in the peak of the gain curve also have smaller values for β_ω, because the spectral wings of these modes simply fall outside the gain bandwidth. As a consequence the effective cavity rate decreases above threshold as was observed in *chapter 4* and put to use in *chapter 5*.

To explain the observed spikes in random lasers we return to the simple model of two modes. Starting from a situation where $\gamma_c^1 / \beta_1 = \gamma_c^2 / \beta_2 = \kappa$, there are two ways to let one

mode end up with more photons than the other mode. First, by simply changing the ratio γ_c/β for the two modes. This ratio is decisive in determining which laser mode ends up with the majority of photons and thus profits the most from the available gain. The mode with the smallest ratio eats up the gain for the other mode, sometimes leading to a complete quenching of the second mode. Second, one mode can become more prominent when the gain competition is reduced by splitting up the gain in more than one reservoir. For a completely uncoupled system, the number of photons in a lasing mode above threshold is given by $R/\gamma_c + 1/\beta$, which shows that in such a situation the mode with lowest cavity decay rate eventually becomes most prominent in the spectrum.

To determine which of the two mechanisms is responsible for inducing spikes in our experiment, we have another look at the results shown in Fig. 6.10(b). The fact that spikes appear systematically on the blue side of the spectrum, indicates that photons in the modes responsible for the spikes have traversed relatively short paths in the medium. Since longer light paths experience more reabsorption and are therefore red shifted as discussed in *chapter 5* [207]. The path length s is related to the cavity decay rate by $s = c/\gamma_c$. Apparently and somewhat counterintuitive, spectral spikes represent modes with a *large* cavity decay rate. In a typical spectrum, several spikes appear simultaneously at the blue side of the spectrum, while a broader smooth peak remains present at the red side. From this observation, we conclude that mode competition cannot be ignored for modes with low cavity decay rates, while at the same time mode competition starts to play a less dominant role for the high cavity decay rate modes.

Our experimental phase diagram shows that spectral spikes appear when the sample becomes less diffusive. At the same in our porous GaP random laser, it became clear that amplification outside the multiple scattering medium cannot be ignored. Once a random laser becomes less diffusive, that is $\ell \approx L$ with L the system length, β_Ω ceases to be constant for all modes. It is therefore likely that a compact mode with a short cavity decay time, but high β_Ω, is privileged over long cavity decay time modes. Moreover, the confinement of this mode also allows it to escape from the mode competition present among the other modes, further enhancing its output. Multiple spikes can then appear in the spectrum representing other well confined modes. However, the more extended modes with low cavity decay rates are still competing for the same gain in the bulk of the sample, which leads to a broader but smooth peak in the spectrum. Reports in the literature on the spatial structure of random laser modes [176, 178, 193] showing that the extent of the modes associated with spikes are small compared to the excitation region, also support our interpretation of the narrow spectral features as due to confined modes with a high β_Ω.

6.6   Conclusion and discussion

Our experimental observation of spikes being restricted to weakly scattering systems unambiguously shows that multiple scattering of light prevents the appearance of spikes. The results imply that spikes are caused by a process including only a low number of scattering events. We introduce a phase diagram that confirms previous indications of the importance of the ratio between the gain length and the mean free path in the literature [180, 188]. The statistics of the narrow spectral features is still largely uncharted territory. Our work reveals how rich the physics of random lasers becomes when studied systematically. We believe these statistical analyzes are key for creating more satisfying connections between theory and experiment in the future.

The analysis of a simple two-mode model is able to explain the trends of our experiments qualitatively. The combination of a shared gain medium and the absence of angular mode selectivity in a purely diffusive random laser, leads to the simultaneous lasing of those modes close to the gain maximum. This simultaneous lasing in its turn creates a smooth output spectrum. Increasing either the gain or decreasing the transport mean free path moves the system away from the diffusive regime and thereby destroys the assumption of no angular mode selectivity and a completely shared gain medium. Individual modes become visible in the output spectrum that are characterized by short cavity decay times and high spontaneous emission factors.

Our interpretation of random lasing in terms of mode competition also explains the results of some beautiful recent experiments [181]. Selectively feeding the modes in a random medium from the outside, as done, *e.g.*, in Ref. [181] by a non-isotropic excitation scheme or in our porous GaP random laser, allows some modes to escape from the competition for gain inside the sample and to start lasing independently from the other modes. Our model, in which two modes are entirely dependent on the same gain reservoir, is undoubtedly an oversimplification of a random laser. In a typical random laser thousands of modes are present with various spatial extent. We have implicitly made the assumption that such a system can effectively be studied by having one gain reservoir. Studying the break down of this assumption will surely lead to new interesting insight in random lasers.

CHAPTER 7

Outlook and applications

Based on the work presented in this thesis, several ideas for new research directions and applications are put forward. Some of these ideas are based on the experimental techniques developed in this thesis, whereas others build upon the concept of studying a source inside a random medium. First, the technique used to unravel the spatial structure of random laser modes is shown to be a promising method for analyzing paint layers in greater detail in Sec. 7.1. Second, we propose an apparatus that measures the turbidity of suspensions by using the side imaging technique of *Chapter 4*. Third, a new line of research is suggested in Sec. 7.3 by combining random lasers with wavefront shaping. Fourth, in Sec. 7.4 studying sinks rather than sources in random media is discussed.

7.1 A new tool for studying paint

Characterization of multiple scattering media is of tremendous importance in the paint industry. The most expensive component in conventional paint is titania. Optimizing the hiding power of a paint, defined as "its ability to hide the color or color differences of a substrate" [208], while using as little pigment as possible therefore significantly reduces the paint's cost. For coating applications, the paint is also required to prevent exposure of the underlying material to its surroundings, *e.g.*, to make sure that no rust is formed in vulnerable parts of a ship. To analyze the quality of a coating, non-invasive techniques for studying the substrate while covered by the coating are needed. In this section, we introduce Frequency Correlation Imaging (FCI) as a new method for characterizing the opacity of paint. Moreover, this method is potentially able to reveal the structure of a multilayered paint sample and the optical properties of its substrate.

In passive random media, the scattering strength of samples is primarily characterized by angularly resolved techniques such as enhanced backscattering [53, 54] or total transmission and reflection measurements. The width of the enhanced backscattering cone is inversely

(a)

white light
excitation

spectrum

layer 1

layer 2

(b)

sample

objective

beam splitter

polarizer

polarizer

Fianium

EMCCD
camera

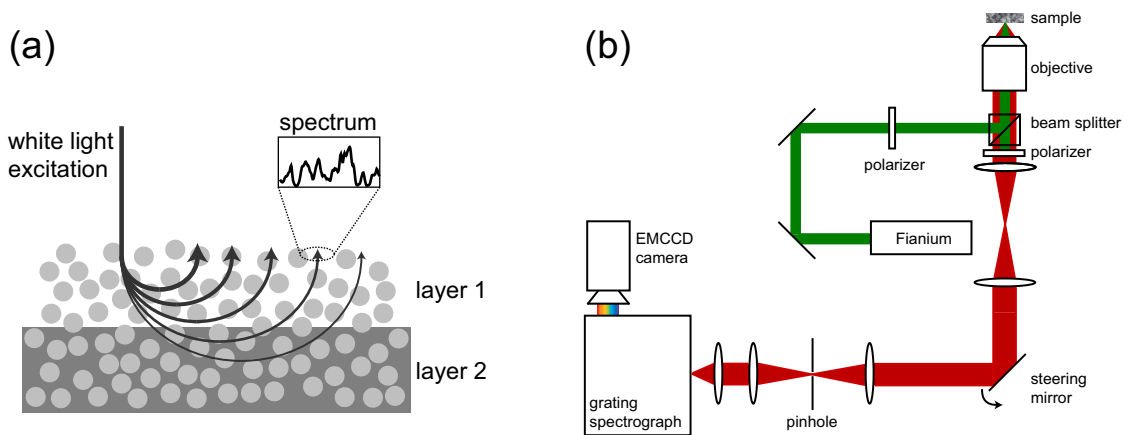steering
mirror

grating
spectrograph

pinhole

Figure 7.1: (a) Illustration of the principles behind Frequency Correlation Imaging. A paint sample is excited by coherent white light. Due to multiple scattering inside the sample, the excitation light diffuses away from the excitation focus. The average path length traversed in the sample is relatively short close to the focus of excitation and becomes longer when moving away from the focus. As a consequence, the spectral speckle collected far away from the focus contains information about light paths reaching deep into the sample. In this case, the spectral speckle collected far from the focus is influenced by another paint layer that is covered by the top layer. (b) Experimental realization of FCI technique.

proportional to the transport mean free path, which makes enhanced backscattering a great tool for studying strongly scattering samples. Information on long paths traversed in the sample accumulates in the tip of the cone, whereas the wings of the cone only convey information about the short paths traversed in the sample. Thus, enhanced backscattering is foremost a sensitive technique for studying short light paths. In the biomedical community, diffuse optical imaging [209] has proven to be a versatile tool for non-invasive imaging inside weakly scattering tissue, but its resolution has been limited to the centimeter scale. In *chapter 6*, a confocal detection scheme was introduced to measure the spatial structure associated with narrow spectral features in random lasers. The beauty of this technique resides in that it provides spatially resolved spectral information on the micrometer scale. At the same time, the advance of supercontinuum white-light laser technologies in the past decade allows for extending multiple scattering analyzing tools to a large range of wavelengths [59, 210].

The combination of excitation by a supercontinuum laser and spatially resolved spectral detection results in a powerful apparatus for analyzing paint samples. Figure 7.1 shows an illustration behind the idea of the FCI technique. Coherent white light generated by the supercontinuum laser (Fianium SC-450) is tightly focussed onto the surface of a paint sample. Multiple scattering results in diffusion of light. The diffuse light escaping the sample is collected in reflection. The average path length traversed through the sample depends on the distance between the point of excitation and the point of detection. Close to the focus, the average path length is short, whereas far away from the focus the average path length is long. This difference in path length changes the spectral intensity speckle. These changes in spectral speckle are measured by using our confocal detection scheme that allows for measuring the spectrum at different regions on the surface of the sample. Speckle due to long light paths in the sample decorrelates stronger than speckle due to short light paths, because the longer the traversed path in the medium the larger the phase
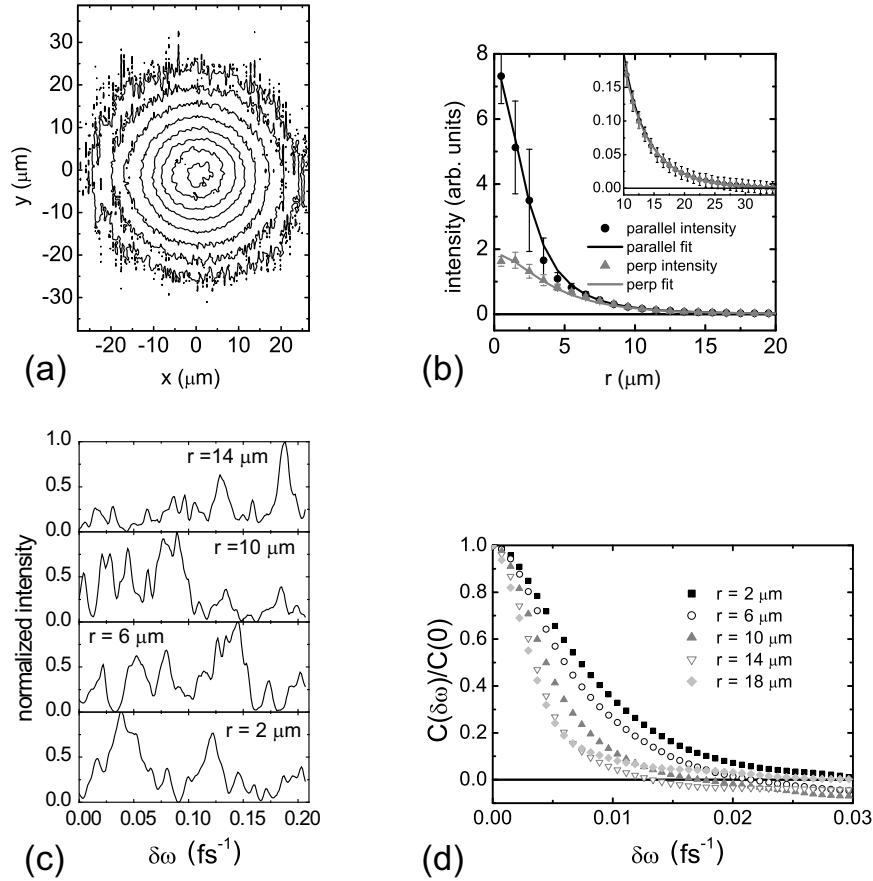
Figure 7.2: (a) Spectrally averaged contour plot of the diffuse spot measured in reflection. The contour lines are logarithmic. (b) Intensity versus radius for a diffuse spot in reflection. Black disks: experimental data points for parallel polarized light. Black line: fit to diffusion theory. Gray triangles: experimental data points for perpendicular polarized light. Gray line: fit to diffusion theory. (c) Experimental spectra around $\lambda = 604 \pm 25$ nm for different radii. (d) Experimental spectral intensity-intensity autocorrelation for different radii.

shift for a given frequency bandwidth. If long light paths are somehow attenuated, *e.g.*, by the presence of a hidden absorptive layer of paint, the correlation of the spectral speckle collected far away from the focus changes. The fact that FCI is both spectrally and spatially resolved then enables to find out which layers are hidden underneath the top layer.

Figure 7.2 shows some first results obtained with the FCI technique on a 14 ± 1 µm thick layer of dried white paint. The experimental apparatus that was used is sketched in Fig. 7.1(b). The spatial scan covered 54×77 microns and the spectrum was measured from 518 to 724 nm. In Fig. 7.2(a) the iso-intensity contour lines of the diffuse spot in reflection are shown. Spatial speckle has been averaged out by averaging over a frequency interval. The focus of the white-light light source is smaller than 2 µm. By fitting the diffuse spot profile with diffusion theory, as shown in Fig. 7.2(b), the transport mean free path ($\ell = 2 \pm 0.1$ µm), the extrapolation ratio ($z_e/\ell = 2.4$), and the absorption length ($\ell_a = 11 \pm 1$ µm) are retrieved. In addition, the spatial profile of the diffusive spot turns out to be strongly dependent on the measured polarization channel. Close to the focus of the white-light source, the intensity of the parallel polarization channel is higher than the perpendicular polarization channel due to a strong single scattering contribution. Far

Figure 7.3: Turbidimeter based on the method of extrapolation. Light from an incoherent light source is incident on a turbid sample. A detector placed at 90 degrees with respect to the incident beam forms a conventional nephelometer. This part of the apparatus is used to measure the turbidity of weakly scattering samples. For multiple scattering media (samples with high turbidity), the turbidity is measured by imaging the side of the sample onto a CCD camera. Extrapolation of the diffuse intensity to zero intensity, as illustrated in the graph, returns the extrapolation length indicated by the gray dot. From the extrapolation length the transport mean free path is deduced which is a direct measure for the turbidity of the sample.
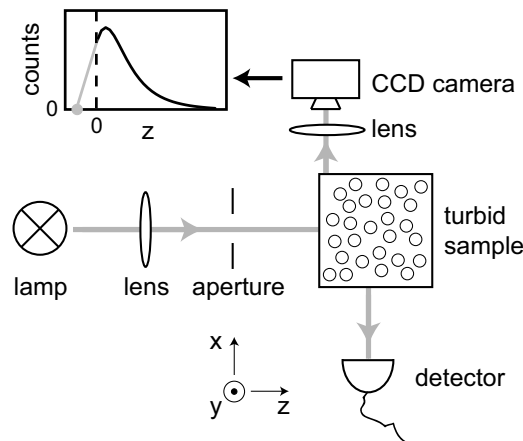
away from the focus, both polarization channels have equal intensity, because multiple scattering inside the sample scrambles the input polarization and thus results in a complete depolarization. Examples of measured spectra at different radii of the diffusive spot are shown in Fig. 7.2(c). Clear speckle intensity fluctuations are visible. By calculating the intensity-intensity spectral autocorrelation $C(\delta\omega)$ in Fig. 7.2(d), we conclude that the speckle indeed decorrelates faster on a spectral scale for larger radii.

These promising initial results show that FCI is a great way to characterize paint samples. In future experiments, the sensitivity of the technique to absorbing layers buried underneath a white paint layer needs to be investigated. The fact that our setup has a good signal-to-noise ratio for radii up to 15 times the transport mean free path indicates that the apparatus is capable of measuring effects of absorption on relatively long light paths. Depending on the sensitivity of the technique, FCI might even be able to recover images obscured by a white layer of paint, for example by performing the above mentioned experiment for different positions of the focus spot.

7.2 Turbidimeter based on the method of extrapolation

The clarity of liquids is often used as an indication for their quality. The industrial method for measuring the turbidity of suspensions relies on so-called nephelometers or turbidimeters. The measured turbidity is expressed in terms of the Nephelometric Turbidity Unit (NTU), which is a measure for the turbidity of the sample with respect to a standard solution of Formazin in water. The basic design of a nephelometer consists of an incoherent white light source and a detector placed at 90 degrees from the beam path that measures the light scattered out from a sample placed in the beam path. These type of nephelometers return accurate results for weakly scattering suspensions, but become useless for multiple scattering media. More complicated designs involving more than one detector exist that increase the turbidity range. Yet, dilution of samples remains required for strongly scattering samples [211, 212].

In the framework of this thesis the turbidity of a sample is expressed by the inverse of the transport mean free path rather than in terms of the NTU. These units are however in principle inversely proportional to each other. In *chapter 4*, we showed that knowledge of the extrapolation ratio and a side imaging technique enabled us to retrieve the transport mean path of a strongly scattering suspension. We propose a new type of turbidimeter based on this method of extrapolation that is able to measure both weakly and strongly scattering samples.

A sketch of the apparatus is shown in Fig. 7.3. The design is an extension to a conventional nephelometer, in which the diffuse intensity is imaged onto a CCD camera. By extrapolating the diffuse intensity at the edge of the sample to zero intensity, the extrapolation length is found. This extrapolation length is related to the transport mean free path via the extrapolation ratio. Since this ratio is well-known for water based suspensions in a cuvette, the transport mean free path can be deduced. The method of extrapolation is based on diffusion of light and is therefore limited to multiple scattering media. By combining this method with a conventional nephelometer however, a wide range of turbidity samples can be covered. This measurement device therefore reduces the need for dilution of samples.

7.3 Controlling random lasers by wavefront shaping

The spectral output of a random laser has been of the main topics in this thesis. Introducing an absorber was shown to lead to more control over the emission wavelength in *chapter 5*. Our approach of tuning a random laser by absorption has recently been extended to the domain of random lasers with narrow spectral features [213]. Yet, controlling the number and spectral position of these spikes in the spectrum has remained very much out of reach for experimentalists. We have seen in *chapter 6* that the spectral position of spikes is often chaotic and differs from shot-to-shot. The situation is remotely similar to ordinary speckle patterns where the spatial position of an intensity maximum is difficult to predict a priori. Wavefront shaping of the incident light, that is modulating the amplitude and phase profile of a plane wave, has led to incredible control over the scattered light from a passive random medium [36]. Here, we suggest that wavefront shaping the pump beam in a random laser enables engineering of the spectral narrow features in random lasers.

A sketch of the proposed experimental configuration is given in Fig. 7.4. Pump light is guided towards a spatial light modulator (SLM). Typically, a beam expander needs to be put in the beam path to match the size of the beam with the size of the SLM. The light reflected by the SLM is incident on a random laser sample. In wavefront shaping experiments, one either focusses the excitation light directly onto the sample or one images the separate SLM-pixels onto the surface of the sample [214]. The latter method has the advantage that it becomes possible to compare the wavefront shaping experiment with our work on the spatial structure of random laser modes in *chapter 6*, where we have measured the spatial distribution of emission light at the surface of the sample. The emission light is analyzed using a high-resolution spectrometer. Depending on the sample, spectral narrow features might appear in the emission spectrum. The spectral intensity of one of these features is selected by the experimenter as a feedback signal of the spatial light modulator. An optimization algorithm is then employed to modulate the amplitude and phase of the SLM, in order to increase the intensity of the selected feature in the spectrum.

Ideally, this pumping scheme leads to the enhancement of one of the narrow spectral

Figure 7.4: Sketch of experimental setup for wavefront shaping random lasers. The wave profile of the pump light (gray arrows) is modulated by a Spatial Light Modulator (SLM). The modulated phase front is projected onto the random laser sample. The emission light (dark gray arrows) is detected using a spectrometer. The intensity of a narrow spectral feature is used as a feedback signal for the amplitude and phase distribution on the SLM. An optimization algorithm is then employed to increase the signal of the selected narrow spectral feature.
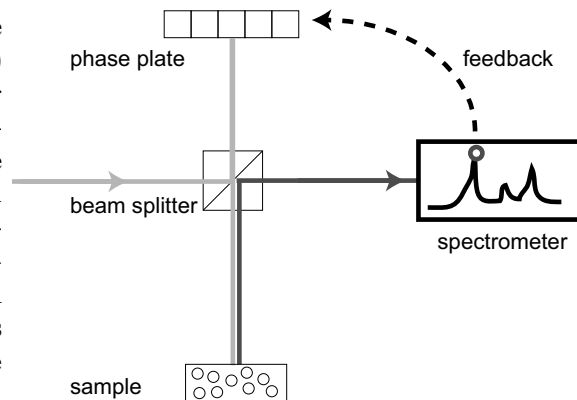
features at the cost of others and to an increased stability of random laser spectra. A serious complication is formed however by the fact that random laser spectra have the tendency to fluctuate strongly from shot-to-shot. These fluctuations stand in sharp contrast with wavefront shaping experiments in passive random media, where the used speckle patterns are stationary. To circumvent this complication, one might reduce the number of lasing modes from the start. For example, by using amplification of light by stimulated emission outside the gain medium [181, 193] or by taking only small samples into consideration [178]. After such a preselection of modes, averaging over multiple shots increases the output stability and hence the possible success rate of the optimization routine.

Our proposal for employing wavefront shaping in random lasers does not only lead to better control over the output of random lasers, it also promises to give more insight in the working principles behind a random laser. When the SLM is imaged onto the sample surface, the amplitude profile of the SLM after optimization corresponds with the excitation structure of a single random laser mode. Using our confocal detection scheme then allows for a direct comparison between the excitation and emission structure of a random laser mode. Moreover, a wavefront shaping experiment on a random laser sample very likely contains quantitative information about how much of the gain medium is shared between the different modes. To that end, the presence and intensity of narrow spectral features other than the one chosen for optimization need to be monitored as well. A complete suppression of the other spectral features is strong indication for little mode overlap inside the random laser sample. Successful implementation of the above brings random lasers closer to the realm of applications as it allows for the selection of a very narrow emission line at a random frequency.

7.4   Sinks in random media: the black shades of white

Researchers in the field of multiple scattering of light have shown a strong preference for nonabsorbing systems in the past [215]. This thesis considered systems in which radiation was not just conserved, but also created. We have seen how the interaction of sources with a multiple scattering random medium leads to fascinating phenomena such as random lasing and infinite range intensity correlations. The mathematical symmetry between gain and absorption has recently inspired a team of physicists to construct a so-called coherent

perfect absorber (CPA), in which interference of two coherent light beams results in almost complete (99 %) absorption of light in a slab of silicon [166, 167]. In essence, a CPA is the time-reversed analogy of a laser: in a conventional laser a standing wave pattern inside a leaky cavity filled with gain leads to the creation of coherent radiation outside the cavity; in a CPA two sided coherent illumination leads to a standing wave pattern in an absorbing cavity and subsequently to annihilation of the excitation light. The technique of CPA relies on resonances inside the cavity and the coherence of illumination. The technique is therefore intrinsically narrowband. A broadband strongly absorbing sample is one of the holy grail in the field of photovoltaics as such a material promises to drastically increase the efficiency of solar cells. Spherical scatterers placed on top of a silicon wafer show great potential for photovoltaic applications as they guide light into the wafer and thereby lead to enhanced absorption [216].

These studies illustrate how the focus in the field of nanophotonics is gradually enlarged towards including absorption. Three subjects follow naturally from the work described in this thesis when the role of sources is replaced by sinks. First, absorption might lead to intensity correlations that are similar to the ones as induced by a classical dipole source in a random medium. The source in the diagrammatic expression for the C_0-correlation is then replaced by an absorber located in close vicinity to a scatterer. In this view an absorbing particle is essentially a miniature version of a detector. If the analogy with the C_0-correlation holds, certain configurations of disorder lead to more extinction of incident light than others. In fact, in might well have been this C_0-correlation induced by absorption that has led to the observation of intensity fluctuations from a source in the literature [116]. Second, introducing local absorbers in our transverse localization experiment might enable a further selection of participating modes and thereby diminish the observed beating effects. Third, weakly absorbing random media might be made strongly absorbing when the amplitude and phase of the input light are altered using wavefront shaping. The feasibility of such an extension of CPA to the field of random media has recently been evaluated theoretically [217]. Our discovery that diffusion in random lasers make a multiple scattering medium act as an integrating sphere might be of use here since it reduces the need to shape the wavefront over a 4π solid angle.

Summary

This thesis deals with the interaction between sources of electromagnetic radiation and disordered photonic media. Three concepts arising from this interaction form its main thread. In the first concept, the combination of multiple scattering media with amplification of light by stimulated emission leads to random lasing. In the second concept, the excitation of a localizing random medium by a source enables the excitation of multiple eigenstates simultaneously. In the third concept, fluctuations in the local density of states influence the output of an embedded light source.

In the first chapter, an introduction into both electromagnetic sources and the theory of multiple scattering of waves is given that forms the framework for the remainder of the thesis. Diffusion is described using random walk arguments and a Green function formalism. Interference effects such as enhanced backscattering and Anderson localization are discussed. Speckle intensity correlations that are due to a source inside a random medium are reviewed as well as the field of amplifying random media.

The second chapter focusses on the role of the quantum efficiency in the outcome of photonic experiments involving molecular light sources. In the case of a unit quantum efficiency, every excited emitter will eventually send out electromagnetic radiation, whereas in the case of lower quantum efficiencies the sending out of radiation has to compete with nonradiative transitions. Changes in the local density of states or invoking stimulated emission of radiation, cause an increase in the power output of such a low quantum efficiency source. We argue that a random laser forms an excellent system to study the power balance of sources due to their omnidirectional output and the transition from spontaneous to stimulated emission as the main mechanism of radiation around the threshold. A random laser experiment with dye molecules with a range of quantum efficiencies, indeed illustrates that knowledge of the source is essential for correctly interpreting experimental results. With the help of an effective cavity model, the quantum efficiencies of the gain media are retrieved and analytic expressions for the threshold are given. It is shown that the theoretically derived infinite range intensity correlations rely on low quantum efficiency sources. For unit quantum efficiency sources, the calculations have to be extended to include sources with a constant power output.

In the third chapter, transverse localization of microwaves is studied with an excitation source in vicinity of the sample. This experimental scheme leads to the excitation of several eigenmodes simultaneously. The similarity of the paraxial wave equation describing our

experiment and the time dependent Schrödinger equation allows for a mapping of the longitudinal coordinate onto time. The waves are confined in the transverse dimension due to one-dimensional Anderson localization, but the superposition of eigenstates leads to beating effects in the longitudinal dimension.

The fourth and the fifth chapter treat some essentials of diffusive random lasers. First, the diffusive volume is shown to increase both experimentally by using a side imaging technique and numerically. This expansion in volume is a consequence of the fact that gain in a random laser compensates for diffusion, which acts as a loss term in the diffusive random laser rate equations. Absorption is another loss mechanism in random lasers, and by carefully engineering the amount of absorption at the emission frequency, control over the emission wavelength of random lasers becomes possible.

The field of random lasers has long been dominated by studies on narrow spectral features. Yet the community has not reached consensus on their origin. In chapter six, narrow spectral features are systematically studied both in samples with quenched disorder and in suspensions. Using a confocal detection apparatus, we are able to measure the spatial profile of random laser modes at the surface of a sample. The scattering and gain strength in a random laser are shown to be two crucial parameters in explaining the transition from smooth spectra to spectra containing narrow features experimentally. A model consisting of just two competing laser modes explains why in a diffusive sample emission spectra are smooth, whereas in weakly scattering samples narrow spectral features appear.

We conclude by discussing several new research directions and ideas for applying the used experimental techniques industrially in the seventh chapter. The combination of wavefront shaping with random lasers promises to yield interesting results in the future and unprecedented control over their spectral output. Our side imaging technique is put forward as a way to extend the scope of conventional turbidimeters. Confocal spectral detection and coherent white light excitation are shown to form a powerful couple that enables a full characterization of paint samples, and that can possibly reveal the layers hidden beneath an opaque layer of white paint.

Samenvatting

Elektromagnetische straling speelt een onmisbare rol in een mensenleven. Niet voor niets neemt de bekendste vorm van deze straling, zichtbaar licht, een zeer prominente en positieve plaats in bij beschavingen en in talen over de hele wereld. Tegelijkertijd zijn de technologische toepassingen van elektromagnetische straling niet meer weg te denken uit onze maatschappij. Mobiele telefonie, razendsnel internet, de magnetron, het zijn maar een paar voorbeelden van veelgebruikte toepassingen van dit soort straling.

Vanzelfsprekend is de opwekking van elektromagnetische straling dan ook van groot belang. De frequentie van de elektromagnetische velden bepaalt het type straling dat wordt gegenereerd. Microgolven, zoals gebruikt in een magnetron, kunnen worden gemaakt door antennes die elektrisch worden aangedreven. De frequentie van zichtbaar licht is daarentegen dusdanig hoog dat we het licht niet op een vergelijkbare wijze elektrisch kunnen opwekken. Om licht te maken zijn we daarom vaak afhankelijk van aangeslagen molekulen, dat wil zeggen molekulen in een hogere energietoestand, die hun overtollige energie kwijtraken door straling uit te zenden.

Het uitzenden van elektromagnetische straling door een molekuul gebeurt echter niet zomaar. Zonder een duwtje vanuit het elektromagnetische veld in de directe omgeving van het molekuul gebeurt er niets. Zelfs als het veld gemiddeld genomen nul is (we spreken dan van een elektromagnetisch vacuüm) vinden dit soort duwtjes plaats door fluctuaties in het veld. Deze zogeheten vacuümfluctuaties spelen een belangrijke rol in de natuurkunde. Als vacuümfluctuaties verantwoordelijk zijn voor de emissie van licht, dan zegt men dat het licht spontaan is uitgezonden. Licht kan ook worden uitgezonden door straling met precies de juiste frequentie op het molekuul te laten schijnen. Deze straling forceert het molekuul dan om uit zijn aangeslagen toestand te komen. Deze wijze van licht maken, wordt gestimuleerde emissie genoemd.

Dit proefschrift behandelt hoe lichtbronnen zich gedragen in ondoorzichtige materialen. Voorbeelden van ondoorzichtige materialen vinden we overal om ons heen. Denk bijvoorbeeld aan verf, melk of papier. Als licht binnentreedt in een dergelijke stof, dan raakt het al heel snel de weg kwijt. De deeltjes waaruit deze materialen zijn opgebouwd sturen het licht namelijk telkens een willekeurige richting op. Dit proces noemen we verstrooiing. In tegenstelling tot licht heeft verstrooiing een veel minder positieve connotatie in de meeste talen. Dat is ook niet zo vreemd, want verstrooiing leidt er vaak toe dat optische apparaten niet meer goed werken en dat je eigen zicht je ontnomen wordt. Een klein verstrooiend
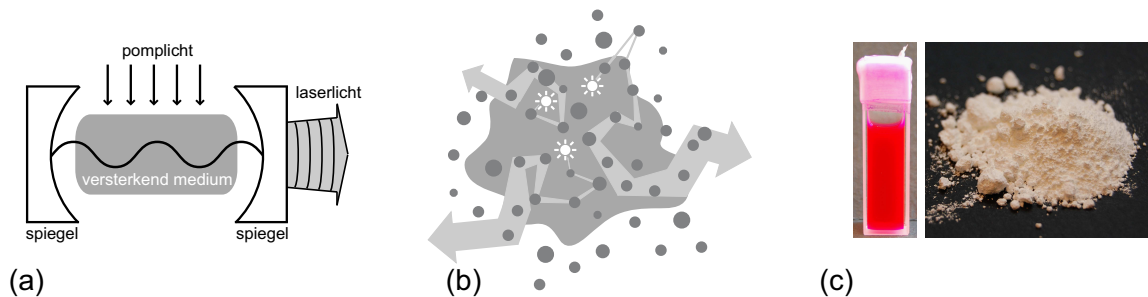
Figuur S.1: (a) Schematisch overzicht van een conventionele laser. Licht dat grotendeels opgesloten zit tussen twee spiegels wint aan intensiteit door de aanwezigheid van een gepompt versterkend medium. De rechterspiegel laat een klein beetje licht door: het laserlicht. (b) In een wanordelijke laser zorgt terugkoppeling middels verstrooiing voor een langere verblijftijd van licht in het versterkende medium. In tegenstelling tot een conventionele laser, gaat het laserlicht nu alle kanten op (grijze pijlen). (c) Hoofdbestanddelen van een typische wanordelijke laser: links het versterkende medium in de vorm van een kleurstof en rechts de verstrooiende deeltjes in de vorm van titania poeder.

vuiltje op de spiegel van een laser, kan er voor zorgen dat de laser in zijn geheel stopt met werken. De laatste decennia proberen verscheidene wetenschappers echter om verstrooiing tot een nieuwe bouwsteen te maken. In plaats van dat verstrooiing iets louter ongewenst is, blijkt het nu opeens een heel krachtig middel om optica robuuster te maken.

De wanordelijke lasers die uitvoerig behandeld worden in dit proefschrift zijn een duidelijk voorbeeld van deze verschuiving in het denken over verstrooiing. Een conventionele laser bestaat uit twee spiegels met daartussen een medium waarin licht wordt versterkt door gestimuleerde emissie. Figuur S.1(a) illustreert het werkingsprincipe van een dergelijke laser. Hoe meer energie er in het versterkende medium wordt gestopt door een pompmechanisme, hoe meer licht wordt versterkt door dit medium. De spiegels vormen een trilholte voor het licht waarin het licht als het ware gevangen zit. De combinatie van deze trilholte en het versterkende medium ertussen leidt tot een enorme hoeveelheid licht binnenin de laser. Doordat één van de spiegels een klein beetje transparant is gemaakt, ontsnapt er wat van dit licht naar buiten. Dit licht verandert van karakter naarmate er meer energie wordt gestopt in het versterkende medium. Boven de zogenaamde laserdrempel, krijgt het licht een zeer goed gedefinieerde kleur en vaak ook een goed gedefinieerde richting. Maar wat gebeurt er nu als de spiegels worden vervangen door verstrooiende deeltjes, met andere worden als die vervelende stofdeeltjes een essentieel onderdeel worden van de laser? Het blijkt dat er dan ook een laser ontstaat. Karakteristieke eigenschappen van een normale laser zijn ook zichtbaar in deze vertrooiende laser, zoals het ontstaan van een heldere kleur boven de laserdrempel.

Als de verstrooiing binnen zo een wanordelijke laser sterk genoeg is, ontstaat er echter wel een belangrijk verschil. Waar in een normale laser het licht een heel duidelijke richting heeft, gaat in een wanordelijke laser het licht alle kanten op. In Figuur S.1(b) staat schematisch weergegeven hoe zo een wanordelijke laser werkt, in Figuur S.1(c) staan de belangrijkste ingrediënten van een dergelijke laser naast elkaar: het versterkingsmedium en de verstrooiers. In hoofdstuk 2 van dit proefschrift, wordt zowel experimenteel als theoretisch aangetoond hoe deze bijzondere eigenschap ons in staat stelt om meer te weten te komen over de lichtbronnen die het versterkend medium vormen. De resultaten van een experiment blijken erg afhankelijk van het type lichtbron dat wordt gebruikt. Deze afhankelijkheid blijkt daarnaast grotendeels genegeerd te zijn in de theoretische verstrooiings-

literatuur. Sommige type lichtbronnen blijken onafhankelijk voor optische veranderingen in de directe omgeving, terwijl andere lichtbronnen veel meer licht gaan uitzenden als de hoeveelheid vacuümfluctuaties of de hoeveelheid invallende straling verandert.

De verspreiding van licht in verstrooiende materialen kan meestal zeer goed worden beschreven met behulp van diffusietheorie. Licht spreidt zich dan op een vergelijkbare manier uit als de inkt die uitloopt van een vulpen op een poreus papiertje. In tegenstelling tot deze inkt is licht echter een golf. Als twee golven elkaar tegenkomen kunnen ze elkaar uitdoven of versterken, dit wordt interferentie genoemd. Als dit fenomeen in verstrooiende media erg dominant wordt, kan het er voor zorgen dat de diffusie beschrijving niet meer correct is. In lager dimensionele systemen zorgt interferentie ervoor dat het licht gelokaliseerd wordt in plaats van diffuus uitspreidt. In het derde hoofdstuk van dit proefschrift laten we zien hoe lokalisatie zich opbouwt in de tijd met behulp van microgolven. Als de straling afkomstig is van een kleine bron, ontstaan er allerlei oscillaties in de lokalisatiepatronen.

In hoofdstuk vier, wordt diffusietheorie juist gebruikt om de transport van licht in een wanordelijke laser te begrijpen. Met behulp van een nieuwe meetmethode wordt een vergroting van het emissievolume waargenomen. Deze vergroting staat aan de basis van een goed begrip van de resultaten in hoofdstuk vijf, waar we de kleur van een wanordelijke laser laten veranderen door een stofje toe te voegen die bepaalde kleuren absorbeert.

In het vakgebied van wanordelijke lasers is er veel discussie over resultaten waarin heel goed gedefinieerde kleuren tegelijkertijd worden waargenomen. Door al deze resultaten te ordenen en nieuwe experimenten uit te voeren komen we tot de ontdekking dat de verstrooiingsterkte en de mate van versterking bepalen hoe een wanordelijke laser zich gedraagt. Hoe diffuser de wanordelijke laser is, hoe voorspelbaarder het spectrum er uit zal zien.

Hoewel het proefschrift behoorlijk fundamenteel van aard is, blijken er ook interessante mogelijkheden te zijn om enkele van de experimentele opstellingen te gebruiken in een industriële context. Deze toepassingen staan centraal in het laatste hoofdstuk. De ontwikkelde opstellingen in dit proefschrift leiden mogelijk tot een betere karakterisering van lagen verf en troebele suspensies.

Context of discovery: a behind-the-scenes story of a thesis

Wat is wetenschap? Wetenschap is de titanische poging van het menselijk intellect zich uit zijn kosmische isolement te verlossen door te begrijpen.

W. F. Hermans, *Nooit meer slapen* (1966)

Science is much more than the collection of scholarly articles, theses, and books. One might give very different answers to the question what science entails depending on one's viewpoint. Philosophers of science often make a useful distinction between the "context of justification" and the "context of discovery" when analyzing science. The "context of justification" refers to the rational arguments put forward by scientists that explain why their research belongs to the body of scientific reasoning. The backgrounds of a study, *e.g.*, questions related to why studies are conducted or where a scientist received inspiration for his work, fall within the "context of discovery" [218]. A thesis in physics is mostly written and judged within the "context of justification". In this section, which does not belong to the academic part of my thesis, I sidetrack a little bit and I describe how scientific research comes into being from the perspective of a graduate student.

The contents of a dissertation in the natural sciences can often only be grasped by a small group of specialized scholars. I am afraid my thesis forms no exception to that rule. For the uninitiated the text of a dissertation is too technical and if it contains a lot of mathematics it might even appear mysterious. A popular saying among physics PhD students goes that the *Acknowledgments* form by far the most important part of a thesis, simply because it is the only part understandable to everyone. Similarly, the structure and style of scientific articles barely reflect the moments of glory and excitation every scientist feels when making a new discovery. For outsiders, these technical and dry pieces of communication are doomed to remain unattractive prose. For insiders, these texts written in broken English enriched with loads of formulas and graphs possibly reveal beautiful new aspects of nature.

In her 2009 *Jan Hanlo*-lecture [219] Marita Mathijsen, professor in Dutch literature at the University of Amsterdam, encouraged to introduce all kinds of literary techniques, such as emotion and rhetoric devices, into scientific texts in order to make works of science accessible to a larger audience. This lecture led to vivid discussions in our own laboratory

and culminated in an exchange of ideas between Marita Mathijsen and my promotor Ad Lagendijk in the Dutch daily *NRC Handelsblad* [220].

To a large extent the difference of opinion originated from alternative interpretations of what scientific texts are about. Natural scientists are trained to write their reports in a factual and logical manner. Phrases, graphs, and formulas are constructed with utmost care to make sure ambiguity is minimized. The reports on their discoveries are primarily aimed at justifying and placing their newly found knowledge into the existing framework of science. The bulk of scientific literature deals with this so-called "context of justification". By focussing on the context of justification, scientists leave out a lot of interesting information about the backgrounds of their study that describe *how* a piece of science comes into existence. For example, from reading a scientific article in a specialized journal it is very hard to understand why a particular study was conducted by scientist A or B in the first place and how and where he conceived the idea for doing so. Analyzing these backgrounds is done in the "context of discovery" [218]. In contrast to reports dealing with the context of discovery, the very nature of reports written in the context of justification does not allow for a lot of flexibility in the way a text is written[1]. Mathijsen's plea for using literary techniques boils down to incorporating more context of discovery elements into scientific correspondence.

The central part of my dissertation, namely the numbered chapters, are written in the context of justification. In this section however, I want to focus on the context of discovery of some parts of my thesis. My aim is thus to give the reader some insights in how experimental science unfolds in practice. More importantly, I hope to show what has motivated me as a PhD student. As a consequence, this section is free of formulas and mind boggling graphs, and I have tried to use as little scientific jargon as possible. Every now and then I allow myself to employ rhetorical techniques to increase readability.

Conceiving ideas: a bike ride to the rescue

What to do in four years? Part of the fun of doing a PhD is that you do not have a clear answer to that question. Most graduate students in physics start off their PhD period with a project that is thought of by one of their supervisors. Yet a lot of them end up doing something else in the end. In fact, eventually a PhD student is required to be able to perform research independently which, in my opinion, includes the generation of new ideas. Unfortunately, good ideas for new experiments do not pop up out of nothing.

Paradoxically, not understanding something completely might help in getting on the right track. After all, if you think you understand it all, then there is not much left to find out. One of the fascinating topics that stayed somewhat of a mystery for me for a long time, concerned the behavior of a minuscule light source embedded in a strongly scattering medium. I heard post-docs and professors talking about it, but reading the original theoretical paper on the subject [51] did not help in gaining a better understanding. The article was full of mathematical diagrams and terminology I had never heard of during my studies. I put the subject to rest and focussed on the topic of my Master's thesis instead. A talk by my supervisor during one of our meetings with the Complex Photonics Systems (COPS) group on the third of October 2008 reignited my curiosity on the subject.

---

[1]Although the distinction between the context of discovery and justification is not always straightforward to make [221], I do think the distinction describes quite accurately the difference between what we read in the scientific literature and the day-to-day experience in the lab.

Theoreticians in multiple scattering media completely overlooked the fact that how much comes out of a light source does not only depend on its optical environment, but also on the type of source that is used. His remarks were in complete disagreement with the theoretical paper I had failed to understand initially.

Intrigued by my advisor's talk I started thinking about an experiment that could reveal the consequences of having different light sources in experiment. I presented an experimental scheme to measure the power balance of sources in random media at one of the brainstorming sessions in our group Photon Scattering in March 2010. The scheme was based on integrating spheres. These hollow spheres typically have a diameter of 10 centimeters and are either coated with white powder or a thin layer of gold. They are often used to measure the total transmitted light through a sample and I thought they would be great instruments for measuring the total emitted power by a light source. One of my senior colleagues Patrick Johnson immediately remarked that this experiment was going to be much harder than I thought. Nevertheless I decided to give it a try. Based on chemical literature I selected some molecular light sources with beautiful names like Rose Bengale and Nile Blue that were suited for the experiment.

After several days of stubbornly trying out the experiment, I concluded however that Patrick's experience had overruled my naive enthusiasm. There was no way I could make sure that what I measured probed the total emitted intensity. I felt disappointed and was about to return to the subject of random lasers with which I was more acquainted. The cloudbursts that tempered Amsterdam those days did not help in improving my mood either. Naturally, I was already thinking what new random laser experiments to do. During my bike ride home, while getting soaking wet, I suddenly realized that a random laser experiment with different type of sources would be a great way to prove my supervisor's point. Multiple scattering inside the sample would mimic an integrating sphere. This realization was a thrilling experience. In the next month I conducted random laser experiments, which indeed showed the behavior I expected and eventually led to the work described in *chapter 2* of this thesis.

The importance of group discussions and meetings in generating ideas can hardly be overestimated. The third chapter of my thesis followed from a group talk given by fellow PhD student and dear friend Sanli Faez. In his quest for measuring Anderson localization with electromagnetic waves, he had decided to move from light to microwaves. Working with microwaves has two distinct advantages in photonics. First, photonic structures in the microwave regime are on the order of centimeters, which means you can just use a pair of scissors and scotch tape to create your samples. So whereas in optics the radiation is visible, while the sample structure is not, it is precisely the other way around in microwaves: the radiation is invisible, but you do not need a fancy electron microscope to study the spatial structure of the sample. Second, in this wavelength range, materials show a much larger spread in refractive index. I wondered what other types of experiments would be feasible and interesting with this new equipment, so I asked Sanli: why not look at a related phenomenon, namely transverse localization, as well? This topic was very much in fashion at that time due to the fact that some first claims were made regarding its observation. Ad, Sanli, and I were convinced that new physics would arise when studying it in more detail. A new project was born.

Another source of inspiration is of course formed by the scientific literature that is already out there. Unfortunately, staying up to date with the literature has become quite a struggle. The number of interesting articles that appear in scientific journals has grown

tremendously. Moreover, the number of journals that might publish relevant work has also grown in recent years. For example the *Nature Publishing Group* has launched at least five journals that are of interest to my community since 2002. It is therefore nearly impossible to read and understand every article in your field from top to bottom. Still, reading articles can be a great way for getting new ideas, because those articles often approach the field under a slightly different angle. Combined with you own knowledge, this angle might just be what is needed to create an insight.

Such an insight occurred to me while I was carefully reading a paper in which the output color of a random laser was manipulated [156]. I liked the paper a lot, because normally the color that comes out of a random laser is beyond control. To induce a preference for a certain color, the authors had made multiple scattering media out of spherical particles with a fixed size. As a consequence some colors remain longer inside the medium than others, and these are then the colors that are generated inside the laser. The formula on which their work was based, was very familiar to me, yet I kept staring at it for minutes. Out of experimental experience and by reading the thesis of Gijs van Soest [89] over and over again, I knew that the color of a random laser changes due to reabsorption. To my surprise, there was however no absorption term in the equations of the paper. Clearly, by engineering the absorption inside the sample, the output color should become tunable as well. I ordered a suitable absorbing material named Quinaldine Blue and about two weeks later the first tuning effects became apparent in experiment.

Experiments: when the unexpected becomes the subject

Not every experiment however turns into a success that easily. Unforeseen effects can either be exciting or a nuisance, but in both cases they require extra work and cause sleepless nights for the researcher. After all, unwanted "trivial" artifacts such as spurious reflections or fluorescence from a host medium are not particularly exciting.

While doing the microwave experiment on transverse localization I thought I encountered precisely such an annoying side effect. The experiment consisted of a lot of nylon bars placed parallel to each other. These nylon bars were supposed to interact with the microwaves in such a way that the wave remained confined and would not spread out in all directions. The experimental results indeed showed this localizing behavior when we studied an ensemble of samples. So far so good: Ad, Sanli, and I were proud of these first results.

But when the initial position of the wave changed in one single sample, the confined output moved in exactly the opposite direction. This observation puzzled us, and for a long time we thought that the detectors were somehow interfering with the phenomenon we aimed to observe. In a somewhat naive moment I decided to remove one of the copper plates covering the sample to see whether we could measure the wave intensity inside the sample. Nobody of us believed this approach would work, because the job of the copper plate was to reduce the losses in the system. Removing the plate, we thought, would lead to a dramatic increase in loss thereby possibly killing the whole effect we were after. Surprise, surprise, it worked. The losses were lower than anticipated due to waveguiding in the nylon itself. Not only remained the localizing behavior intact, clear oscillations in wave intensity were revealed as well.

So the next question cropped up: what on earth were these oscillations? The data was very convincing, so there was no real need for new experiments. I focussed instead

on modeling the system. At first I solved the relevant equations by a brute force method, which worked but did not give me any real insight. The equations were very similar to Schrödinger's equation, one of the iconic equations in quantum mechanics. I knew quantum mechanics from my undergraduate courses, but my knowledge had become a little rusty over the years. I redid some exercises that I did in my second year at the University of Twente. The answer was to be found in one of the first chapters, where it was explained in an exercise how adding up several of the system's characteristic states leads to oscillations. I calculated these characteristic states for my samples and indeed the wave oscillated in exactly the same manner as it did in experiment.

A little understanding

For me, the thrill of seeing one's own model in agreement with one's own experimental data, is only rivalled by seeing a sought after experimental effect for the first time. Together they make up for all hours in the lab when things did not work as planned and for all hours spent behind the desk when integrals, impossible equations, and crashing computers test your patience to the maximum. At first glance, it appears that understanding a problem in physics comes down to understanding the maths that describes the phenomenon. The maths can however easily get out of control and although a numerical solution probably yields the correct answer, it does not necessarily lead to understanding. Playing with the input parameters increases the insight obtained with numerics somewhat, but the risk of playing with parameters for weeks without significant progress is a serious danger.

Due to these limitations of numerical calculations, simple, approximate analytical solutions are very much preferred in our group. Sanli referred to this preference explicitly when I showed my first results on light sources and random lasers. He was impressed by the experimental data, but believed an analytical model would be much more powerful than the numerical solution I had presented. He was right. Later on, our analytical expressions showed directly how light sources influence the outcome of the experiments. It still amazes me that our experiments are encapsulated in an expression containing just a handful of characters. All of a sudden, you find yourself with one line that describes the essence of an experiment. To experience such beauty, is the pleasure of doing natural science.

Dankwoord

Mijn proefschrift had nooit tot stand kunnen komen zonder de oprechte ondersteuning op zowel wetenschappelijk als sociaal vlak van vele mensen. Ik zou hier graag de bijdragen van sommigen nader willen toelichten.

Allereerst wil ik mijn promotor Ad Lagendijk danken voor vele inspirerende gesprekken. Of deze discussies nou gingen over wetenschap, maatschappij of technologie, ze leiden altijd tot een heel vruchtbare uitwisseling van ideeën. Ook wil ik je in het bijzonder bedanken voor het expliciet uitspreken van jouw begrip en vertrouwen in het eerste wat turbulentere jaar van mijn promotieperiode.

De groep waar ik deel van uit maakte, Photon Scattering, bestaat uit kleurrijke karakters. Allemaal zijn ze behoorlijk eigenwijs, koppig, maar bovenal nieuwsgierig. De werkbesprekingen en lunches zijn voor buitenstaanders wellicht onnavolgbaar, maar ik zal ze zeker gaan missen. Waar hebben we het eigenlijk niet over gehad? Bergin, Patrick, Jochen, Paolo, Timmo, Otto, Mohamed, Ronald, Sanli: het was een genoegen om met jullie te mogen samenwerken. Otto, jouw enthousiasme voor onderzoek is een belangrijke drijfveer voor mij geweest om te gaan promoveren. Dank. Ronald, mede dankzij jouw toewijding is het zesde hoofdstuk een compleet verhaal geworden, heel veel dank daarvoor. Sanli, jij was vanaf het eerste project in Twente een dierbare vriend, kameraad en inspiratiebron. Daarnaast ben ik heel trots op het wetenschappelijk werk dat we samen hebben uitgevoerd.

Ontmoetingen met andere wetenschappers zijn essentieel voor een promovendus. De COPS en center for nanophotonics bijeenkomsten waren voor mij dan ook onmisbaar. Het machismo gehalte van beide bijeenkomsten is wellicht wat afgenomen met de jaren, maar de goede inhoudelijke discussies zijn er niet minder op geworden. Dank allen voor de nuttige terugkoppeling op mijn werk. Allard, jouw wetenschappelijke ingevingen zijn vaak bijzonder origineel. Onze discussies over random lasers waren bovendien heel erg productief. Het was een genoegen om met je samen te werken. Willem, ik heb onze gesprekken sinds mijn komst bij COPS altijd erg gewaardeerd. Ik hoop dat de band tussen de oud COPS leden nog lang sterk zal blijven.

Tijdens mijn tijd op AMOLF heb ik me altijd omringd geweten door fantastische kamergenoten. Aan Bart en Merel in kamer 1.39 in het oude gebouw, en aan Ernst-Jan, Paolo, Yichen, Grzegorz en Benjamin in 2.51 in het nieuwe gebouw, ben ik dan ook veel dank verschuldigd. Menigmaal werd de vrijdagmiddag gelukkig gebruikt om het over andere zaken dan wetenschap te hebben.

Tot slot zijn er mijn vrienden en familie die mij zo lief zijn en ik zeker niet mag vergeten. Ik voel me gezegend met de vele bijzondere vriendschappen die zijn voortgekomen uit mijn middelbare school periode, mijn Enschedese studententijd en mijn Amsterdamse jaren. Samen zorgden jullie voor de nodige ontspanning op de juiste momenten. Dardiry gatherings, whether in Alexandria, Cairo, Amsterdam, or San Fransisco, are legendary by definition. My Dutch and Egyptian family share their love for food, life, and openness. De familie Bogaers is onderscheidend door haar verscheidenheid. Wat is het heerlijk om dat in één familie bij elkaar te hebben. In Amsterdam, is het altijd een groot plezier om bij Ruud en Betty te zijn, jullie gastvrijheid is weergaloos. Met Felix en Yousef heb ik ongetwijfeld de meeste tijd doorgebracht in Amsterdam. Onze lach is daarbij ons gedeelde wapen. Ik ben er trots op dat jullie mijn paranimfen zijn. Timor, jouw inzichten in werk, relaties, schrijven, reizen en muziek laten me altijd weer net wat verder kijken. Veel van mijn ontdekkingen heb ik dan ook aan jou te danken. Ik hoop dat we snel weer een mooi stuk schrijven samen. Dankzij de rust, het vertrouwen en de liefde van mijn ouders kan ik de wereld beetje bij beetje verkennen. Mama, misschien begrijp je niet veel van dit proefschrift, je begrijpt wel heel goed waarom ik het geschreven heb. Papa, mijn wetenschappelijke reis begon bij jou met 3-4-5 en eerst denken dan doen. Duizendmaal dank. Het grootste geluk ontdekte ik op AMOLF met Ramses Shaffy aan mijn zijde: Laila, met dat ene lied in ons achterhoofd is het leven samen een groot plezier.

Bibliography

[1] C. Huygens, *Traité de la lumière*, Pierre van der Aa, Leiden (1690). — p.9.

[2] C. Huygens and S. P. Thompson (trans.), *Treatise on light*, University of Chicago Press, Chicago (1945). — p.9.

[3] G. R. Fowles, *Introduction to modern optics*, Dover publications, New York (1975). — p.10 and 16.

[4] A. G. Curto, G. Volpe, T. H. Taminiau, M. P. Kreuzer, R. Quidant, and N. F. van Hulst, "Unidirectional emission of a quantum dot coupled to a nanoantenna", *Science* **329**, 930 (2010). — p.10.

[5] L. Novotny and N. F. van Hulst, "Antennas for light", *Nat. Photon.* **5**, 83 (2011). — p.10.

[6] T. Coenen, E. J. R. Vesseur, A. Polman, and A. F. Koenderink, "Directional emission from plasmonic Yagi-Uda antennas probed by angle-resolved cathodoluminescence", *Nano Lett.* **11**, 3779 (2011). — p.10.

[7] N. I. Zheludev, "What diffraction limit?", *Nat. Mater.* **7**, 420 (2008). — p.10.

[8] J. B. Pendry, "Negative refraction makes a perfect lens", *Phys. Rev. Lett.* **85**, 3966 (2000). — p.10.

[9] V. M. Shalaev, "Optical negative-index metamaterials", *Nat. Photon.* **1**, 41 (2007). — p.10.

[10] N. Engheta, "Circuits with light at nanoscales: Optical nanocircuits inspired by metamaterials", *Science* **317**, 1698 (2007). — p.10.

[11] A. Lagendijk and B. A. van Tiggelen, "Resonant multiple scattering of light", *Phys. Rep.* **270**, 143 (1996). — p.10, 18, and 28.

[12] D. J. Griffiths, *Introduction to electrodynamics*, Prentice Hall, New Jersey (1999). — p.11.

[13] C. F. Bohren and D. R. Huffman, *Absorption and scattering of light by small particles*, Wiley Interscience (1983). — p.12, 19, 20, and 28.

[14] M. Tonouchi, "Cutting-edge TeraHertz technology", *Nat. Photon.* **1**, 97 (2007). — p.13.

[15] A. Siegman, *Lasers*, University Science Books (1986). — p.13, 14, 15, 17, 36, 39, 68, 88, and 93.

[16] O. Svelto, *Principles of Lasers*, Plenum Press (1998). — p.13, 14, 34, and 64.

[17] G. C. Gerry and P. L. Knight, *Introductory quantum optics*, Cambridge University

Press (2004). — p.13.

[18] E. M. Purcell, "Spontaneous emission probabilities at radio frequencies", *Phys. Rev.* **69**, 674 (1946). — p.13.

[19] K. H. Drexhage, "Interaction of light with monomolecular dye layers", *Prog. Optics* **12**, 165 (1974). — p.14.

[20] W. L. Barnes, "Fluorescence near interfaces: the role of photonic mode density", *J. Mod. Opt.* **45**, 661 (1998). — p.14.

[21] M. D. Leistikow, A. P. Mosk, E. Yeganegi, S. R. Huisman, A. Lagendijk, and W. L. Vos, "Inhibited spontaneous emission of quantum dots observed in a 3d photonic band gap", *Phys. Rev. Lett.* **107**, 193903 (2011). — p.14.

[22] P. A. Lynn, *The analysis and processing of signals*, MacMillan Press, London (1989). — p.15.

[23] N. J. Turro, *Molecular photochemistry*, W. A. Benjamin, New York (1967). — p.15.

[24] I. S. Nikolaev, P. Lodahl, and W. L. Vos, "Fluorescence lifetime of emitters with broad homogeneous linewidths modified in opal photonic crystals", *J. Phys. Chem. C* **112**, 7250 (2008). — p.15.

[25] J. P. Gordon, H. J. Zeiger, and C. H. Townes, "The maser - new type of microwave amplifier, frequency standard, and spectrometer", *Phys. Rev.* **99**, 1264 (1955). — p.16.

[26] T. H. Maiman, "Stimulated optical radiation in ruby", *Nature* **167**, 493 (1960). — p.16.

[27] M. O. Scully and M. Fleischhauer, "Lasers without inversion", *Science* **21**, 337 (1994). — p.16.

[28] H. C. van de Hulst, *Light scattering by small particles*, Dover publications (1957). — p.18, 19, 20, 28, and 70.

[29] A. F. Koenderink and W. L. Vos, "Light exiting from real photonic band gap crystals is diffuse and strongly directional", *Phys. Rev. Lett.* **91**, 213902 (2003). — p.18.

[30] A. F. Koenderink, A. Lagendijk, and W. L. Vos, "Optical extinction due to intrinsic structural variations of photonic crystals", *Phys. Rev. B* **72**, 153102 (2005). — p.18.

[31] M. V. Gorkunov, S. A. Gredeskul, I. V. Shadrivov, and Y. S. Kivshar, "Effect of microscopic disorder on magnetic properties of metamaterials", *Phys. Rev. E* **73**, 056605 (2006). — p.18.

[32] J. Gollub, T. Hand, S. Sajuyigbe, S. Mendonca, S. Cummer, and D. R. Smith, "Characterizing the effects of disorder in metamaterial structures", *Appl. Phys. Lett.* **91**, 162907 (2007). — p.18.

[33] L. Sapienza, H. Thyrrestrup, S. Stobbe, P. D. Garcia, S. Smolka, and P. Lodahl, "Cavity quantum electrodynamics with Anderson-localized modes", *Science* **327**, 1352 (2010). — p.18, 33, 59, and 70.

[34] T. Schwartz, G. Bartal, S. Fishman, and M. Segev, "Transport and Anderson localization in disordered two-dimensional photonic lattices", *Nature* **446**, 52 (2007). — p.18 and 50.

[35] G. Lerosey, J. de Rosney, A. Tourin, and M. Fink, "Focussing beyond the diffraction limit with far-field time reversal", *Science* **315**, 1120 (2007). — p.18.

[36] I. M. Vellekoop and A. P. Mosk, "Focusing coherent light through opaque strongly scattering media", *Opt. Lett.* **32**, 2309 (2007). — p.18 and 101.

[37] I. M. Vellekoop, A. Lagendijk, and A. P. Mosk, "Exploiting disorder for perfect focusing", *Nat. Photon.* **4**, 320 (2010). — p.18 and 70.

[38] I. M. Vellekoop, E. G. van Putten, A. Lagendijk, and A. P. Mosk, "Demixing light paths inside disordered metamaterials", *Opt. Express* **16**, 67 (2008). — p.18.

[39] E. G. van Putten, D. Akbulut, J. Bertolotti, W. L. Vos, A. Lagendijk, and A. P. Mosk, "Scattering lens resolves sub-100 nm structures with visible light", *Phys. Rev. Lett.* **106**, 193905 (2011). — p.18.

[40] S. M. Popoff, G. Lerosey, R. Carminati, M. Fink, A. C. Boccara, and S. Gigan, "Measuring the transmission matrix in optics: An approach to the study and control of light propagation in disordered media", *Phys. Rev. Lett.* **104**, 100601 (2010). — p.18.

[41] A. Taflove and S. C. Hagness, *Computational Electrodynamics: The Finite-Difference Time-Domain Method*, Artech House (2005). — p.18.

[42] G. Mie, "Beiträge zur optik trüber medien, speziell kolloidaler metallösungen", *Ann. Phys.* **330**, 377 (1908). — p.20.

[43] B. D. Hughes, *Random walks and random environments*, Oxford science publications, New York (1995). — p.21 and 22.

[44] H. C. Berg, *Random walks in biology*, Princeton University Press (1993). — p.21.

[45] H. S. Carslaw and J. C. Jaeger, *Conduction of Heat in Solids*, Oxford University Press (1986). — p.22.

[46] P. H. Cootner (Ed.), *The Random Character of Stock Market Prices*, Risk Publications (2000). — p.22.

[47] M. Born and E. Wolf, *Principles of Optics: Electromagnetic Theory of Propagation, Interference and Diffraction of Light*, Cambridge University Press (1997). — p.22.

[48] M. C. W. van Rossum and T. M. Nieuwenhuizen, "Multiple scattering of classical waves: microscopy, mesoscopy, and diffusion", *Rev. Mod. Phys.* **71**, 313 (1999). — p.23 and 30.

[49] M. B. van der Mark, M. P. van Albada, and A. Lagendijk, "Light scattering in strongly scattering media: Multiple scattering and weak localization", *Phys. Rev. B* **37**, 3575 (1988). — p.23.

[50] J. F. de Boer, *Optical fluctuations on the tranmsission and reflection of mesoscopic systems.*, Ph.D. thesis, University of Amsterdam (1995). — p.23.

[51] B. Shapiro, "New type of intensity correlation in random media", *Phys. Rev. Lett.* **83**, 4733 (1999). — p.26, 30, 47, 59, and 112.

[52] M. P. van Albada, B. A. van Tiggelen, A. Lagendijk, and A. Tip, "Speed of propagation of classical waves in strongly scattering media", *Phys. Rev. Lett.* **66**, 3132 (1991). — p.27.

[53] M. P. van Albeda and A. Lagendijk, "Observation of weak localization of light in a random medium", *Phys. Rev. Lett.* **55**, 2692 (1985). — p.28, 80, and 97.

[54] P.-E. Wolf and G. Maret, "Weak localization and coherent backscattering of photons in disordered media", *Phys. Rev. Lett.* **55**, 2696 (1985). — p.28, 80, and 97.

[55] A. Tourin, A. Derode, P. Roux, B. A. van Tiggelen, and M. Fink, "Time-dependent coherent backscattering of acoustic waves", *Phys. Rev. Lett.* **79**, 3637 (1997). — p.28.

[56] G. Labeyrie, F. de Tomasi, J.-C. Bernard, C. A. Müller, C. Miniatura, and R. Kaiser, "Coherent backscattering of light by cold atoms", *Phys. Rev. Lett.*

83, 5266 (1999). — p.28.

[57] E. Akkermans, P. E. Wolf, and R. Maynard, "Coherent backscattering of light by disordered media: Analysis of the peak line shape", *Phys. Rev. Lett.* **56**, 1471 (1986). — p.28.

[58] Y. L. Kim, V. M. Turzhitsky, Y. Liu, H. K. Roy, R. K. Wali, H. Subramanian, P. Pradhan, and V. Backman, "Low-coherence enhanced backscattering: review of principles and applications for colon cancer screening", *J. Biomed. Opt.* **11**, 041125 (2006). — p.28.

[59] O. L. Muskens and A. Lagendijk, "Broadband enhanced backscattering spectroscopy of strongly scattering media", *Opt. Express* **16**, 1222 (2008). — p.28, 61, and 98.

[60] C. M. Aegerter and G. Maret, "Coherent backscattering and Anderson localization of light", *Prog. Optics* **52**, 1 (2009). — p.28.

[61] P. W. Anderson, "Absence of diffusion in certain random lattices", *Phys. Rev.* **109**, 1492 (1958). — p.28 and 49.

[62] E. Abrahams, P. W. Anderson, D. C. Licciardello, and T. V. Ramakrishnan, "Scaling theory of localization: Absence of quantum diffusion in two dimensions", *Phys. Rev. Lett.* **42**, 673 (1979). — p.28 and 49.

[63] A. F. Ioffe and A. R. Regel, "Non-crystalline, amorphous and liquid electronic semiconductors", *Prog. Semicond.* **4**, 237 (1960). — p.28.

[64] A. Lagendijk, B. A. van Tiggelen, and D. S. Wiersma, "Fifty years of Anderson localization", *Physics Today* **62**, 24 (2009). — p.28 and 59.

[65] S. John, "Localization of light", *Physics Today* **44**, 32 (1991). — p.28.

[66] D. S. Wiersma, P. Bartolini, A. Lagendijk, and R. Righini, "Localization of light in a disordered medium", *Nature* **390**, 671 (1997). — p.28, 50, and 70.

[67] F. Scheffold, R. Lenke, R. Tweer, and G. Maret, "Localization or classical diffusion of light?", *Nature* **398**, 206 (1999). — p.28, 50, and 70.

[68] C. M. Aegerter, M. Störzer, S. Fiebig, W. Bührer, and G. Maret, "Observation of Anderson localization of light in three dimensions", *J. Opt. Soc. Am. A* **24**, 23 (2007). — p.28.

[69] H. Hu, A. Strybulevych, J. H. Page, S. E. Skipetrov, and B. A. van Tiggelen, "Localization of ultrasound in a three-dimensional elastic network", *Nat. Phys.* **4**, 945 (2008). — p.28 and 49.

[70] S. Faez, A. Strybulevych, J. H. Page, A. Lagendijk, and B. A. van Tiggelen, "Observation of multifractality at the Anderson localization transition of ultrasound in open three-dimensional media", *Phys. Rev. Lett.* **103**, 155703 (2009). — p.28.

[71] A. Richardella, P. Roushan, S. Mack, B. Zhou, D. A. Huse, D. D. Awschalom, and A. Yazdani, "Visualizing critical correlations near the metal-insulator transition in $Ga_{1-x}Mn_xAs$", *Science* **327**, 665 (2010). — p.28.

[72] R. Friedel and P. Israel, *Edison's electric light: biography of an invention*, Rutgers University Press, New Brunswick (NJ) (1987). — p.29.

[73] D. Lindley, "Focus: Invention of the maser and laser", *Phys. Rev. Focus* **15**, 4 (2005). — p.29.

[74] V. S. Letokhov, "Generation of light by a scattering medium with negative resonance absorption", *Sov. Phys. JETP* **26**, 835 (1968). — p.29, 77, and 87.

[75] V. M. Markushev, V. F. Zolin, and C. M. Briskina, "Powder laser", *Zh. Prikl. Spektrosk.* **45**, 847 (1986). — p.29.

[76] C. Gouedard, D. Husson, C. Sauteret, F. Auzel, and A. Migus, "Generation of spatially incoherent short pulses in laser-pumped neodymiun stoichiometric crystals and powders", *J. Opt. Soc. Am. B* **10**, 2358 2362 (1993). — p.29.

[77] N. M. Lawandy, R. M. Balachandran, A. S. L. Gomes, and E. Sauvain, "Laser action in strongly scattering media", *Nature* **368**, 436 (1994). — p.29, 70, 77, and 78.

[78] D. S. Wiersma, M. P. van Albeda, and A. Lagendijk, "Random laser?", *Nature* **373**, 203 (1995). — p.29.

[79] C. M. Soukoulis, X. Jiang, J. Y. Xu, and H. Cao, "Dynamic response and relaxation oscillations in random lasers", *Phys. Rev. B* **65**, 041103 (2002). — p.29.

[80] K. L. van der Molen, A. P. Mosk, and A. Lagendijk, "Intrinsic intensity fluctuations in random lasers", *Phys. Rev. A* **74**, 053808 (2006). — p.29 and 73.

[81] H. Cao, X. Jiang, Y. Ling, J. Y. Xu, and C. M. Soukoulis, "Mode repulsion and mode coupling in random lasers", *Phys. Rev. B* **67**, 161101 (2003). — p.29 and 92.

[82] D. S. Wiersma, M. P. van Albada, and A. Lagendijk, "Coherent backscattering of light from amplifying random media", *Phys. Rev. Lett.* **75**, 1739 (1995). — p.29.

[83] G. van Soest, F. J. Poelwijk, and A. Lagendijk, "Speckle experiments in random lasers", *Phys. Rev. E* **65**, 046603 (2002). — p.29.

[84] H. Cao, Y. G. Zhao, H. C. Ong, S. T. Ho, J. Y. Dai, J. Y. Wu, and R. P. H. Chang, "Ultraviolet lasing in resonators formed by scattering in semiconductor polycrystalline films", *Appl. Phys. Lett.* **73**, 3656 (1998). — p.29, 77, and 78.

[85] H. Cao, Y. G. Zhao, S. T. Ho, E. W. Seelig, Q. H. Wang, and R. P. H. Chang, "Random laser action in semiconductor powder", *Phys. Rev. Lett.* **82**, 2278 (1999). — p.29, 30, 39, 68, 77, 78, and 88.

[86] H. E. Türeci, L. Ge, S. Rotter, and A. D. Stone, "Strong interactions in multimode random lasers", *Science* **320**, 643 (2008). — p.30, 33, 39, 78, and 88.

[87] J. Andreasen, A. A. Asatryan, L. C. Botten, M. A. Byrne, H. Cao, L. Ge, L. Labont, P. Sebbah, A. D. Stone, H. E. Treci, and C. Vanneste, "Modes of random lasers", *Adv. Opt. Photon.* **3**, 88 (2011). — p.30 and 78.

[88] X. Wu, W. Fang, A. Yamilov, A. A. Chabanov, A. A. Asatryan, L. C. Botten, and H. Cao, "Random lasing in weakly scattering systems", *Phys. Rev. A* **74**, 053812 (2006). — p.30 and 59.

[89] G. van Soest, *Experiments on random lasers*, Ph.D. thesis, University of Amsterdam (2001). — p.30, 62, 64, 65, 78, and 114.

[90] A. Yamilov, X. Wu, H. Cao, and A. L. Burin, "Absorption-induced confinement of lasing modes in diffusive random media", *Opt. Lett.* **30**, 2430 (2005). — p.30 and 87.

[91] S. Mujumdar, M. Ricci, R. Torre, and D. S. Wiersma, "Amplified extended modes in random lasers", *Phys. Rev. Lett.* **93**, 053903 (2004). — p.30, 77, 78, and 88.

[92] H. Cao, "Review on latest developments in random lasers with coherent feedback", *J. Phys. A* **38**, 10497 (2005). — p.30, 59, and 70.

[93] D. S. Wiersma, "The physics and applications of random lasers", *Nat. Phys.* **4**, 359 (2008). — p.30, 36, 59, 70, 77, and 78.

[94] P. A. Lee and A. D. Stone, "Universal conductance fluctuations in metals", *Phys. Rev. Lett.* **55**, 1622 (1985). — p.30.

[95] S. Feng, C. Kane, P. A. Lee, and A. D. Stone, "Correlations and fluctuations of coherent wave transmission through disordered media", *Phys. Rev. Lett.* **61**, 834

(1988). — p.30.

[96] T. Wilk, S. C. Webster, A. Kuhn, and G. Rempe, "Single-atom single-photon quantum interface", *Science* **317**, 488 (2007). — p.33.

[97] A. F. Koenderink, L. Bechger, H. P. Schriemer, A. Lagendijk, and W. L. Vos, "Broadband fivefold reduction of vacuum fluctuations probed by dyes in photonic crystals", *Phys. Rev. Lett.* **88**, 143903 (2002). — p.33.

[98] J. N. Farahani, D. W. Pohl, H. J. Eisler, and B. Hecht, "Single quantum dot coupled to a scanning optical antenna: A tunable superemitter", *Phys. Rev. Lett.* **95**, 017402 (2005). — p.33.

[99] R. Y. Tsien, "The green fluorescent protein", *Annu. Rev. Biochem.* **67**, 509 (1998). — p.33.

[100] V. Westphal and S. W. Hell, "Nanoscale resolution in the focal plane of an optical microscope", *Phys. Rev. Lett.* **94**, 143903 (2005). — p.33.

[101] W. Min, S. Lu, S. Chong, R. Roy, G. Holtom, and X. S. Xie, "Imaging chromophores with undetectable fluorescence by stimulated emission microscopy", *Nature* **461**, 1105 (2009). — p.33.

[102] P. Horowitz and W. Hill, *The Art of Electronics*, Cambridge University Press (1989). — p.33.

[103] R. Sens and K. H. Drexhage, "Fluorescence quantum yield of oxazine and carbazine laser dyes", *J. Lumin.* **24**, 709 (1981). — p.36.

[104] D. Magde, J. H. Brannon, T. L. Cremers, and J. Olmsted, "Absolute luminescence yield of Cresyl Violet. A standard for the red", *J. Phys. Chem.* **83**, 696 (1979). — p.36.

[105] S. J. Isak and E. M. Eyring, "Fluorescence quantum yield of Cresyl Violet in methanol and water as a function of concentration", *J. Phys. Chem.* **96**, 1738 (1992). — p.36.

[106] P. G. Seybold, M. Gouterman, and J. Callis, "Calorimetric, photometric and lifetime determinations of fluorescence yields of fluorescein dyes", *Photochem. Photobiol.* **9**, 229 (1969). — p.37.

[107] G. van Soest and A. Lagendijk, "Beta factor in a random laser", *Phys. Rev. E* **65**, 047601 (2001). — p.39, 40, 70, and 93.

[108] F. De Martini and G. R. Jacobovitz, "Anomalous spontaneous-stimulated-decay phase transition and zero-threshold laser action in a microscopic cavity", *Phys. Rev. Lett.* **60**, 1711 (1988). — p.40.

[109] S. Noda, "Seeking the ultimate nanolaser", *Science* **314**, 260 (2006). — p.40.

[110] B. A. van Tiggelen and S. E. Skipetrov, "Fluctuations of local density of states and C_0 speckle correlations are equal", *Phys. Rev. E* **73**, 045601 (2006). — p.43 and 47.

[111] F. Abeles, "Investigations on the propagation of sinusoidal electromagnetic waves in stratified media. Application to thin films.", *Ann. Phys. (Paris)* **5**, 596 (1950). — p.44.

[112] L. A. A. Pettersson, L. S. Roman, and O. Inganas, "Modeling photocurrent action spectra of photovoltaic devices based on organic thin films", *J. Appl. Phys.* **86**, 487 (1999). — p.44.

[113] S. Smolka, *Quantum correlations and light localization in disordered nanophotonic structures.*, Ph.D. thesis, Technical University of Denmark (2010). — p.45.

[114] A. Cazé, R. Pierrat, and R. Carminati, "Near-field interactions and non-

universality in speckle patterns produced by a point source in a disordered medium", *Phys. Rev. A* **82**, 043823 (2010). — p.47.

[115] S.-A. BIEHS and J.-J. GREFFET, "Statistical properties of spontaneous emission from atoms near a rough surface", *Phys. Rev. A* **84**, 052902 (2011). — p.47.

[116] M. D. BIROWOSUTO, S. E. SKIPETROV, W. L. VOS, and A. P. MOSK, "Observation of spatial fluctuations of the local density of states in random photonic media", *Phys. Rev. Lett.* **105**, 013904 (2010). — p.47 and 103.

[117] P. W. ANDERSON, "The question of classical localization: A theory of white paint?", *Philos. Mag. B* **52**, 505 (1985). — p.49 and 50.

[118] S. JOHN, "Strong localization of photons in certain disordered dielectric superlattices", *Phys. Rev. Lett.* **58**, 2486 (1987). — p.49.

[119] A. A. CHABANOV, M. STOYTCHEV, and A. Z. GENACK, "Statistical signatures of photon localization", *Nature* **404**, 850 (2000). — p.49.

[120] J. WANG and A. Z. GENACK, "Transport through modes in random media", *Nature* **471**, 345 (2011). — p.49.

[121] J. BILLY, V. JOSSE, Z. ZUO, A. BERNARD, B. HAMBRECHT, P. LUGAN, D. CLÉMENT, L. SANCHEZ-PALENCIA, P. BOUYER, and A. ASPECT, "Direct observation of Anderson localization of matter waves in a controlled disorder", *Nature* **453**, 891 (2009). — p.49.

[122] G. ROATI, C. D'ERRICO, L. FALLANI, M. FATTORI, C. FORT, M. Z. G. MODUGNO, M. MODUGNO, and M. INGUSCIO, "Anderson localization of a non-interacting BoseEinstein condensate", *Nature* **453**, 895 (2009). — p.49.

[123] S. S. KONDOV, W. R. MCGEHEE, J. J. ZIRBEL, and B. DEMARCO, "Three-dimensional Anderson localization of ultracold matter", *Science* **334**, 66 (2011). — p.49.

[124] H. DE RAEDT, A. LAGENDIJK, and P. DE VRIES, "Transverse localization of light", *Phys. Rev. Lett.* **62**, 47 (1989). — p.49 and 50.

[125] Y. LAHINI, A. AVIDAN, F. POZZI, M. SOREL, R. MORANDOTTI, D. N. CHRISTODOULIDES, and Y. SILBERBERG, "Anderson localization and nonlinearity in one-dimensional disordered photonic lattices", *Phys. Rev. Lett.* **100**, 013906 (2008). — p.50.

[126] L. LEVI, M. RECHTSMAN, B. FREEDMAN, T. SCHWARTZ, O. MANELA, and M. SEGEV, "Disorder-enhanced transport in photonic quasicrystals", *Science* **332**, 1541 (2011). — p.50 and 58.

[127] S. FISHMAN, D. R. GREMPEL, and R. E. PRANGE, "Chaos, quantum recurrences, and Anderson localization", *Phys. Rev. Lett.* **49**, 509 (1982). — p.50.

[128] F. L. MOORE, J. C. ROBINSON, C. F. BHARUCHA, B. SUNDARAM, and M. G. RAIZEN, "Atom optics realization of the quantum δ-kicked rotor", *Phys. Rev. Lett.* **75**, 4598 (1995). — p.50.

[129] S. JOHN, "Localization and absorption of waves in a weakly dissipative disordered medium", *Phys. Rev. B* **31**, 304 (1985). — p.50.

[130] R. L. WEAVER, "Anomalous diffusivity and localization of classical waves in disordered media: The effect of dissipation", *Phys. Rev. B* **47**, 1077 (1993). — p.50 and 53.

[131] J. C. J. PAASSCHENS, T. S. MISIRPASHAEV, and C. W. J. BEENAKKER, "Localization of light: Dual symmetry between absorption and amplification", *Phys. Rev. B* **54**, 11887 (1996). — p.50.

[132] Z. Q. Zhang, A. A. Chabanov, S. K. Cheung, C. H. Wong, and A. Z. Genack, "Dynamics of localized waves: Pulsed microwave transmissions in quasi-one-dimensional media", *Phys. Rev. B* **79**, 144203 (2009). — p.50.

[133] Hewlett-Packard, *Measuring Dielectric Constant with the HP 8510 Network Analyzer*, Hewlett-Packard, Pablo Alto, CA (1985). — p.50.

[134] M. Rechtsman, A. Szameit, F. Dreisow, M. Heinrich, R. Keil, S. Nolte, and M. Segev, "Amorphous photonic lattices: Band gaps, effective mass, and suppressed transport", *Phys. Rev. Lett.* **106**, 193904 (2011). — p.51.

[135] E. Hecht, *Optics*, Addison Wesley (2002). — p.51 and 82.

[136] L. Novotny and B. Hecht, *Principles of Nano-Optics*, Cambridge University Press, Cambridge (2006). — p.51.

[137] W. E. Schiesser and G. W. Griffiths, *A Compendium of Partial Differential Equation Models. Method of Lines Analysis with MatLab.*, Cambridge University Press (2009). — p.53 and 65.

[138] Y. V. Fyodorov and A. D. Mirlin, "Level-to-level fluctuations of the inverse participation ratio in finite quasi 1d disordered systems", *Phys. Rev. Lett.* **71**, 412 (1993). — p.54.

[139] Y. Lahini, R. Pugatch, F. Pozzi, M. Sorel, R. Morandotti, N. Davidson, and Y. Silberberg, "Observation of a localization transition in quasiperiodic photonic lattices", *Phys. Rev. Lett.* **103**, 013901 (2009). — p.58.

[140] D. Capeta, J. Radić, A. Szameit, M. Segev, and H. Buljan, "Anderson localization of partially incoherent light", *Phys. Rev. A* **84**, 011801 (2011). — p.58.

[141] A. Yodh and B. Chance, "Spectroscopy and imaging with diffusing light", *Physics Today* **48**, 34 (1995). — p.59.

[142] M. A. Noginov, *Solid-State Random Lasers*, Springer, New York (2005). — p.59, 69, and 70.

[143] P. M. Johnson, S. Faez, and A. Lagendijk, "Full characterization of anisotropic diffuse light", *Opt. Express* **16**, 7435 (2008). — p.59.

[144] R. G. S. El-Dardiry, A. P. Mosk, and A. Lagendijk, "Spatial threshold in amplifying random media", *Opt. Lett.* **35**, 3063 (2010). — p.60, 75, and 78.

[145] M. U. Vera and D. J. Durian, "Angular distribution of diffusely transmitted light", *Phys. Rev. E* **53**, 3215 (1996). — p.61.

[146] D. S. Wiersma, *Light in strongly scattering and amplifying random media*, Ph.D. thesis, University of Amsterdam (1995). — p.61.

[147] G. Beckering, S. J. Zilker, and D.Haarer, "Spectral measurements of the emission from highly scattering gain media", *Opt. Lett.* **22**, 1427 (1997). — p.61 and 89.

[148] P. S. Whitfield and L. D. Mitchell, "Quantitative rietveld analysis of the amorphous content in cements and clinkers", *J. Mater. Sci.* **38**, 4415 (2003). — p.61.

[149] G. van Soest, F. P. Poelwijk, R. Sprik, and A. Lagendijk, "Dynamics of a random laser above threshold", *Phys. Rev. Lett.* **86**, 1522 (2001). — p.64.

[150] R. C. Hilborn, "Einstein coefficients, cross sections, f values, dipole moments, and all that", *Am. J. Phys.* **50**, 982 (1982). — p.64.

[151] A. E. P. Veldman and K. Rinzema, "Playing with nonuniform grids", *J. Eng. Math.* **26**, 119 (1992). — p.65.

[152] G. A. Berger, M. Kempe, and A. Z. Genack, "Dynamics of stimulated emission from random media", *Phys. Rev. E* **56**, 6118 (1997). — p.68.

[153] D. S. Wiersma and S. Cavalieri, "A temperature-tunable random laser", *Nature*

414, 708 (2001). — p.69 and 70.

[154] E. Tikhonov, V. P. Yashchuk, O. Prygodjuk, and V. Bezrodny, "Wavelength tunable random laser", *Solid State Phenom.* **106**, 87 (2005). — p.69.

[155] Y. Tian, X. Ma, P. Chen, Y. Zhang, and D. Yang, "Electrically pumped wavelength-tunable ultraviolet random lasing from mgxzn1-xo films on si", *Opt. Express* **18**, 10668 (2010). — p.69.

[156] S. Gottardo, R. Sapienza, P. D. García, A. Blanco, D. S. Wiersma, and C. López, "Resonance-driven random lasing", *Nat. Photon.* **2**, 429 (2008). — p.70, 75, 78, and 114.

[157] W. L. Barnes, A. Dereux, and T. W. Ebbesen, "Surface plasmon subwavelength optics", *Nature* **424**, 824 (2003). — p.70.

[158] A. Polman, "Plasmonics applied", *Science* **322**, 868 (2008). — p.70.

[159] T. van der Beek, P. Barthelemy, P. M. Johnson, D. S. Wiersma, and A. Lagendijk, "Light transport through disordered layers of dense gallium arsenide submicron particles", *Phys. Rev. B* **85**, 115401 (2012). — p.70.

[160] H. A. Atwater, , and A. Polman, "Plasmonics for improved photovoltaic devices", *Nat. Mater.* **9**, 205 (2010). — p.70.

[161] D. Lim, K. K. Chu, and J. Mertz, "Wide-field fuorescence sectioning with hybrid speckle and uniform illumination microscopy", *Opt. Lett.* **33**, 1819 (2008). — p.70.

[162] A. Gaiduk, M. Yorulmaz, P. V. Ruijgrok, and M. Orrit, "Room-temperature detection of a single molecules absorption by photothermal contrast", *Science* **330**, 353 (2010). — p.70.

[163] P. Kukura, M. Celebrano, A. Renn, and V. Sandoghdar, "Single-molecule sensitivity in optical absorption at room temperature", *J. Phys. Chem. Lett.* **1**, 3323 (2010). — p.70.

[164] S. Chong, W. Min, and X. S. Xie, "Ground-state depletion microscopy: Detection sensitivity of single-molecule optical absorption at room temperature", *J. Phys. Chem. Lett.* **1**, 3316 (2010). — p.70.

[165] M. Celebrano, P. Kukura, A. Renn, and V. Sandoghdar, "Single molecule imaging by optical absorption", *Nat. Photon.* **5**, 95 (2011). — p.70.

[166] Y. D. Chong, L. Ge, H. Cao, and A. D. Stone, "Coherent perfect absorbers: Time-reversed lasers", *Phys. Rev. Lett.* **105**, 053901 (2010). — p.70 and 103.

[167] W. Wan, Y. Chong, L. Ge, H. Noh, A. D. Stone, and H. Cao, "Time-reversed lasing and interferometric control of absorption", *Science* **331**, 889 (2011). — p.70 and 103.

[168] M. Leonetti and C. Conti, "Haus/GrossPitaevskii equation for random lasers", *J. Opt. Soc. Am. B* **27**, 1446 (2010). — p.70 and 78.

[169] R. G. S. El-Dardiry, S. Faez, and A. Lagendijk, "Classification of light sources and their interaction with active and passive environments", *Phys. Rev. A* **83**, 031801(R) (2011). — p.70, 71, 89, and 93.

[170] S. Rentsch, R. Danielius, and R. Gadonas, "Bestimmung von lebensdauern und transientenabsorptionsspektren von polymethinfarbstoffen aus pikosekunden-spektroskopischen messungen", *J. Signalaufz.-Mater.* **12**, 319 (1984). — p.70.

[171] N. Cherroret and A. Buchleitner, "Entanglement and thouless times from coincidence measurements across disordered media", *Phys. Rev. A* **83**, 033827 (2011). — p.74.

[172] K. L. van der Molen, *Experiments on Scattering Lasers. From Mie to random.*,

Ph.D. thesis, University of Twente (2007). — p.74 and 87.

[173] G. D. Dice, S. Mujumdar, and A. Y. Elezzabi, "Plasmonically enhanced diffusive and sub-diffusive metal nanoparticle-dye random laser", *Appl. Phys. Lett.* **86**, 131105 (2005). — p.75.

[174] X. Meng, K. Fujita, Y. Zong, S. Murai, and K. Tanaka, "Random lasers with coherent feedback from highly transparent polymer films embedded with silver nanoparticles", *Appl. Phys. Lett.* **92**, 201112 (2008). — p.75.

[175] F. A. Pinheiro and L. C. Sampaio, "Lasing threshold of diffusive random lasers in three dimensions", *Phys. Rev. A* **73**, 013826 (2006). — p.78.

[176] K. L. van der Molen, R. W. Tjerkstra, A. P. Mosk, and A. Lagendijk, "Spatial extent of random laser modes", *Phys. Rev. Lett.* **98**, 143901 (2007). — p.78, 79, 80, 88, 92, and 94.

[177] H. Cao, Y. Ling, J. Y. Xu, and A. L. Burin, "Probing localized states with spectrally resolved speckle techniques", *Phys. Rev. E* **66**, 025601 (2002). — p.78.

[178] J. Fallert, R. J. B. Dietz, J. Sartor, D. Schneider, C. Klingshirn, and H. Kalt, "Co-existence of strongly and weakly localized random laser modes", *Nat. Photon.* **3**, 279 (2009). — p.78, 88, 94, and 102.

[179] R. C. Polson and Z. V. Vardeny, "Spatially mapping random lasing cavities", *Opt. Lett.* **35**, 2801 (2010). — p.78.

[180] A. Tulek, R. C. Polson, and Z. V. Vardeny, "Naturally occurring resonators in random lasing of pi-conjugated polymer films", *Nat. Phys.* **6**, 303 (2010). — p.78, 79, and 94.

[181] M. Leonetti, C. Conti, and C. Lopez, "The mode-locking transition of random lasers", *Nat. Photon.* **5**, 615 (2011). — p.78, 88, 95, and 102.

[182] C. Vanneste, P. Sebbah, and H. Cao, "Lasing with resonant feedback in weakly scattering random systems", *Phys. Rev. Lett.* **98**, 143902 (2007). — p.78.

[183] H. E. Türeci, A. D. Stone, and B. Collier, "Self-consistent multimode lasing theory for complex or random lasing media", *Phys. Rev. A* **74**, 043822 (2006). — p.78 and 88.

[184] W. L. Sha, C.-H. Liu, and R. R. Alfano, "Spectral and temporal measurements of laser action of Rhodamine 640 dye in strongly scattering media", *Opt. Lett.* **19**, 1922 (1994). — p.78.

[185] S. Mujumdar, V. Türck, R. Torre, and D. S. Wiersma, "Chaotic behavior of a random laser with static disorder", *Phys. Rev. A* **76**, 033807 (2007). — p.78, 85, and 86.

[186] R. Uppu and S. Mujumdar, "Statistical fluctuations of coherent and incoherent intensity in random lasers with nonresonant feedback", *Opt. Lett.* **35**, 2831 (2010). — p.78 and 79.

[187] H. Cao, J. Y. Xu, D. Z. Zhang, S.-H. Chang, S. T. Ho, E. W. Seelig, X. Liu, and R. P. H. Chang, "Spatial confinement of laser light in active random media", *Phys. Rev. Lett.* **84**, 5584 (2000). — p.78.

[188] X. Wu, W. Fang, A. Yamilov, A. A. Chabanov, A. A. Asatryan, L. C. Botten, and H. Cao, "Random lasing in weakly scattering systems", *Phys. Rev. A* **74**, 053812 (2006). — p.78 and 94.

[189] X. Wu and H. Cao, "Statistics of random lasing modes in weakly scattering systems", *Opt. Lett.* **32**, 3089 (2007). — p.78 and 79.

[190] B. Redding, M. A. Choma, and H. Cao, "Spatial coherence of random laser

emission", *Opt. Lett.* **36**, 3404 (2011). — p.78.

[191] K. L. VAN DER MOLEN, A. P. MOSK, and A. LAGENDIJK, "Relaxation oscillations in long-pulsed random lasers", *Phys. Rev. A* **80**, 055803 (2009). — p.78.

[192] K. L. VAN DER MOLEN, A. P. MOSK, and A. LAGENDIJK, "Quantitative analysis of several random lasers", *Opt. Commun.* **278**, 110 (2007). — p.79.

[193] R. G. S. EL-DARDIRY, A. P. MOSK, O. L. MUSKENS, and A. LAGENDIJK, "Experimental studies on the mode structure of random lasers", *Phys. Rev. A* **81**, 043830 (2010). — p.79, 88, 94, and 102.

[194] R. UPPU and S. MUJUMDAR, "On the coherent modes of ultranarrowband random lasers with nonresonant feedback", *Appl. Opt.* **50**, E13 (2011). — p.79.

[195] R. UPPU, A. K. TIWARI, and S. MUJUMDAR, "Identification of statistical regimes and crossovers in coherent random laser emission", *Opt. Lett.* **37**, 662 (2012). — p.79.

[196] R. W. TJERKSTRA, J. G. RIVAS, D. VANMAEKELBERGH, and J. J. KELLY, "Porous GaP multilayers formed by electrochemical etching", *Electrochemical and Solid-State Letters* **5**, 32 (2002). — p.80.

[197] F. J. P. SCHUURMANS, *Light in complex dielectrics*, Ph.D. thesis, University of Amsterdam (1999). — p.80.

[198] W. H. PRESS, S. A. TEUKOLSKY, W. T. VETTERING, and B. P. FLANNERY, *Numerical Recipes. The Art of Scientific Computing.*, Cambridge University Press (2007). — p.84.

[199] B. SHAPIRO, "Large intensity fluctuations for waves in random media", *Phys. Rev. Lett.* **57**, 2168 (1986). — p.84.

[200] I. FREUND and D. ELIYAHU, "Surface correlations in multiple scattering media", *Phys. Rev. A* **45**, 6133 (1992). — p.85.

[201] X. WU and H. CAO, "Statistics of random lasing modes in weakly scattering systems", *Opt. Lett.* **32**, 3089 (2007). — p.86.

[202] A. PENZKOFER and W. LEUPACHER, "Fluorescence behaviour of highly concentrated rhodamine 6G solutions", *J. Lumin.* **37**, 61 (1987). — p.87.

[203] M. LEONETTI, C. CONTI, and C. LOPEZ, "A random laser tailored by directional stimulated emission", *arXiv:1112.3533v1* (2011). — p.88.

[204] T. NAKAMURA, T. HOSAKA, and S. ADACHI, "Gold-nanoparticle-assisted random lasing from powdered gan", *Opt. Express* **19**, 467 (2011). — p.89.

[205] O. ZAITSEV, "Spacing statistics in two-mode random lasing", *Phys. Rev. A* **76**, 043842 (2007). — p.92.

[206] M. P. VAN EXTER, G. NIENHUIS, and J. P. WOERDMAN, "Two simple expressions for the spontaneous emission factor β", *Phys. Rev. A* **54**, 3553 (1996). — p.93.

[207] R. G. S. EL-DARDIRY and A. LAGENDIJK, "Tuning random lasers by engineered absorption", *Appl. Phys. Lett.* **98**, 161106 (2011). — p.94.

[208] H. G. VÖLZ, *Industrial color testing: fundamentals and techniques*, Wiley-VCH (2001). — p.97.

[209] A. P. GIBSON, J. C. HEBDEN, and S. R. ARRIDGE, "Recent advances in diffuse optical imaging", *Phys. Med. Biol.* **50**, R1 (2005). — p.98.

[210] O. L. MUSKENS and A. LAGENDIJK, "Method for broadband spectroscopy of light transport through opaque scattering media", *Opt. Lett.* **34**, 395 (2009). — p.98.

[211] UNITED STATES ENVIRONMENTAL PROTECTION AGENCY, *Guidance Manual for Compliance with the Interim Enhanced Surface Water Treatment Rule: Turbidity Provisions*, EPA-815-R-99-010 (1999). — p.100.

[212] M. J. SADAR, *Understanding Turbidity Science*, Technical Information Series Booklet No. 11., Hach Company (1996). — p.100.

[213] T. NAKAMURA, B. P. TIWARI, and S. ADACHI, "Control of random lasing in ZnO/Al$_2$O$_3$ nanopowders", *Appl. Phys. Lett.* **99**, 231105 (2011). — p.101.

[214] B. GJONAJ, J. AULBACH, P. M. JOHNSON, A. P. MOSK, L. KUIPERS, and A. LAGENDIJK, "Active spatial control of plasmonic fields", *Nat. Photon.* **5**, 360 (2011). — p.101.

[215] A. LAGENDIJK, "Fundamental optical physics: Uncovering superabsorption", *Nat. Photon.* **5**, 252 (2011). — p.102.

[216] P. SPINELLI, M. A. VERSCHUUREN, and A. POLMAN, "Broadband omnidirectional antireflection coating based on subwavelength surface Mie resonators", *Nat. Comm.* **3**, 692 (2012). — p.103.

[217] Y. D. CHONG and A. D. STONE, "Hidden black: Coherent enhancement of absorption in strongly-scattering media", *Phys. Rev. Lett.* **107**, 163901 (2011). — p.103.

[218] F. H. CORNELISSE, *Inleiding tot de wetenschapsfilosofie*, Van Loghum Slaterus (1985). — p.111 and 112.

[219] M. MATHIJSEN, "Hoe ver kun je gaan?", *NRC Handelsblad* (September 18, 2009). — p.111.

[220] A. LAGENDIJK, "Hoe literair mag wetenschap zijn?", *NRC Handelsblad* (October 17, 2009). — p.112.

[221] T. S. KUHN, *The structure of scientific revolutions*, University of Chicago Press (1962). — p.112.